

Distributed Vibration Sensing using Rayleigh Backscatter in Optical Fibers

Alexander Kipkosgei Sang

Dissertation submitted to the faculty of the Virginia Polytechnic Institute and State University in
partial fulfillment of the requirements for the degree of

Doctor of Philosophy
In
Aerospace Engineering

Joseph A. Schetz
Mark Froggatt
Rakesh Kapania
William Devenport
Robert Walters

December 5th 2011
Blacksburg, Virginia

Keywords: distributed sensing, vibration, Rayleigh scatter, dynamic strain, optical fiber

Copyright 2011, Alexander K Sang

Distributed Vibration Sensing using Rayleigh Backscatter in Optical Fiber

Alexander Kipkosgei Sang

ABSTRACT

Sensing has been essential for the investigation, understanding, exploitation, and utilization of physical phenomena. Traditional single-point sensing methods are being challenged by the multi-point or distributed sensing capabilities afforded by optical fiber sensors. A powerful technique available for distributed sensing involves the use of the Optical Frequency Domain Reflectometry (OFDR).

This work focuses on using OFDR as a means of obtaining distributed vibration measurements using the Rayleigh scatter along a single-mode optical fiber. The effort begins by discussing various distributed measurement techniques currently in use before discussing the OFDR technique. Next, a thorough discussion on how high spatially resolved Rayleigh measurements are acquired and how such measurements can be used to make static strain measurements is presented. A new algorithm to resolve strain at regions of high spatial gradient is developed. This results in enhanced measurement performance of systems using the Rayleigh scatter to determine static strain or temperature measurements by improving measurement fidelity at the high gradient locations.

Next, discussions on how dynamic strain (vibration) couples to optical fiber in a single point and in a distributed setting are presented. Lessons learned are then used to develop a new and unique distributed vibration measurement algorithm. Various consequential benefits are then reviewed before concluding remarks are stated.

A simulation model was developed and used to supplement this investigation in every step of the discussion. The model was used to gain insight on how various physical phenomena interact with the optical fiber. The simulation was also used to develop and optimize the high gradient and vibration algorithms developed herein. Simple experiments were then used to validate the theory and the simulation models.

ACKNOWLEDGEMENTS

I would like to thank God for giving me the opportunity for pursuing this degree. I extend my gratitude to Dr. J. Schetz and Dr. M. Froggatt for believing in me and providing the necessary support to accomplish this work. I also recognize members of my committee, Dr. R. Kapania, Dr. W. Devenport and Dr. R. Walters for helping me in numerous ways. Thank you.

I would like to also extend my sincere gratitude to Ms. Debbie Nester, Secretary to Dr. Walters and Ms. Rachel M. Hall Smith, the Aerospace Department Graduate Coordinator for helping me process paper work and guiding me through the administrative requirements and deadlines, without which, I would not have been able to graduate in the fall of 2011.

Next, I would like to thank members of the Luna Technologies Research and Development team and Engineering team, led by Dawn Gifford and Eric Sanborn for giving me unconditional support during this effort. Members of the OSG are also recognized for their contribution through equipment loans for some of the experiments performed in support of this dissertation. I thank Stephen Kreger and Aida Rahim for reviewing this document before submission to the committee. Special thanks is extended to Sandra Klute for keeping me motivated for the past several years to get the task of writing the dissertation completed. I would also like to thank Roger Duncan and Larry Vacari, individuals that helped me in one way or another in completing the early phases of this effort.

I would like to recognize the Jennings and Mahaffey clans for familial support. I would like to thank Dr. Nelly Yatich and Ezra Mereng for keeping me motivated in accomplishing this task. Yes Nelly, better late than never.

I thank my American family; the late Dr. J. Schultz, Patricia K. Schultz, Christopher, Francie and Joanna. Thank you for hosting me through the first few years of my stay in the United States. I extend my gratitude to my African family, Prof. Sang, Mrs. Mary Sang, Rispah, Monica, Kigen, my nephews and nieces for providing me with emotional support and staying in continuous prayer for me.

I finally recognize my wife and best friend, Sheri Renee Jennings Kosgei for enduring through the times where I stayed isolated from our family in an effort to complete this work. I thank you for your continual love.

God bless you all!

DEDICATION

This is dedicated to my wife and children. Alexandra Jepyator and Jennings Kiptunen, Daddy loves you.

Alexander K Sang

TABLE OF CONTENTS

ABSTRACT.....	ii
ACKNOWLEDGEMENTS.....	iii
DEDICATION.....	iv
TABLE OF CONTENTS.....	v
NOMENCLATURE.....	vii
LIST OF FIGURES.....	ix
1 Introduction.....	1
1.1 Advent of Sensing.....	1
1.2 Electricity based sensing.....	1
1.3 Optical Sensors.....	3
1.3.1 Single Point Optical Sensors.....	4
1.3.2 Distributed Sensing.....	5
1.4 Motivation for the Research.....	7
1.4.1 General Motivation.....	7
1.4.2 Potential Applications.....	7
1.4.3 Layout of Investigation.....	9
2 Distributed Measurement Techniques in Optical Fibers.....	10
2.1 Optical fiber.....	10
2.2 Time Domain Measurement.....	11
2.2.1 Optical Time Domain Reflectometry.....	11
2.2.2 The Polarization Optical Time Domain Reflectometry.....	13
2.2.3 Raman Scattering.....	13
2.2.4 Brillouin Scattering.....	16
2.3 Frequency Domain Measurement.....	18
2.3.1 Low Coherence Frequency Domain reflectometry.....	18
2.3.2 Optical Frequency Domain Reflectometry.....	19
3 An Analysis of Rayleigh Scattering.....	30
3.1 Single point reflection Analysis.....	30
3.1.1 Introductory analysis.....	30
3.1.2 Single point Simulation Derivation.....	31
3.2 Distributed reflection Analysis.....	36
3.2.1 Coupled-Mode Theory derivation.....	36
3.2.2 Multi-point Simulation Derivation.....	39
3.3 Summary.....	44
4 Static Strain Theory.....	45
4.1 Rayleigh Scatter Acquisition.....	45
4.2 The strain function.....	48
4.3 Resolving strain in Rayleigh scatter temporal domain.....	49
4.4 Resolving strain in Rayleigh scatter spectrum.....	51
4.4.1 Constant strain approximation.....	51
4.5 Summary.....	52
5 Static Strain Simulations and Experiments.....	54

5.1	Phase Derivative Computer Simulation.....	54
5.2	Phase Derivative of Acquired Data.....	56
5.3	Constant Strain Computer Simulation.....	57
5.4	Constant Strain Experimental Data.....	58
5.5	Linear Strain Approximation.....	60
5.6	Summary.....	63
6	Dynamic Strain Theory.....	64
6.1	Understanding the basics of Vibration coupling into OFDR measurement.....	64
6.1.1	Frequency variation effects.....	66
6.1.2	Amplitude variation effects.....	66
6.1.3	Baseband shift of amplitude signal.....	67
6.1.4	Vibration extraction from single point measurement.....	68
6.2	Vibration coupling into a distributed measurement.....	71
6.2.1	Dynamic strain only.....	71
6.2.2	Vibration and Strain.....	72
6.3	Summary.....	73
7	Dynamic Strain Simulations and Experiments.....	74
7.1	Computer Simulation: Vibration Only.....	74
7.2	Computer Simulation: Strain and Vibration.....	82
7.3	Experimental implementation of strain and vibration algorithm.....	87
7.4	Summary.....	90
8	Summary and conclusions.....	91
8.1	Summary.....	91
8.2	Conclusions.....	92
8.3	Future work.....	92
9	Appendix A: Optical Path Length relationship Development.....	93
10	Appendix B: Frequency related to Instrument Parameters.....	95
11	Appendix C: Supporting Works by the Author.....	97
	REFERENCES.....	109

NOMENCLATURE

Below is a list of symbols in order of appearance

R_1	Resistor 1
R_2	Resistor 2
R_3	Resistor 3
R_4	Resistor 4
V_G	Sensor voltage
V_{IN}	Excitation voltage
θ_c	Critical angle
$R(T)$	Absolute temperature via Raman thermometry
λ_a	Anti-stokes wavelength
λ_s	Stokes wavelength
$\tilde{\nu}$	Wave number separation from the pump wavelength
h	Planck's constant
c	Speed of light
k	Boltzmann's constant
T	Absolute temperature
V_a	Speed of sound in glass
n	Index of refraction
λ_p	Free space pumping wavelength
$\Delta\tau$	Time delay
ω_x	Angular frequency at location x
α	Rate of change of angular frequency
λ_B	Bragg wavelength
$\delta\lambda_B$	Change in Bragg wavelength
Λ	Grating period
ε_1	Principle strain component
ε_t	Principle strain component
p_{ij}	Pockel's coefficients
μ	The Poison ratio
dn/dT	Rate of change of the refractive index with respect to temperature
G_n	Bragg grating n
L_n	Length to Bragg grating n
k	Propagation number
ω	Angular frequency
λ	Wavelength of energy source
k_0	Propagation number
n_{eff}	Effective group index of refraction of the fiber
t	Time

ω_0	Starting angular frequency
Δs	Fiber segment
E_0	Field intensity of optical energy source
E_n	Field intensity of region n
$\phi_n(t)$	Phase as a function of time of region n
L_1	Path length from the source to end reflector of the measurement arm and back to the optical detector
L_2	Path length from the source to the reference arm reflection and back to the detector
d_n	Length of segment n in interferometer
I	Irradiance
ε	Permittivity
v	Electromagnetic wave speed
I_{INT}	Time varying interference component
θ	Phase difference term
τ_n	Delay of point n
E^+	Forward propagating field intensity
E^-	Backward propagating field intensity
$\kappa(x)$	Rayleigh backscatter of the fiber
E_1^n	Reflectivity along the core of the fiber at position x^n
x^n	Fiber location at n
$\widehat{\kappa}(x)$	Rayleigh scatter function
$\varepsilon(x)$	Strain field
Δx	Sampling resolution
$\frac{d\phi}{dx}$	Phase derivative
C	Strain constant
\mathfrak{F}	Fourier transform
A_{vib}	Amplitude of vibration
ω_{vib}	Frequency of vibration
V_s	Start of vibration region
V_e	End of vibration region

LIST OF FIGURES

Figure 1-1 A Wheatstone bridge circuit.....	2
Figure 1-2. A Piezoresistive accelerometer sensor using a Wheatstone bridge to make measurements.....	3
Figure 1-3. Single-point fiber optic vibration sensor.....	4
Figure 1-4. Distributed (a) and quasi-distributed sensing of optical fiber capable using various techniques	5
Figure 1-5. An unbalanced (a), and a balanced (b) Michelson interferometer used by the OFDR and OLCR techniques respectfully	6
Figure 1-6 A vibration simulation of an aircraft structure to extract vibration modes (a) and acquisition modules used for accelerometer during experimentation (b).....	8
Figure 1-7 A vibration simulation of an aircraft structure to extract vibration modes (a) and acquisition modules used for accelerometer during experimentation (b).....	8
Figure 2-1. Optical fiber cross-section.....	10
Figure 2-2 Optical fiber classifications.....	11
Figure 2-3. OTDR schematic diagram.....	11
Figure 2-4. A typical OTDR trace	12
Figure 2-5. P-OTDR network diagram	13
Figure 2-6. An Energy Level diagram of Rayleigh and Stokes and Anti-Stokes Raman Scattering	14
Figure 2-7. The variation in the Stokes and anti-Stokes amplitude, however the signals are symmetric around the pump frequency.....	14
Figure 2-8. Distributed Raman thermometry optical network.....	15
Figure 2-9. A Raman trace from initial thermometry demonstration by Dankin <i>et al</i>	15
Figure 2-10. The Brillouin Frequency Distribution.....	16
Figure 2-11 Temperature and strain dependencies of the Brillouin frequency shift in fibers at 1.3 μm	17
Figure 2-12. B-OTDR using a pulsed and a continuous wavelength (CW) laser.....	17
Figure 2-13 Network diagram of the low coherence frequency domain reflectometry technique	18
Figure 2-14. Basic OFDR Network, represented as a Michelson Interferometer.....	19
Figure 2-15. FBG fabrication based on a) holographic and b)phase mask exposure	20
Figure 2-16 Diagram of the operation of a FBG.....	21
Figure 2-17. Bragg grating thermal sensitivity at elevated temperatures	22
Figure 2-18 Wavelength division multiplexing of Bragg gratings	23
Figure 2-19 The basics of OFDR.....	23
Figure 2-20. Data acquisition using the OFDR technique on fiber Bragg gratings.....	24
Figure 2-21. An optical fiber containing an FBG array (a.k.a. – ‘sensing fiber’).	25
Figure 2-22. Optical network used for polarization-diverse measurement of Rayleigh backscatter.	26
Figure 2-23 The reflectivity of a 25 meter spool (5 cm radius) of standard single-mode fiber....	27
Figure 2-24. Rayleigh backscatter random reflection features	27
Figure 2-25. Demonstration of a Thermal shift of an optical fiber.....	29
Figure 3-1. A basic Michelson Interferometer in optical fiber	31
Figure 3-2. Wavelength and Frequency of an unbalanced Michelson interferometer with different optical path length differences with nominally similar end reflections.....	35

Figure 3-3. Optical network depicting distributed reflection.....	36
Figure 3-4. Optical network depicting detailed back reflection of Rayleigh scatter	37
Figure 3-5. A distributed scan with two partially reflecting mirrors	39
Figure 3-6. Simulated data showing the signal at the detector and the Fourier transform of the same.	42
Figure 3-7. Detector intensity from simulation model of an optical fiber	43
Figure 3-8. Rayleigh scatter from simulation model of an optical fiber.....	43
Figure 3-9. An illustration of the mean positional variance introduced to simulate Rayleigh scatter.	44
Figure 4-1. An example of Rayleigh scatter reflections at atomic resolution	46
Figure 4-2. An example of Rayleigh scatter measurement spectrum at full atomic resolution and corresponding window representing laser angular frequency sweep range.....	46
Figure 4-3. An example of Rayleigh scatter measurement spectrum at full atomic resolution and corresponding window representing laser angular frequency sweep range.....	47
Figure 4-4. Rayleigh scatter reflection versus position for original scatter (grey and in the background) , Windowed spectra (red), and segmented array over the laser sweep region (black with points)	47
Figure 4-5. Axial strain applied to axial bar	48
Figure 5-1. The Rayleigh scatter and detector intensity of unstrained fiber generated using a computer simulation model.....	55
Figure 5-2. The Rayleigh scatter and detector intensity of strained fiber generated using a computer simulation model.....	55
Figure 5-3 The phase and phase derivative for a constant strain field over a subset of the domain of the computer simulated dataset.....	56
Figure 5-4 The phase and phase derivative for a constant strain field over a 0.31 Meter section of single mode fiber from experimental data acquired using the Optical Backscatter Reflectometer.....	57
Figure 5-5. The strain function computed from the computer simulated Rayleigh scatter spectrum.....	58
Figure 5-6. The strain function computed from the experimentally acquired Rayleigh scatter spectrum.....	59
Figure 5-7. Experimental data of Spectral shift versus position in a high temperature test	60
Figure 5-8. Experimental test setup, also showing the Rayleigh scatter trace of the fiber.....	61
Figure 5-9 Spectral shift computed using an algorithm that implemented a linear slop estimate over the high gradient region	62
Figure 6-1. A Michelson Interferometer in optical fiber with a vibrating mirror on the measurement arm.....	64
Figure 6-2. A single point on a fiber vibrating to a 20Hz signal Inset shows a close-up of the peak.....	65
Figure 6-3. Detector intensity and modeled Rayleigh Scatter of a single point	66
Figure 6-4. Effects of a 20Hz vibration signal with increasing amplitude.	67
Figure 6-5. Base band-shifted frequency signal of an optical path length =1 at various vibration signal modulation frequencies.	68
Figure 6-6. Procedural recovery of 20Hz input vibration signal.	69
Figure 6-7. Procedural recovery of 10Hz, 15Hz and 25 Hz input vibration signal.	70
Figure 6-8. Optical network depicting distributed reflection where the FUT is oscillating.....	71

Figure 7-1. Modeled Rayleigh scatter with a 20Hz vibration signal perturbing the fiber	74
Figure 7-2. Spectral shift curves at various points of the fiber.....	76
Figure 7-3. Temporal shift curves at various points of the fiber	77
Figure 7-4. Spectral shift quality as a function of position. Reference compared to 20Hz vibration	78
Figure 7-5. Temporal shift quality as a function of position. Reference compared to 20Hz vibration	78
Figure 7-6. Vibration Signal at various locations along the fiber after processing with algorithm	80
Figure 7-7. Rayleigh Scatter of fiber perturbed with 20Hz signal after vibration correction.....	81
Figure 7-8 Spectral shift quality as a function of position for the fiber at states.....	81
Figure 7-9. Temporal shift quality as a function of position for the fiber at states	82
Figure 7-10. Rayleigh Scatter of fiber perturbed with 20Hz signal and 400 $\mu\epsilon$ strain field.....	83
Figure 7-11. Rayleigh Scatter of fiber after correction of 20Hz vibration signal where a 400 $\mu\epsilon$ strain field present.....	83
Figure 7-12. The temporal shift quality of strained fiber at before, with and after vibration correction	84
Figure 7-13. The spectral shift quality of strained fiber at before, with and after vibration correction	84
Figure 7-14. Rayleigh Scatter of fiber perturbed with 20Hz signal and 400 $\mu\epsilon$ strain field.....	85
Figure 7-15. Strain as a function of position of the vibration free and vibrating segment	86
Figure 7-16. Strain as a function of position of the vibration free and vibration corrected segment	87
Figure 7-17. Experimental setup for vibration extraction modeling.....	88
Figure 7-18. End peak reflection of strained optical fiber before and after vibration correction where a 2Vpp 20Hz vibration was induced to the measurement.....	88
Figure 7-19. Spectral shift as a function of position of the vibration and vibration corrected segment	89
Figure 7-20. Spectral shift as a function of position of the vibration free and vibration corrected segment	90

Distributed Vibration Sensing using Rayleigh Backscatter in Optical Fiber

1 Introduction

In this chapter, a brief history on the evolution of sensing will be presented chronologically to the reader. Various sensing technologies will be discussed. An introduction to single point and distributed optical sensing will then be presented before remarks on the motivation behind this research.

1.1 Advent of Sensing

Sensing has been essential for the investigation, understanding, exploitation and utilization of physical phenomena and the resultant derivatives dating back to the dawn of man. Starting from the basic senses of sight, sound, touch, smell and taste, human beings were able to begin developing systems to improve quality of life. The use of common, readily available items such as sticks, were used as sensing mechanisms; the audible sound of snapping twigs would alert the hunter of approaching game.

With time, the invention of new systems and technologies resulted in the evolution of sensors. Weight sensors such as the scale balance were used to quantify all kinds of goods and commodities to facilitate and expand trade. The ancient Romans and Greeks used the device as a standard to value agricultural produce. The Arabs extended the use of the device to establish standards for minerals such as gold, silver and gems.¹

The invention of the odometer by Archimedes of Syracuse during the First Punic war in 23 BC² led to one of the first mechanical measurement sensing systems. It was a chariot with a wheel designed such that it revolved 400 times in one mile. A peg on the inside rim of the wheel tied to a 400 tooth gear, enabled the tracking of distance by dropping a pebble into a container at every mile^{3,4}. The device enabled the growth and expansion of the Roman Empire by facilitating rapid movement of troops, communication and commerce. Overall, sensors to this point had indicating mechanisms that could be directly interpreted by one of, or a combination of our five common senses.

1.2 Electricity based sensing

The 18th-20th century so the dawn of the industrial age; a period when science and technology led to inventions, such as the steam engine, the internal combustion engine and electric power

generation, that were to change the human socio-economic structure⁵. Sensing technologies aided the scientific advancement by facilitating parameter measurement leading to an understanding of the underlying principles of the object or system under investigation. A classic example is the galvanometer, an instrument that enabled the measurement of voltage and current, contributing to the formulation of Ohm's Law⁶ and the development of the science of electromagnetism⁷. The understanding of electrical phenomenon led to the development of a new class of sensors that exploited circuit theory and electromagnetism. The Wheatstone bridge, invented by Samuel Hunter Christie⁸, was one such measuring instrument that has been used in its current or derivative form in various electrical sensor platforms such as temperature, pressure and strain sensors. The basic Wheatstone bridge circuit contains four resistors, a voltage input and a voltage sensor in a configuration illustrated in Figure 1-1 below. At the point of bridge balance, the ratio R_1/R_2 is equal to R_3/R_4 , resulting in no current flowing through the voltage sensor V_G . However, a change in resistance in R_4 or any other resistor member of the circuit would lead to a proportional change in voltage measured.

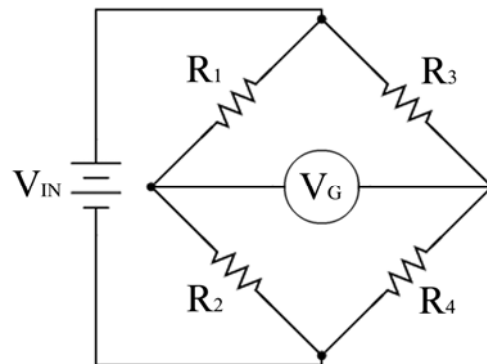
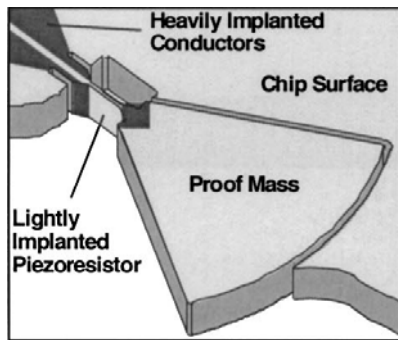
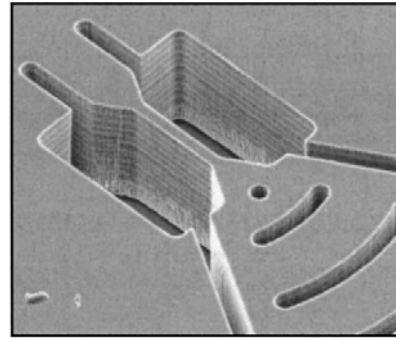


Figure 1-1 A Wheatstone bridge circuit

An illustration of the use of the above principle is seen in accelerometers. Such sensors are commonly used for vibration monitoring⁹. Here, a pie shaped proof mass shown in Figure 1-2a is attached to the sensor housing through a slender cantilever. A lightly implanted piezoresistor is fused to the sides of the flexure. These elements are used to complete the bridge circuit. Flexure deflection due to vibration results in change in the bridge resistors causing a proportional change in the voltage output. Figure 1-2b shows a SEM image of the planer piezoresistive accelerometer.



a) Design illustration



b) SEM image of planar piezoresistive accelerometer

Figure 1-2. A Piezoresistive accelerometer sensor using a Wheatstone bridge to make measurements⁹

While meeting the goal of vibration measurement, such sensors only make point measurements hence, the aggregation of several sensors is required to acquire a pseudo-distributed measurement. Such grouping is accomplished through wired¹⁰ or wireless¹¹ means, however, due to sensor and installation cost, the spatial density leaves much to be desired¹⁰.

1.3 Optical Sensors

With the invention of the laser in 1960¹², coupled with the development of photon detectors¹³, the field of opto-electronics emerged leading to a new class of sensors that exploited optical radiation as a measurement mechanism.

The laser is a source of quasi-monochromatic, collimated, coherent light that could be used as a means of information transfer through data encoding and decoding at optical frequencies ($\cong 10^{14} \text{ Hz}$) leading to high bandwidth and ultra-fast transfer rates. However, in order to exploit the identified attributes, a means of propagation between the source and the destination needed to be identified. The parallel development of optical fibers as waveguides, with significant breakthroughs in reducing the optical attenuation per unit length¹⁴, led to its adoption as the primary mode for optical transmission. The low attenuation levels achieved made optical fiber a viable alternative to coaxial cabling in the telecommunications industry. This resulted in an explosion of optical fiber use leading to the availability of large quantities of moderately priced, low-loss fibers, spurring research into alternative uses of the readily available optical resource. This included the possible use as a transducing mechanism for parameter measurement. It was evident that the optical signal propagating in the fiber was modulated by external environmental stimuli such as temperature pressure and strain. Thus, with the appropriate physics, one could potentially make measurements using optical fiber.

1.3.1 Single Point Optical Sensors

Fiber optic sensors began with simple, single-point transducers such as the vibration sensor shown in Figure 1-3, where the vibration measurement is correlated to the amount of light that couples across an optical gap. The amplitude of the light is modulated by the vibration of the housing perpendicular to the neutral axis of the fiber¹⁵. Other single point optical vibration sensors with varying degrees of complexity have been developed^{16 17 18} however, no one has ventured to use optical sensing for distributed vibration detection.

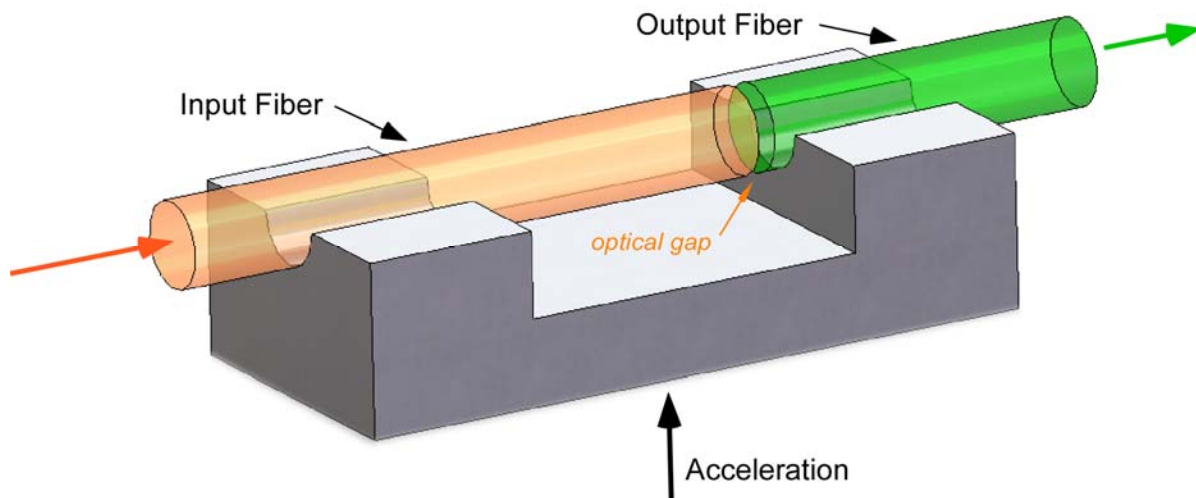


Figure 1-3. Single-point fiber optic vibration sensor

With time, single-point sensors with increasing sophistication became available, utilizing a variety of optical effects resulting from interaction of the light source with optical fiber. The effects include, but are not limited to, variation in optical intensity, phase, frequency, polarization, spectral content, evanescent field or a combination thereof. Examples of such transducers include optical current sensors which utilized polarization characteristics of light¹⁹, or fiber optic gyroscopes (FOG), which exploit optical interference as its working principle²⁰, or chemical sensors which have a spectral response to fluctuations in the evanescent field of specialty fiber²¹. Fiber optic sensors may be designed to operate similarly. Besides electromagnetic immunity and environmental stability (glass relative to copper), optical fiber offers sensing options not generally duplicated with conventional measurement techniques; the fiber length in part or in its entirety may be used as a transducer. This may be done to enhance sensitivity or provide spatial averaging by dense wrapping of the fiber to form a singular sensing surface whereupon the measurement is acquired.

1.3.2 Distributed Sensing

The parameter of interest discussed thus far is measured at a specific location. This point measurement capability has been the conventional measurement mode used widely in multiple sensing applications such as thermocouples, accelerometers, strain gages, pressure sensors etc. Fiber may also be used to facilitate distributed sensing by spatial discrimination of the measurand along the length of the fiber as illustrated in Figure 1-4.

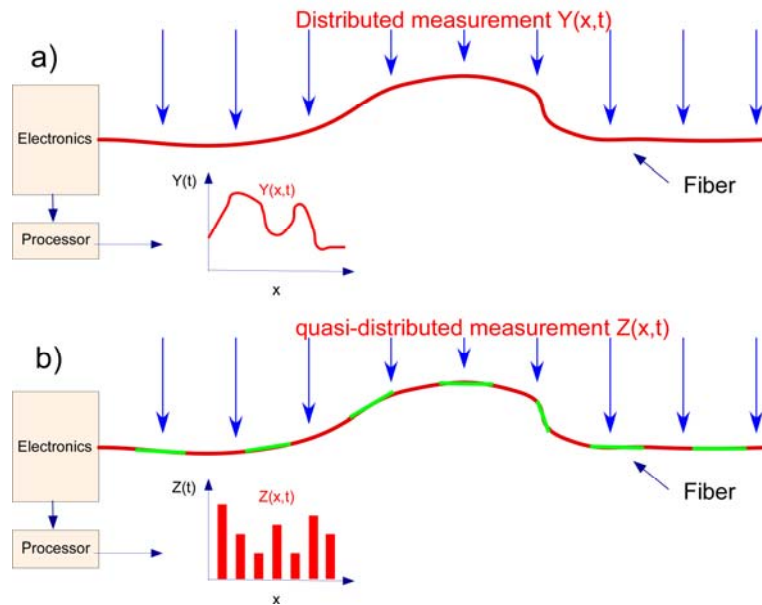


Figure 1-4. Distributed (a) and quasi-distributed sensing of optical fiber capable using various techniques

The genesis of distributed sensing in part was due to the explosion of the use of optical fiber by the telecommunications industry resulting in the need for the development of infrastructure to support the new protocol. It was necessary for diagnostics equipment to facilitate maintenance of the optical networks to locate anomalous features such as fiber breaks, regions of large loss or bad optical joints. This resulted in the invention of the Optical Time Domain Reflectometer (OTDR)²². The technology makes a measurement by sending a short series of optical pulses that propagate through the fiber, and, upon hitting a reflective event, sending a reflection back to the instrument that is proportional to the event encountered. The location of the reflection is determined by the time-of-flight taken for the pulse to return to the instrument. Interrogation techniques leveraged from this technology can make measurements from 1 to > 50 kilometers at a spatial resolution of several meters. This technology has been heavily utilized in the oil and gas industry for the thermal characterization of sub-sea wells which may be several kilometers from the platform and in the ocean floor.

OTDR technology provided the necessary platform to enable distributed sensing by exploiting various optical attributes such as polarization and phase. The introduction of Bragg gratings into optical fiber led to further gains in distributed sensing by functioning as a quasi-distributed transducer capable of interrogation via multiple demodulation platforms. The use of gratings for structural health monitoring in civil structures has steadily increased with time. The systems generally exploited the spectral shift exhibited by the gratings when subjected to a thermal or mechanical load. Various demodulation techniques enable the interrogation of 10's to 1000's of gratings on a single optical path over distances from 10's to 100's of meters. A further discussion on gratings will be presented in section 2.3.2.1.1.

With time, various interferometric techniques evolved to further enhance the spatial resolution of the measurand. The techniques were either based on a balanced (Low Coherence Frequency Domain Reflectometry [OLCR]) or an unbalanced (Optical Frequency Domain Reflectometry [OFDR]) interferometer as illustrated in Figure 1-5.

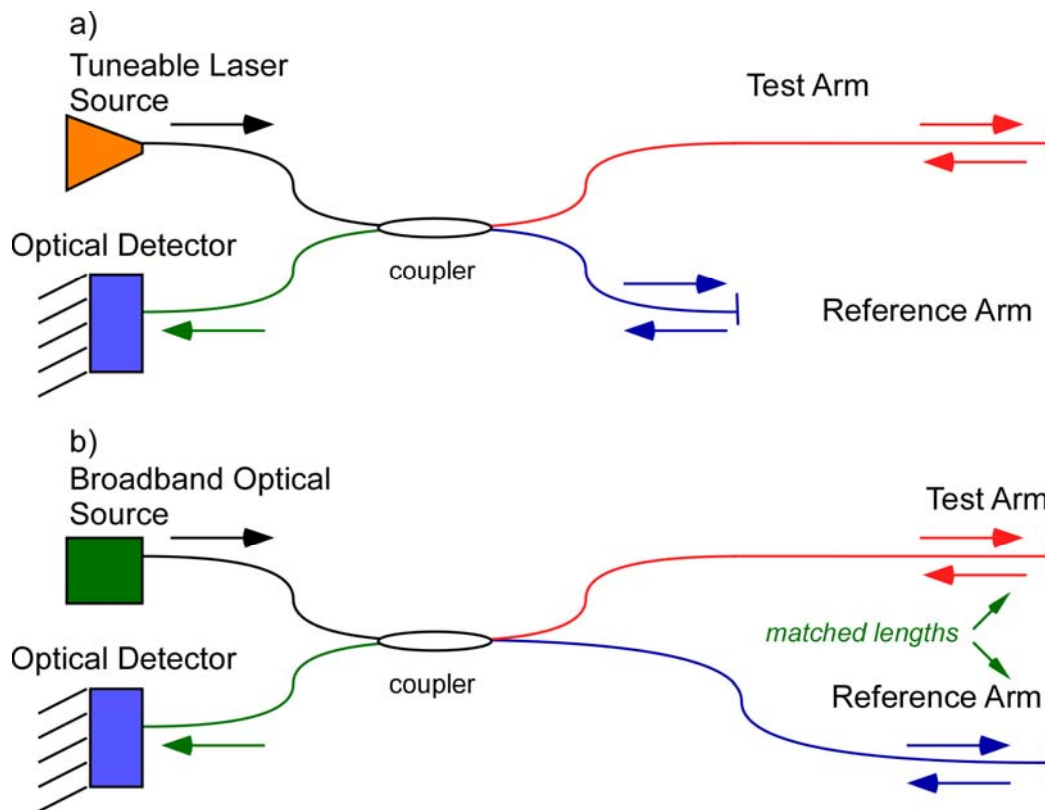


Figure 1-5. An unbalanced (a), and a balanced (b) Michelson interferometer used by the OFDR and OLCR techniques respectively

The interferometric demodulation techniques traded spatial resolution for range. The Optical Backscatter Reflectometer, the platform behind this investigation, has a reconfigurable test range, with a maximum of 2 kilometers at a 1mm, two-point spatial resolution. At shorter interrogation configurations (e.g. 30 meters) the 2 point resolution reduces to $10\mu\text{m}$. A thorough discussion of the aforementioned demodulation techniques will be discussed in chapter 2.

1.4 Motivation for the Research

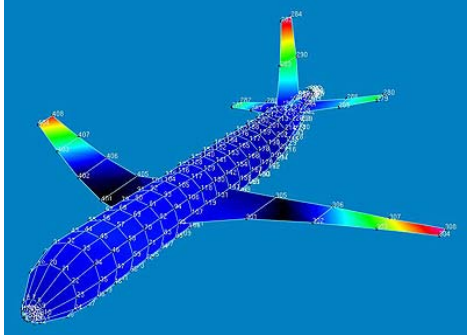
1.4.1 General Motivation

The primary motivation behind this study was to supply engineers and scientists a new tool to measure vibration in a simple yet effective layout as a continuum over the device under test. Vibration may be described as an oscillatory motion of a device from its mean position²³. The number of times a device translates over a full cycle is considered the vibration frequency. Vibration is integral to a large subset of mechanical devices, components and structures. These include, but are not limited to, cars, planes, ships, motors, generators etc. If these systems are poorly designed, oscillatory loading of structures may lead to reduced fatigue life and eventual failure. By measuring the vibration time response signal, one may be able to perform frequency and modal analysis from the time signature to reveal key performance attributes that may be exploited or rectified to maximize device performance.

The ability to determine the position-correlated, vibration evolution of a structure will provide engineers the capability to improve structural design for future components and structures, while implementing robust structural health monitoring, with the capability to detect failure locations, for existing civil structures.

1.4.2 Potential Applications

There are multiple advantages to using a distributed optical fiber sensing technique for vibration monitoring. First, optical fiber is light, hence it will not unduly influence the mass of the measurand which would result in a biased frequency response. Second, a single energy source supplied over a sole optical path is required to get a fully-distributed measurement, unlike accelerometers which require separate wiring harnesses for each assembly as illustrated in Figure 1-6.



a) Modal analysis simulation of aircraft



b) data acquisition modules for accelerometers

Figure 1-6²⁴ A vibration simulation of an aircraft structure to extract vibration modes (a) and acquisition modules used for accelerometer during experimentation (b)

In this example, the light weight, singular acquisition path of the optical fiber allows for an accurate characterizing the vibration modes and mode shapes of the structure under test by not unduly influencing the mass of the structure.

Further versatility may be achieved with optical fiber by embedding its embedment into the laminate of the composite fabrics that are growing in use in aircraft structures as illustrated in . The optical fiber will be an integrated non-intrusive component of the aircraft structure that will enable online health monitoring of static parameters such as temperature and strain.

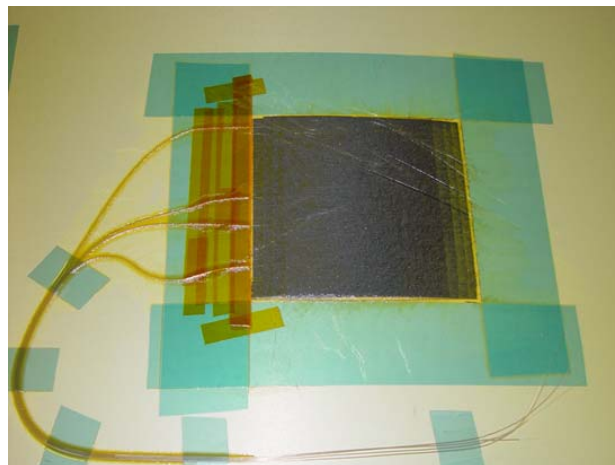


Figure 1-7 A vibration simulation of an aircraft structure to extract vibration modes (a) and acquisition modules used for accelerometer during experimentation (b)

This study extends health monitoring to dynamic parameters such as mode shape evolution, frequency shifting, crack onset and growth etc. This will allow for condition based maintenance of the vehicle and accurate prediction of the remaining useful life of the vehicle based on actual events experienced by the flight vehicle.

Optical fiber is non-conductive and immune to electromagnetic interference, hence it may be used in high voltage or high current facilities and in devices such as motors and generators. Fourth, the measurement technique is passive, so it may be used in highly volatile environments such as gasoline plants or natural gas pipelines without danger of fuel ignition.

Vibration sensing may be further leveraged for use for perimeter security by monitoring the motion of the fence. And, with further work, the sensing platform may be used as a distributed microphone for covert audio detection in various security applications.

1.4.3 Layout of Investigation

This work focuses on developing a means of measuring distributed vibration measurements based on Rayleigh scatter measurements using optical frequency domain reflectometry (OFDR) on single mode optical fiber. The effort begins by discussing various distributed measurement techniques currently in use before discussing the OFDR technique. Next a thorough discussion on how high spatially resolved Rayleigh measurements is acquired and how such measurements can be used to make static strain measurements. An algorithm to resolve strain at regions of high spatial gradient is developed by the author to further improve the robustness of Rayleigh static strain sensing. Next, discussions on how dynamic strain (vibration) couples to optical fiber in a single point and in a distributed setting are presented. Lessons learned from the vibration coupling analysis is then used to develop a distributed vibration measurement algorithm, a feat that, to this author's knowledge, has never been demonstrated in optical fiber. Various consequential benefits are then reviewed before concluding remarks are stated.

A simulation model was developed by the author to supplement this investigation in every step of the discussion and to give further insight on how various physical phenomena interacted with the optical fiber. The simulation was also used to develop and optimize the algorithm to resolve measurements at regions of high spatial parameter variation. The simulation was also used to develop the vibration algorithm. Simple experiments were then used to validate the theory and the simulation models.

2 Distributed Measurement Techniques in Optical Fibers

In this chapter, various distributed measurement techniques will be discussed in sufficient detail to give the reader an overall understanding of current, commonly used distributed parameter measurement techniques used in various industries. The chapter will address techniques with increasing similarity before finally discussing the method implemented in this investigation.

2.1 Optical fiber

Prior to delving into a discussion on the various methodologies for distributed measurement acquisition, it is best to briefly discuss the fundamentals of optical fibers to give the reader a basic understanding of the medium, and its form, function, optical propagation and transmission attributes.

Optical fibers are hair-thin, plastic or silica structures that are designed in such a manner as to act as waveguides to light along its length by total internal reflection²⁵. The light propagation mechanism is achieved by design, where a central core is surrounded by a cladding of like material that has a slightly lower index of refraction²⁷. The refractive index mismatch consequently results in a critical angle θ_c , within the core whereby any light beam striking the core-cladding interface at or greater than θ_c will result in total internal reflection as illustrated in Figure 2-1.

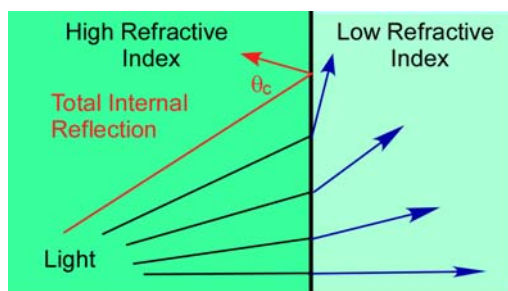


Figure 2-1. Optical fiber cross-section

The propagation properties of optical fibers are generally determined by the variation in the core diameter and core/cladding refractive index. Multimode fibers (MMF) generally have a large core and support the propagation of light in multiple paths or propagation modes²⁹. A stepped index MMF has a constant refractive index throughout the core, in contrast to a graded index MMF, which has a gradient variation of the refractive index from the core center where it is greatest, to the outer core/cladding boundary³⁰. Due to the multi-path propagation, MMF results

in optical dispersion, where the light broadens as a function of distance as illustrated in Figure 2-2b and Figure 2-2c. MMF's are usually used for short communication links or high power transmission. Single mode fiber (SMF) is designed to support one optical propagation mode hence has reduced dispersion characteristics as seen in Figure 2-2a. SMF is usually used for communication links longer than 200 meters. Sensing in optical fiber is primarily done using SMF, and that is the fiber type used in this study.

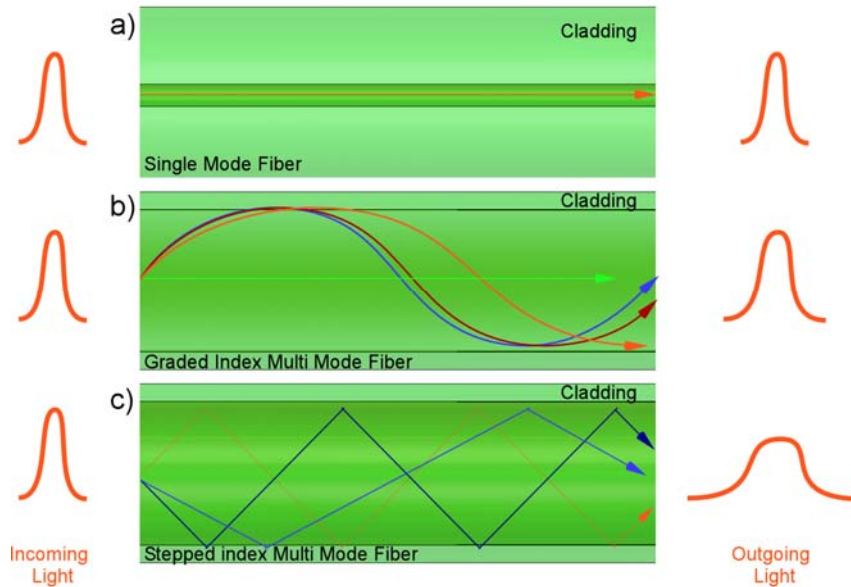


Figure 2-2 Optical fiber classifications

2.2 Time Domain Measurement

2.2.1 Optical Time Domain Reflectometry

The need for prognostics/diagnostic equipment for fiber optic telecommunication links to troubleshoot bends, breaks and poor connectors resulted in the invention of the Optical Time Domain Reflectometer (OTDR)³¹. The basic layout of the device is illustrated in Figure 2-3 below.

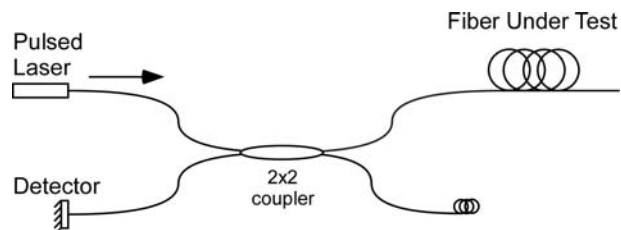


Figure 2-3. OTDR schematic diagram

The OTDR is a time-domain encoding technique that functions by injecting an optical pulse into the fiber under test (FUT). Light is backscattered as it propagates down the FUT due to small, irregular, continuously distributed features formed during the manufacturing process at the atomic level. The elastic mode of this reflective phenomenon is known as Rayleigh scattering. Here, the scattered photons have the same frequency and wavelength of the incident photons. The intensity of the optical reflection from the atomic boundaries is measured and integrated as a function of time and is then mapped as a function of position revealing the FUT overall attenuation including features such as splices, connectors, bends and breaks. The spatial resolution of the system is a function of the pulse width, whereby a narrow pulse results in fine spatial resolution but results in reduced amplitude of the return signal. Figure 2-4 is an illustration of a typical attenuation plot from an OTDR.

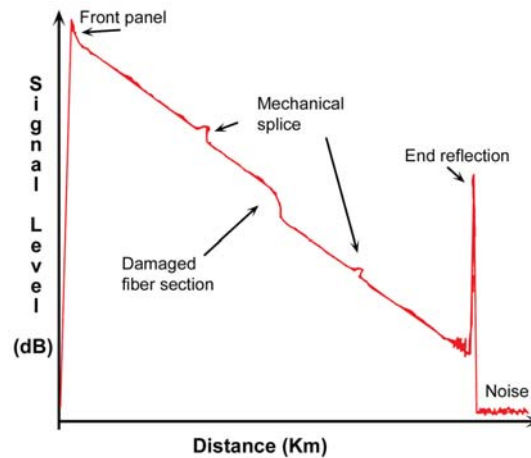


Figure 2-4. A typical OTDR trace

The OTDR was not purpose-built for spatially resolved parameter measurement; however it clearly provided a platform and a pattern of thought, to enable the evolution of distributed sensing³². It was, therefore, desirous to determine optical parameters that were sensitive to environmental variables of interest such as temperature, pressure, strain, vibration, electric field, magnetic field, gamma radiation, neutron radiation etc. The fiber attenuation, directly measured by the OTDR, was marginally (if at all) sensitive to these parameters³³; hence the need for the exploitation of optically induced effects by the interaction of the fiber and laser. Key among these was phase dependent properties such as the polarization state evolution, coherence and the optical phase itself.

2.2.2 The Polarization Optical Time Domain Reflectometry

The first implementation of optical time domain reflectometry (OTDR) technique for distributed sensing was the investigation of the use of the variance in the polarization state due to a physical disturbance on the fiber^{34,35,36}. Polarization is a property of transverse waves which describes the orientation of the oscillations in the plane perpendicular to the wave's direction of travel³⁷. The Polarization-OTDR (P-OTDR) at its simplest form, introduces a polarizer analyzer into the return path prior to the detector as illustrated in Figure 2-5.

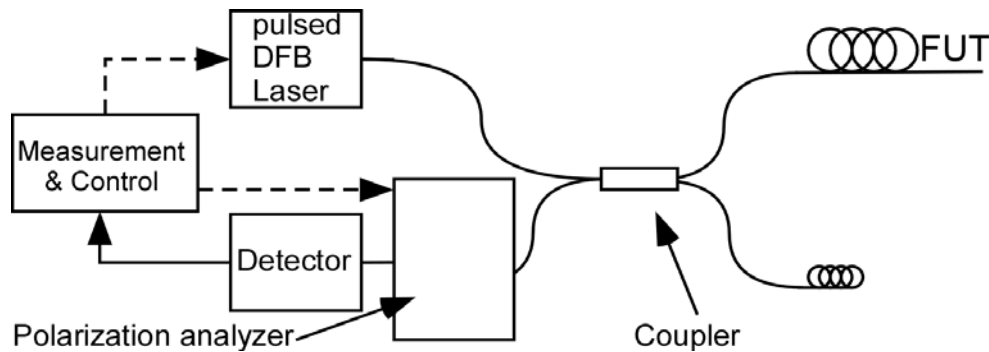


Figure 2-5. P-OTDR network diagram

2.2.3 Raman Scattering

In 1985, Dankin *et al* proposed the use of non-elastic scattering based on the Raman effect in an OTDR configuration for distributed sensing³⁸. In both Rayleigh and Raman scattering, the incident photon causes the excitation of an electron into a higher virtual energy state. With time, the electron decays back to a lower level emitting a scattered photon. In Rayleigh scattering, the electron decays back to the same level from which it started, however, in Raman scattering, the electron decays to an energy level different than the incident photon³⁹ as illustrated in Figure 2-6. Due to the Maxwell-Boltzmann energy partition, the emitted frequency (or wavelength) is equal to a discrete energy state of the molecule which is usually at a state lower than the incident photon. This emission level, known as the Stokes wavelength, is the predominant state of occurrence in Raman scattering. For an emitted photon to have a higher frequency (or lower wavelength), the molecule would have to provide the extra energy required which will only happen if the molecule is already in an excited condition due to a thermal variation from its ground state. This level is known as the anti-Stokes wavelength.

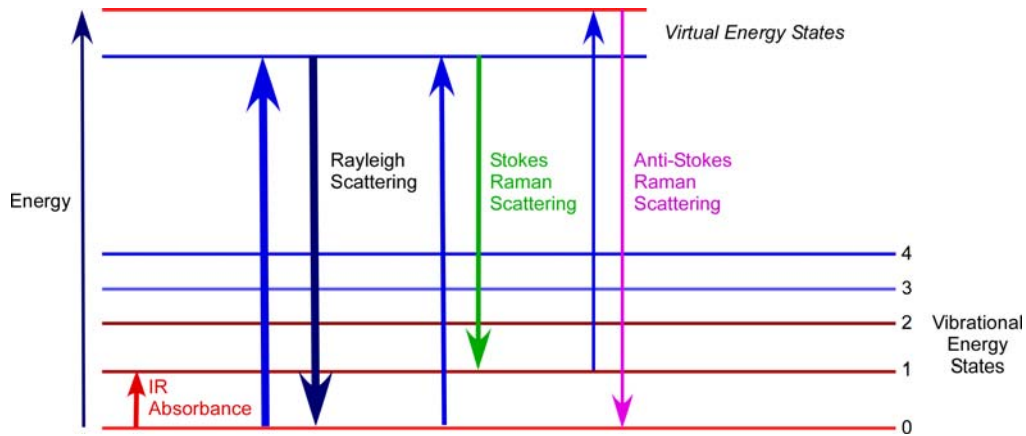


Figure 2-6. An Energy Level diagram of Rayleigh and Stokes and Anti-Stokes Raman Scattering

The number of molecules at the anti-Stokes wavelength is directly proportional to the absolute temperature of the medium, therefore, by monitoring the ratio of the amplitudes of the Stokes to the anti-Stokes wavelengths, one may determine the absolute temperature of the device under test by the relationship given by:

$$R(T) = (\lambda_s / \lambda_a)^4 \cdot e^{-h \cdot c \cdot \tilde{\nu} / kT} \quad (2-1)^{38}$$

where λ_a and λ_s are the measured anti-Stokes and Stokes wavelengths, $\tilde{\nu}$ is the wave number separation from the pump wavelength, h is Planck’s constant, c is the speed of light, k is the Boltzmann’s constant and T is the absolute temperature of the core of the section of fiber from which the scattered light was received³⁸. Figure 2-7 illustrates the symmetry of the Stokes and anti-Stokes lines about the pump frequency. Recall that frequency is inversely related to wavelength. The variation in intensity is also seen, where the Stokes lines have higher energy content than the corresponding anti-Stokes lines.

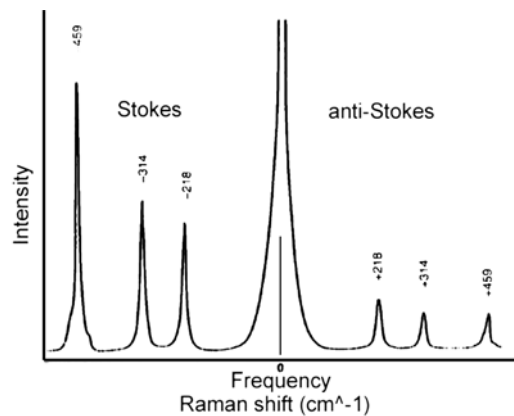


Figure 2-7. The variation in the Stokes and anti-Stokes amplitude, however the signals are symmetric around the pump frequency⁴⁰

The optical network for Raman thermometry is a modification of the OTDR layout with the addition of a spectral filter to enable separate detection of the Stokes and anti-Stokes frequencies prior to data processing as illustrated in Figure 2-8.

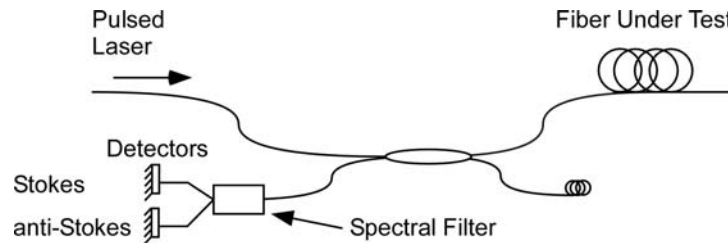


Figure 2-8. Distributed Raman thermometry optical network

Figure 2-9 shows experimental results obtained by Dakin *et al*⁴² as a demonstration of the technology. A fiber ~90 km long had regions placed in an ice bath, an oven and a water bath to induce thermal variation at different segments. Temperature variation in the optical path length is seen as detected by Raman thermometry. An argon ion pump laser producing 15 ns pulses with a center wavelength of 514 nm and 5 W peak power was used on telecommunications grade MMF with a 50 μ m/125 μ m core/cladding diameter ratio³⁸. A thermal and spatial resolution of $\pm 5^\circ$ C and 3 m, respectively was computed in this experiment. However, modern systems have improved thermal and spatial resolution to $\pm 0.5^\circ$ C and 1 m for distances up to 10 km obtained after 5 minute averaging⁴¹.

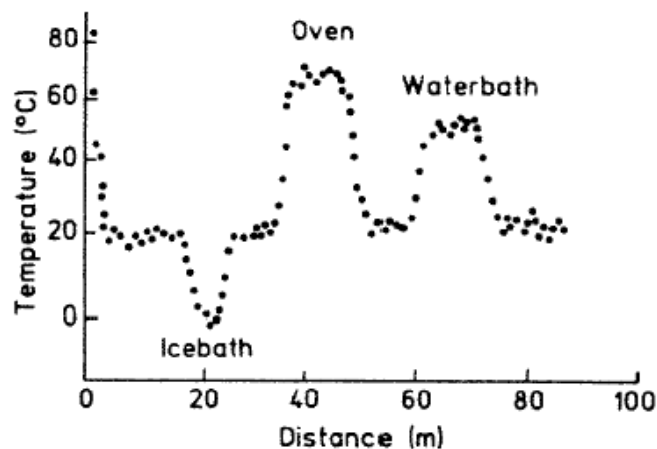


Figure 2-9. A Raman trace from initial thermometry demonstration by Dakin *et al*⁴²

2.2.4 Brillouin Scattering

In the late 1980's, Brillouin scattering was proposed as a tool for distributed sensing^{43,44}, and it was identified as Brillouin optical time-domain reflectometry (BOTDR). The sensing principle used in this technique is based on the Brillouin effect⁴⁵, which is similar to the Raman effect. As described in the previous paragraph, an optical pump laser causes molecular excitation from a ground state to an arbitrary excited state, after which decay occurs leading to the Stokes and Anti-Stokes components. However, unlike Raman scattering which depends on an intensity variation due to individual molecular rotations and vibrations, Brillouin scattering is based on the frequency shift of the Stokes and Anti-Stokes states due to overall molecular shifting, making the measurement very immune to any loss effects as illustrated in Figure 2-10.

This shifting is a result of interaction of the guided optical signal and acoustic phonons propagating in the fiber, which are produced by electrostrictive mechanisms⁴⁶ such as acoustic waves due to thermal excitation. The scattered light is frequency shifted by⁴⁷:

$$\nu_B = 2 \cdot n \cdot V_a / \lambda_p \quad (2-2)$$

where V_a is the speed of sound in glass, n is the index of refraction of the optical fiber, and λ_p is the free space pumping wavelength.

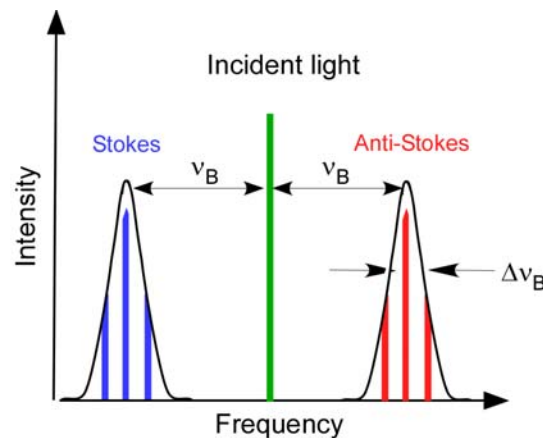


Figure 2-10. The Brillouin Frequency Distribution

For silica fiber operating at a pumping wavelength of $1.3 \mu\text{m}$ a frequency shift, $\nu_B = 13.2 \text{ GHz}$ results in the electronic, rather than the optical domain. In general, the Brillouin bandwidth (width of the Stokes and Anti-Stokes lines) in silica fiber has been reported to be in the range of 20 to $\sim 35 \text{ MHz}$, hence it can be detected with high sensitivity using coherent detection techniques.

The Brillouin shift effect and the scattered power levels are a function of both temperature and strain since the acoustic velocity and scattering cross sections are dependent on both. The measured response rate for Brillouin coefficients for strain and temperature at $1.3 \mu\text{m}$ are $4.6 \times 10^{-6} \mu\text{e}^{-1}$ and $9.4 \times 10^{-5} \text{ }^\circ\text{C}^{-1}$, respectively and they are shown in Figure 2-11⁴⁷. A typical optical layout for the BOTDR technique is shown in Figure 2-12

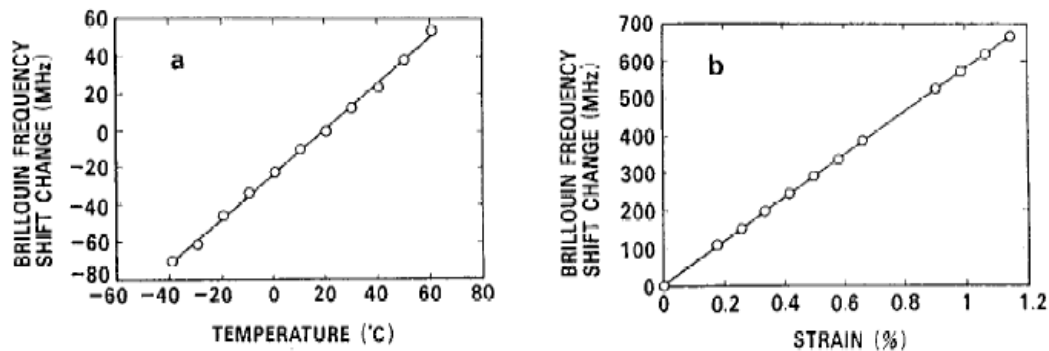


Figure 2-11 Temperature and strain dependencies of the Brillouin frequency shift in fibers at $1.3 \mu\text{m}$

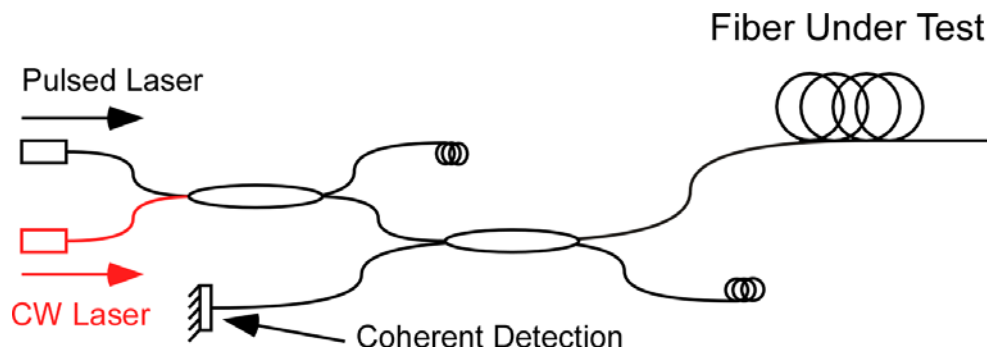


Figure 2-12. B-OTDR using a pulsed and a continuous wavelength (CW) laser

The primary advantages of thermal interrogation using BOTDR over the Raman technique is the measurement of a frequency shift rather than an intensity variation. The backscatter level of the BOTDR is larger than the Raman effect leading to less restrictive requirements on the optical detector. However, the persistence of the acoustic wave limits the spatial resolution to $\sim 1\text{m}$, and the indiscriminate response to both temperature and strain makes it difficult to distinguish temperature or strain response without modifying the transducer layout. Several authors have speculated on the use of a dual-sensing fiber in a single cable^{48,49}, one loosely ‘floating’, the other rigidly attached to the cable jacket. In this setup, the ‘floating’ fiber will respond to temperature only, whereas the other will respond to both temperature and strain, leading to a situation where one may solve the coupled equations.

2.3 Frequency Domain Measurement

2.3.1 Low Coherence Frequency Domain reflectometry

An alternative to the OTDR technique is the low coherence frequency domain reflectometry (OLCR) first proposed by Youngquist *et al*⁵⁰. The technique is based on a Michelson interferometer that utilizes a broad-band optical source. The light source is launched through a 3dB coupler into the fiber under test (FUT) and a reference arm that has a moving mirror as illustrated in Figure 2-13.

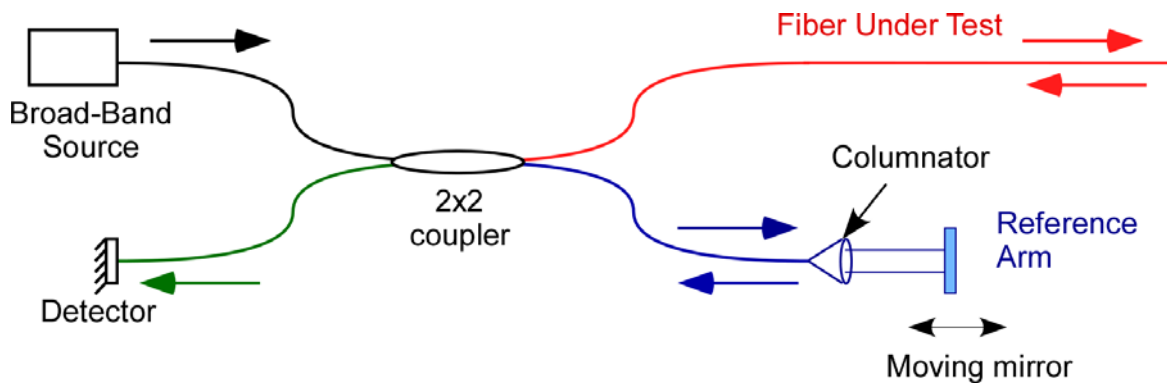


Figure 2-13 Network diagram of the low coherence frequency domain reflectometry technique

The working principle of the OCLR is to detect the resulting fringe pattern of the FUT and the local reference. This condition only occurs when the optical path lengths of the reference and the FUT are matched; other reflections that are sufficiently mismatched to be incoherent with the mirror reflection are converted to phase noise⁵¹. In general, the FUT will reflect a coherent fringe pattern to the detector at a location corresponding to the reference path which can be modulated by the motion of the mirror. Various commercial devices have been produced and have been demonstrated to produce high resolution reflective events up to a $20\mu\text{m}$, two-point spatial resolution⁵².

A key limitation to the aforementioned technology is the need to match device lengths in order to acquire a high resolution measurement. The spatial dynamic range of the instrument is further limited by the range of motion of the moving mirror which is usually no more than 0.2 m. However, variants to the above optical arrangement have demonstrated the potential of 10-100x increase in range with a modest resolution compromise⁵³.

2.3.2 Optical Frequency Domain Reflectometry

Distributed measurements may also be obtained through an interferometric technique known as optical frequency domain reflectometry (OFDR). Unlike OTDR where a pulse of laser light is transmitted, or the OCLR which utilizes a broad band source, the OFDR technique uses a continuously swept optical source. The light source is assumed to be spatially coherent, narrowband and continuously tunable over a defined frequency range⁵⁴. The basic concept of the OFDR technique is illustrated in Figure 2-14, and it is the method of choice used in this investigation. A full mathematical analysis of the technique is presented in Chapter 3.

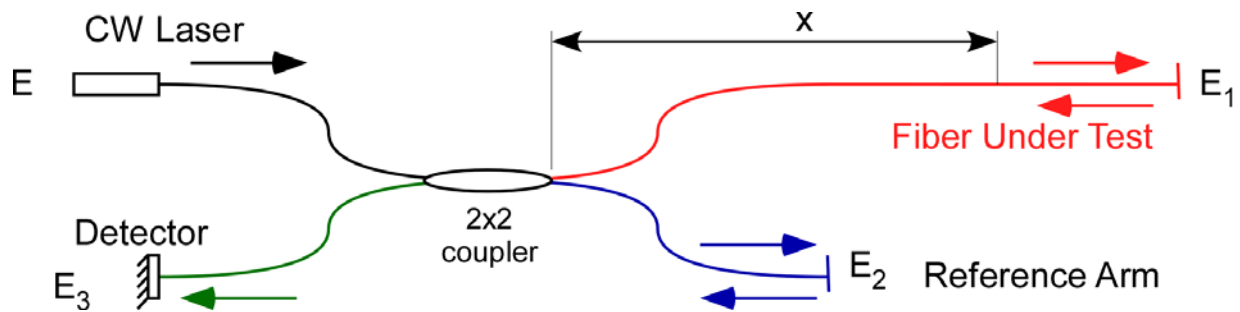


Figure 2-14. Basic OFDR Network, represented as a Michelson Interferometer

A coherent source is coupled into a 2x2 coupler and linearly tuned over a defined wavelength range. The FUT forms one arm of the Michelson interferometer, while the second arm is formed by a reference terminated by a reflective surface such as a mirror. The signal from backscattered light in the FUT at an arbitrary location x and the end reflection from the reference arm are mixed in the 2x2 coupler. The time delay at location x is:

$$\Delta\tau = \frac{2 \cdot n}{c} \cdot x \quad (2-3)$$

Where n is the index of refraction and c is the speed of light. During the time delay $\Delta\tau$, the optical frequency of the source changes by $\omega_x = \Delta\tau \cdot \overbrace{d\omega/dt}^{\alpha}$. The observed frequency ω_x is correlated to the location x , and its amplitude is proportional to the backscattered light observed at x . Performing a Fourier transform of the accumulated detector signal will result in the simultaneous display of the backscattered light from all points along the FUT.

2.3.2.1 Quasi-distributed Sensing

2.3.2.1.1 Fiber Bragg gratings

The OFDR demodulation technique has been utilized in quasi-distributed sensing methodologies where spatially distributed regions along the fiber have been sensitized to various environmental parameters of interest. The transducing mechanism of choice currently is the fiber Bragg grating (FBG). A FBG is a periodic perturbation of the refractive index over a defined length in the core of an optical fiber by exposure to an intense UV interference pattern⁵⁵. Permanent gratings in optical fiber was first demonstrated in 1978, where germanium doped fiber was exposed to an argon ion laser radiation of oppositely propagating modes^{56,57}.

Gratings may be made using a split-beam interferometer⁵⁸ or a phase mask to form the fringes⁵⁹ as illustrated in Figure 2-15. In the former, the fiber is illuminated by two beams from a UV source that intersect within the fiber. The angle between the beams, coupled with the wavelength of the UV light defines the periodicity of the interference pattern. The generated optical waveform periodically modulates the index of refraction of the fiber within the region of exposure.

In the second technique, a diffracted phase mask is placed at a predetermined distance from the fiber (typically, in contact) in the path of the UV light source such as an Excimer laser^{60,61}. The diffracted light interferes in the plane of the fiber to produce the gratings which are half the periodicity of the etched mask pattern. The phase mask technique is currently the preferred method due to the relaxed requirements of the UV laser coherence and stability, and it can be utilized in the production of gratings during fiber manufacturing in the draw-tower⁶².

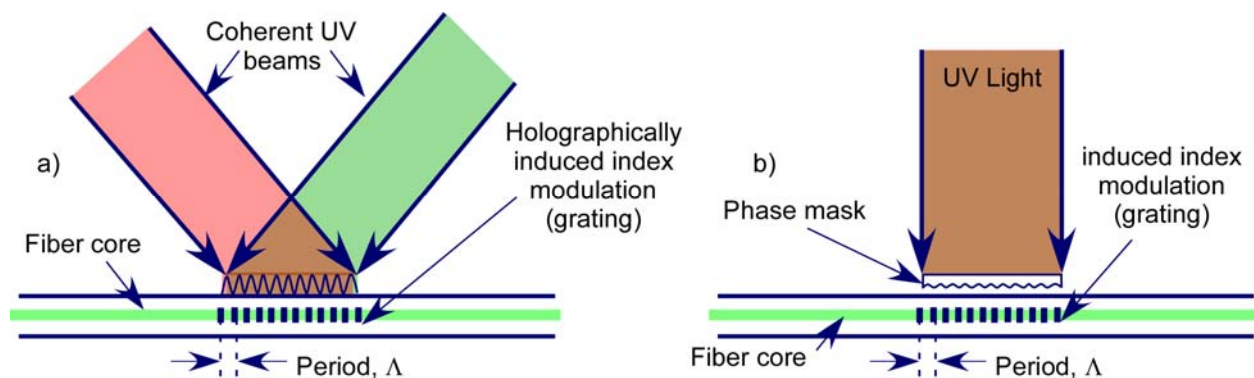


Figure 2-15. FBG fabrication based on a) holographic and b) phase mask exposure

When light is transmitted through a FBG, multiple Fresnel reflections resulting from the period of the refractive-index profile formed in the core take place along the length of the grating. This narrow band reflection has the strongest interaction or mode-coupling at the Bragg wavelength, λ_B , which is given by

$$\lambda_B = 2 \cdot n \cdot \Lambda \quad (2-4)$$

where n is the modal index and Λ is the grating period. Any change in fiber properties such as caused by strain or temperature, will change the Bragg wavelength. By measuring the shift in the reflected wavelength, one can determine the external stimulus applied (see Figure 2-16).

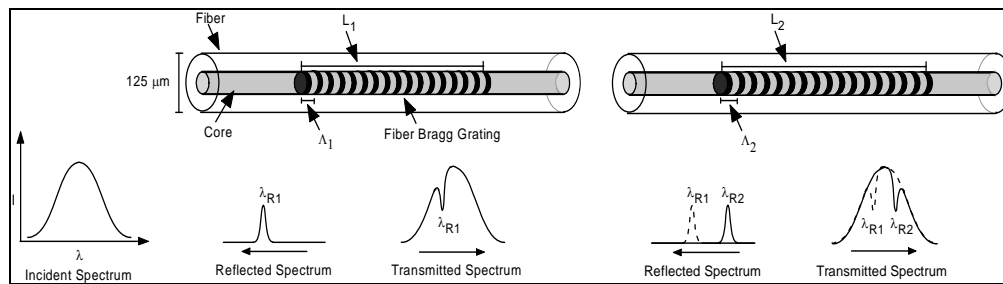


Figure 2-16 Diagram of the operation of a FBG

An applied strain to the optical fiber in the vicinity of the FBG will cause the Bragg wavelength to shift through dilating or compressing the grating and changing the effective index. The resulting shift is given by⁶³:

$$\frac{\delta\lambda_B}{\lambda_B} = \varepsilon_1 - \left(\frac{n^2}{2}\right) \cdot [p_{11}\varepsilon_t + p_{12} \cdot (\varepsilon_1 + \varepsilon_t)] \quad (2-5)$$

where ε_1 and ε_t are the principle strain components along the fiber axis and transverse to the fiber axis, p_{ij} are the Pockel's coefficients and $\delta\lambda_B$ is the change in Bragg wavelength. For homogeneous and isotropic strain conditions, equation (2-5) reduces to⁶³:

$$\frac{\delta\lambda_B}{\lambda_B} = [1 - p_e] \cdot \varepsilon \quad \cong 0.78 \cdot \varepsilon \quad (2-6)$$

where the photo-elastic contributions to p_e have been subsumed. P_e is defined by⁶³:

$$p_e = n/2 \cdot [p_{12} - \mu \cdot (p_{11} + p_{12})] \quad (2-7)$$

where μ is the Poisson ratio. The strain response has been determined to be linear with no evidence of hysteresis at temperatures as high as 370 °C⁶⁴.

The temperature sensitivity of a bare fiber is primarily due to the thermo-optic effect given by⁶³:

$$\frac{\delta\lambda_B}{\lambda_B} = \alpha + \frac{1}{n} \cdot \frac{dn}{dT} \cong 6.7 \times 10^{-6} / ^\circ\text{C} \quad (2-8)$$

where $\frac{dn}{dT}$ is the rate of change of the refractive index with respect to temperature. A typical response rate for light propagated at 1550nm is 0.01nm/°C. Figure 2-17 shows the thermal response of FBGs over a range of temperatures showing a slight second-order contribution as one approaches 900 °C.

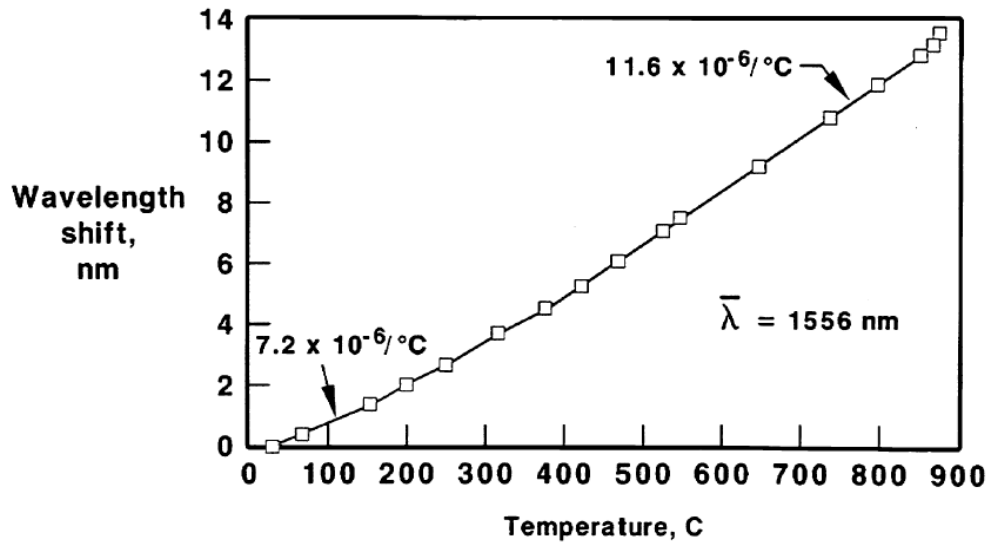


Figure 2-17. Bragg grating thermal sensitivity at elevated temperatures

Overall, FBGs have been used as sensors in a wide variety of applications, and they are generally accepted as being among the most viable of optical sensing platforms^{65,66}.

2.3.2.2 Wavelength Division Multiplexing on fiber Bragg gratings

The use of wavelength division multiplexing (WDM) for the demodulation of FBG's has been successfully implemented for various sensing applications⁶⁷. WDM as applied to FBG's requires that each grating have a reflected spectrum in a wavelength domain that is different from any other FBG within the array set as illustrated in Figure 2-18. WDM systems typically require FBG sensors to operate in a distinct wavelength window, with the elements arranged such that their operational regions do not overlap. The maximum number of FBG sensors on a single optical path that can be interrogated is a function of the optical bandwidth of the light source, the operation range of each FBG sensor and the tuning range of the tunable filter. The typical

number of FBG sensors that can be dealt with by a WDM interrogation unit is about 40, with the key limitation determined by the optical bandwidth of the light source.

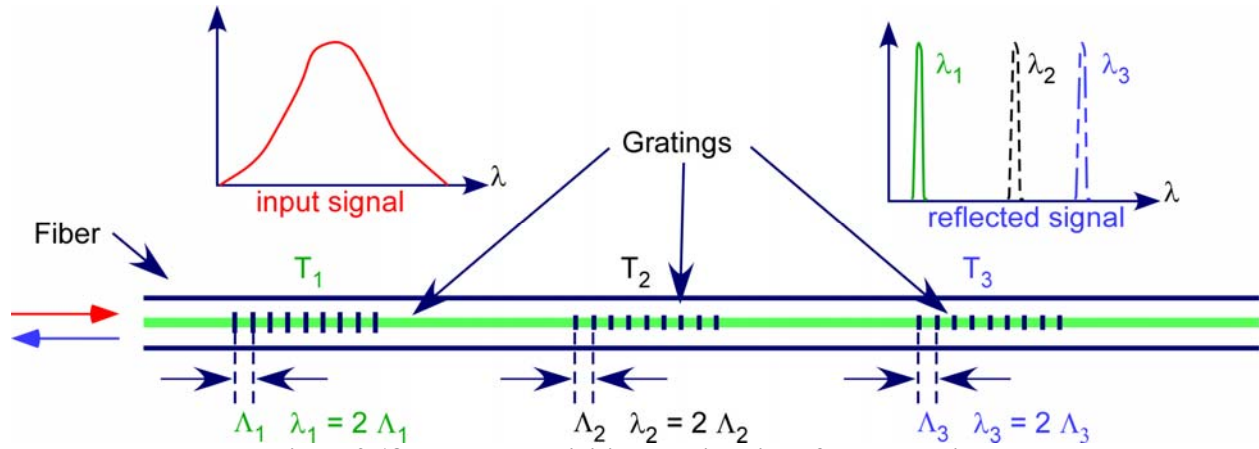


Figure 2-18 Wavelength division multiplexing of Bragg gratings

2.3.2.3 Optical Frequency Domain Reflectometry on fiber Bragg gratings

The OFDR technique has been successfully implemented to a quasi-distributed sensing platform utilizing Fiber Bragg Gratings (FBG)^{68,69,70,71,72,73}. A basic diagram of an OFDR system as applied to FBG's is shown in Figure 2-19a). Again, the gratings are interrogated with a swept-wavelength source⁷⁴.

When implementing the OFDR technique to FBG's, each grating (G_1 - G_n in Figure 2-19a) is spaced a unique distance (L_1 - L_n) from a broadband reference reflector (R). In this way, each grating/reference-reflector combination forms an interferometer with a unique optical path length (L_n). This interference modulates the reflected spectrum of each grating with a unique beat frequency (f_1 - f_n in Figure 2-19c) that is directly proportional to the path difference, L_n .

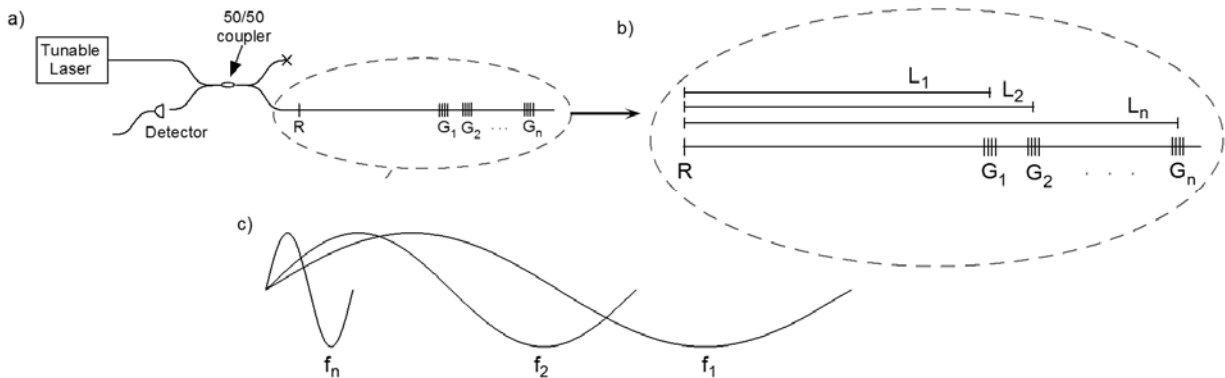
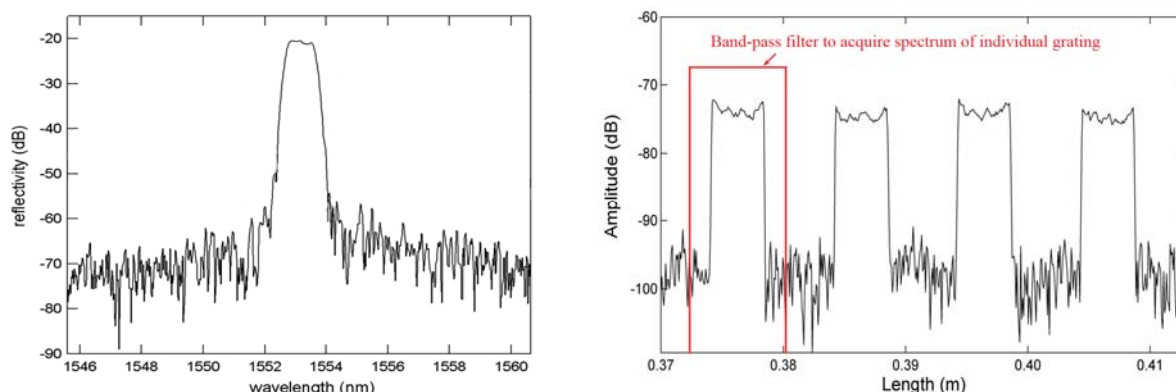


Figure 2-19 The basics of OFDR. a) Schematic representation of the OFDR network. b) Each sensor (G_1, G_2, \dots, G_n) forms an interferometer with the reference reflector (R). c) The interference causes the signal from each sensor to be modulated by a unique frequency (f_1, f_2, \dots, f_n)

During signal acquisition, the optical source is swept through a pre-determined wavelength range traversing the designed reflectance of the FBG's under interrogation. The spectrum of all the reflective elements in the FBG strand is acquired by an optical detector. An example of such output is illustrated in Figure 2-20a. A Fourier Transform applied to the spectrum yields a reflectivity curve as a function of spatial frequency, corresponding to the unique frequency due to the optical path length difference of the reflective element and the broad band reflector as depicted in Figure 2-20b. The response spectrum of each grating may then be uniquely obtained by applying a band-pass filter to window the signal. An inverse transform is then performed. The center wavelength of the each grating's reflected spectrum may then be determined. The shift in center wavelength from the nominal center wavelength can then be interpreted to determine the applied stimulus.



a) Spectrum captured during FBG interrogation

b) The Fourier transform of raw data

Figure 2-20. Data acquisition using the OFDR technique on fiber Bragg gratings

Using this demodulation technique, gratings are not required to have high reflectivity or different nominal wavelengths, but can be extremely weakly reflecting (0.04% or -34 dB is typical) and have overlapping reflectance spectra. Because of this and the high sensitivity of the coherent detection scheme, OFDR has three primary advantages over other distributed sensing techniques. First, since all the gratings can be written at the same wavelength, they can be written in-line as the fiber is being drawn, greatly simplifying fabrication by automating the process and considerably reducing the cost per sensor (from approximately \$400/FBG to approximately \$4/FBG)⁷⁵. Second, significantly more sensors, 10,000's instead of 10's, can be multiplexed in a single fiber than is possible using other demodulation and fabrication techniques, and the number of sensors does not affect the dynamic range of the measurement, unlike with the WDM technique. Finally, high spatial resolution is easily achievable using the OFDR technique. One

centimeter is routine, but the resolution can be made as fine or as coarse as desired, within the limits of the sensor gage length.

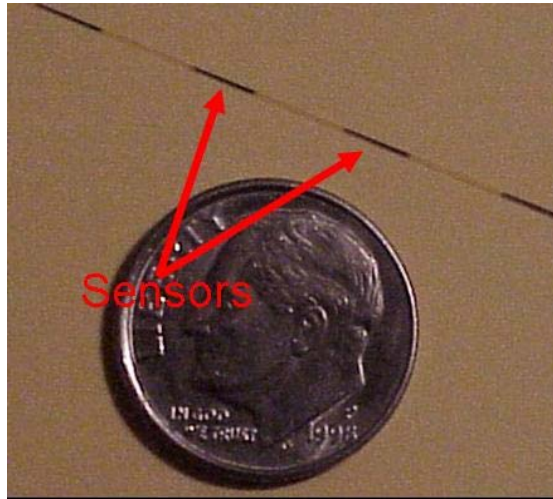


Figure 2-21. An optical fiber containing an FBG array (a.k.a. – ‘sensing fiber’).

Additional benefits are a narrowing of the laser spectrum necessary for complete detection and a widening of the dynamic range of the parameter being measured. In addition, multiple sensing strings can easily be multiplexed into the same demodulation system by using 2 x 2 couplers to split the laser power between the pathways, thus enabling a multi-channel system. OFDR technology, therefore, enables measurements from vast sensor arrays with a single system, and it makes practical distributed sensing on a scale and with a resolution that is vital for multiple sensing applications.

2.3.2.4 Optical Frequency Domain Reflectometry on Rayleigh backscatter

The OFDR technique may be extended to the measurement of Rayleigh backscatter in an optical fiber. The technique is similar in form and function to OFDR on fiber Bragg gratings as discussed in Section 2.3.2.3 above. The OFDR technique provides both the high spatial resolution and the sensitivity necessary to obtain the coherent Rayleigh scatter profile⁷⁶. The measurement network used to acquire the amplitude and phase of the Rayleigh backscatter signature as a function of fiber length is shown in Figure 2-22. This simplified network, used in the Optical Backscatter Reflectometer, a commercial instrument sold by Luna Technologies, has modifications to enable polarization diversity.

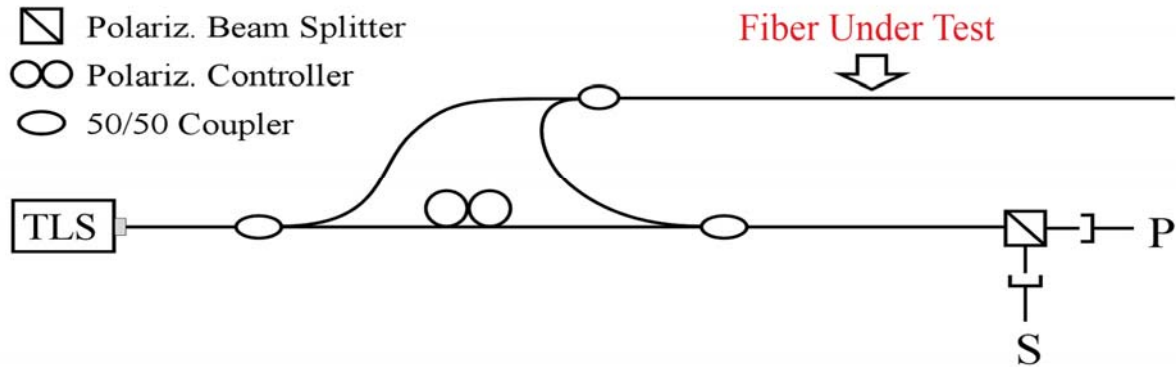


Figure 2-22. Optical network used for polarization-diverse measurement of Rayleigh backscatter.

Light from an external-cavity, tunable laser source (TLS) is split between the reference and measurement arms of an interferometer. In the measurement path, a 50/50 coupler further splits the light to interrogate a length of fiber under test (FUT) and returns the reflected light. Another 50/50 coupler then recombines the measurement and reference fields. A polarization beam splitter (PBS) and a polarization controller (PC) are used to split the reference light evenly between two orthogonal polarization states. As the laser is linearly tuned in frequency, the interference between the measurement field and the reference field is recorded at detectors labeled S and P. This polarization diversity technique is used in OFDR to mitigate signal fading due to polarization misalignment of the interfering measurement and local-oscillator fields. Not shown in the figure is an auxiliary interferometer used to trigger data acquisition in equal optical frequency increments. Also not shown is a portion of the network wherein a Hydrogen cyanide (HCN) gas-cell is used to monitor the absolute wavelength of the scanning laser. A typical trace obtained using the aforementioned technique is seen in Figure 2-23. The data was taken using the Optical Backscatter Reflectometer (OBR). No averaging was performed to achieve this data, however it was spatially filtered with an effective bandwidth of approximately 10 mm.

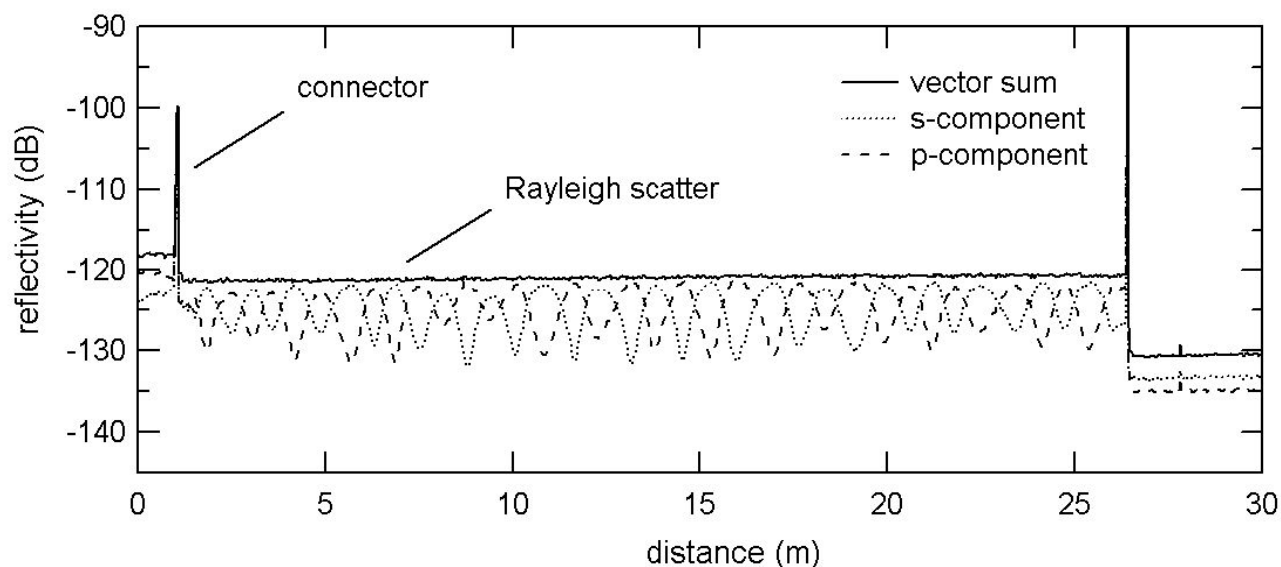
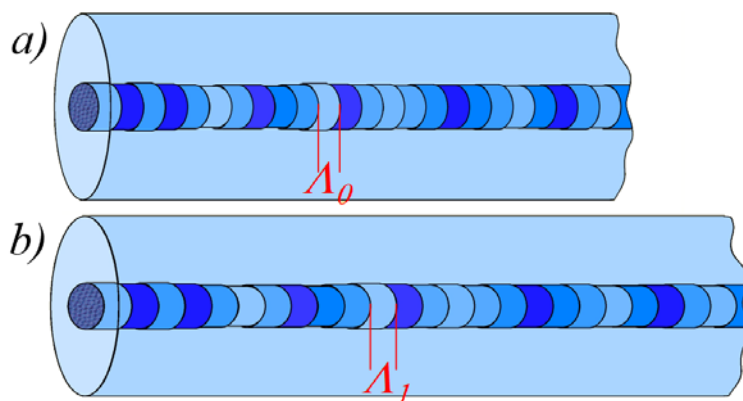


Figure 2-23 The reflectivity of a 25 meter spool (5 cm radius) of standard single-mode fiber.

The top trace is the vector sum of the S and P components of the Fourier transform of the interference signals measured on the two detectors shown in Figure 2-22. The oscillations in the S and P curves are caused by birefringence (or PMD) induced in the fiber due to coiling.

2.3.2.4.1 Sensing using Rayleigh scatter

Rayleigh backscatter for a given fiber has random, but static, scatter amplitude and phase patterns as a function of distance and they can be modelled as a long, weak FBG with a varying amplitude and a random spatial period as illustrated in Figure 2-24a). Changes in the local period of the Rayleigh scatter caused by an external stimulus like strain or temperature will cause fiber elongation (as shown in Figure 2-24b), which, in turn cause shifts in the locally reflected spectrum. These local spectral shifts can then be calibrated and assembled to form a distributed strain or temperature measurement.

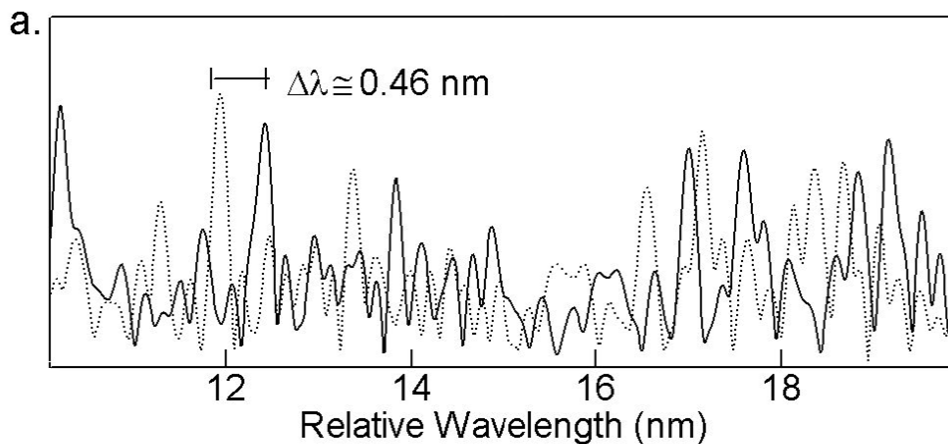


a) baseline, prior to any external perturbations b) After external stimulus, such as temperature

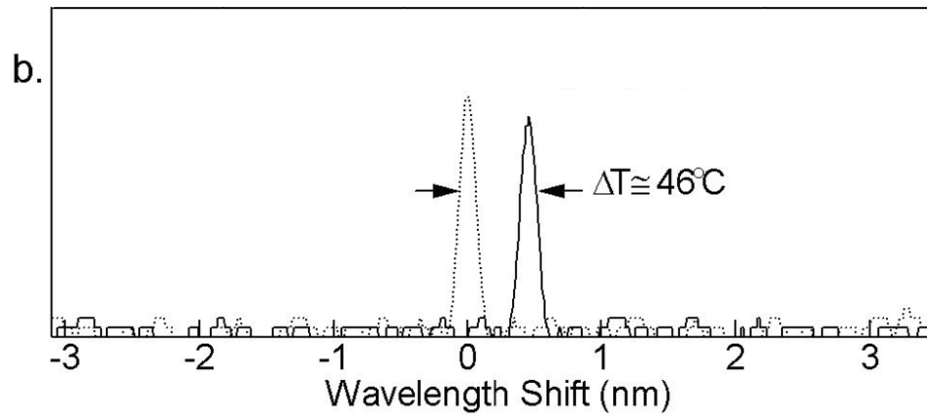
Figure 2-24. Rayleigh backscatter random reflection features

A distributed sensor is formed by first measuring and storing the Rayleigh scatter signature of the FUT at an ambient temperature and null strain state (nominally called a reference scan). The scatter profile is then measured at a later time with a strain or temperature perturbation applied to the fiber. The complex data sets from each detector, S and P, are broken into segment lengths Δs along the FUT and Fourier transformed into the optical frequency domain. A vector sum of the S and P spectra is then calculated to generate a polarization-independent spectrum associated with each interval. To determine the spectral shift between the reference and perturbed scans, a cross-correlation is performed for each FUT interval. Any change in strain or temperature manifests as a shift in the correlation peak. A distributed measurement is formed by compiling the spectral shifts for each interval along the FUT.

Figure 2-25a shows the fiber Rayleigh backscatter spectra along a 5mm segment for a reference scan at ambient temperature and scan of the same fiber interval after heating. Figure 2-25b then shows the cross-correlation with the reference spectrum for a measurement scan with and without temperature shift. The spectral difference between the shifted peak and the un-shifted peak is directly proportional to the temperature shift in this fiber interval.



a). Wavelength spectra along a 5 mm fiber interval for a heated (solid) and unheated (dotted) measurement scan.



b). Cross-correlation of the heated spectra with reference (unheated) spectrum.

Figure 2-25. Demonstration of a Thermal shift of an optical fiber

In summary, various distributed measurement techniques have been discussed ranging from quasi-distributed, time-domain based measurements to highly distributed coherent techniques. The goal of this discussion is to give the reader a general understanding of current, commonly used distributed sensing methods. Of particular interest is the Optical Frequency Domain Reflectometry (OFDR) based on Rayleigh scatter measurements. This technique will form the foundation from which the present distributed vibration measurement sensor will be based, and it will be discussed in detail in the following chapter as a part of an analysis of Rayleigh scatter.

3 An Analysis of Rayleigh Scattering

In this chapter, a mathematical discussion of the basis of the measurement of Rayleigh scattering will be presented. The work will begin with a demonstration of a single reflection, before extending to distributed reflections over a defined region. Comparison to laboratory data will be presented to supplement data generated by a Rayleigh scatter simulation model.

A simplified, representative optical network illustrating optical frequency domain reflectometry will be used as the basis of the analysis. The presentation will form the foundation of the work performed in this study; equations given herein will be referenced in forthcoming chapters.

3.1 Single point reflection Analysis

3.1.1 Introductory analysis

Two initially important parameters are propagation number, k , and angular frequency, ω . k is a function of energy source wavelength λ , and is defined as:

$$k = \frac{2\pi}{\lambda} \quad (3-1)$$

Similarly, the angular frequency is defined as a function of the source wavelength or frequency as given in equation (3-2)

$$\omega = \frac{2 \cdot \pi}{T} = 2 \cdot \pi \cdot f = \frac{2 \cdot \pi \cdot c}{\lambda} \quad (3-2)$$

Representing k as a function of angular frequency ω using equations (3-1) and eqn. (3-2) results in:

$$\omega = k \cdot c \quad (3-3)$$

$$k = \frac{\omega}{c} \quad (3-4)$$

To account for dispersion effects, the functional relationship of the propagation number to angular frequency becomes approximately linear such that:

$$k(\omega) \approx k_0 + \frac{n_{eff}}{c} \cdot \omega \quad (3-5)$$

where k_0 is the starting propagation constant and n_{eff} is the effective group index of refraction of the fiber. For the sake of simplicity and brevity, k_0 will be neglected such that:

$$k(\omega) = \frac{n_{eff}}{c} \cdot \omega \quad (3-6)$$

Assuming that the laser scan is a linear function of time, ω can be defined as:

$$\omega(t) = \alpha \cdot t + \omega_0 \quad (3-7)$$

where α is the rate of change of angular frequency (i.e. the laser frequency sweep rate) and ω_0 is the starting angular frequency.

k can therefore be stated to be function of time. Utilizing equation (3-7), equation (3-6) is recast, resulting in:

$$k(t) = \frac{n_{eff}}{c} \cdot \omega(t) \quad (3-8)$$

$$k(t) = \frac{n_{eff}}{c} \cdot (\alpha \cdot t + \omega_0) \quad (3-9)$$

3.1.2 Single point Simulation Derivation

The single point derivation begins with a Michelson interferometer, a simplified, unbalanced optical network commonly used for OFDR measurement. For this analysis, the interferometer is presumed to have partially reflecting mirrors at the end of each optical path as shown in Figure 3-1. A tunable laser is the source of optical energy of field intensity E_0 . The propagation of the energy is now tracked through the optical network.

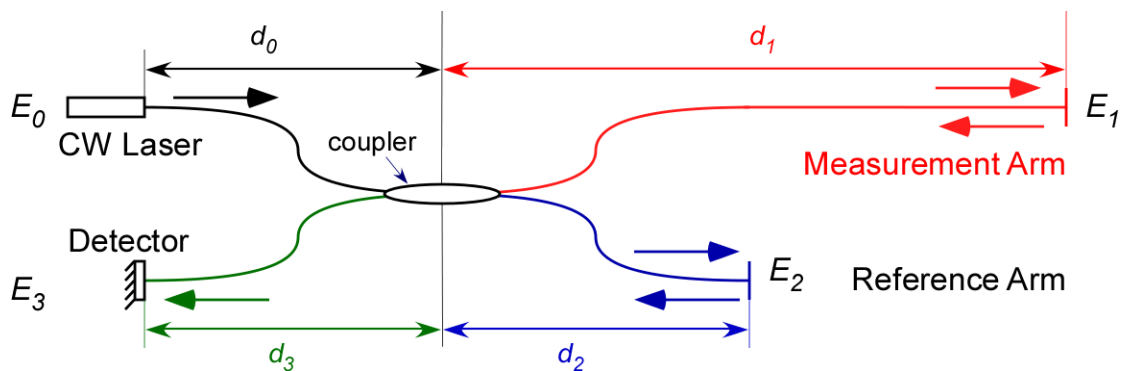


Figure 3-1. A basic Michelson Interferometer in optical fiber

On exiting the laser, the wave-front propagates down an optical path to a coupler where it is divided into two segments, with field intensity E_1 and E_2 . The optical energy is reflected from the end of the optical paths and is then recombined and measured by an optical detector. The

resulting optical field intensity as seen by the detector E_3 , is the linear superposition of E_1 and E_2 shown as:

$$E_3 = E_1 + E_2 \quad (3-10)$$

To develop a better understanding of the interference, let us represent the general field intensity E as a 1-dimensional complex function of both space and time such that:

$$E(x, t) = E_0 \cdot e^{i(k \cdot x - \omega t)} \quad (3-11)$$

where E_0 is the laser field intensity and quantities x and t are the position and time variables respectively.

In, this investigation, the path lengths are fixed, resulting in the optical energy equation being only a function of time. Utilizing equation (3-11), the optical field intensities E_1 and E_2 from the two different paths can be defined as:

$$E_1(t) = \underbrace{E_0 \cdot \rho_1}_{E_1} \cdot e^{i\phi_1(t)} \quad (3-12)$$

$$= E_1 \cdot e^{i\phi_1(t)}$$

$$E_2(t) = \underbrace{E_0 \cdot \rho_2}_{E_2} \cdot e^{i\phi_2(t)} \quad (3-13)$$

$$= E_2 \cdot e^{i\phi_2(t)}$$

where E_1 and E_2 are the electric field amplitude scaling due to reflectivity of the reflections on the measurement and reference arm of the interferometer. The phase terms $\phi_1(t)$ and $\phi_2(t)$ are defined as:

$$\phi_1(t) = k(t) \cdot L_1 - \omega \cdot t \quad (3-14)$$

$$\phi_2(t) = k(t) \cdot L_2 - \omega \cdot t \quad (3-15)$$

Here, L_1 is the path length from the source to end reflector of the measurement arm and back to the optical detector, and it is represented analytically as:

$$L_1 = d_0 + 2d_1 + d_3 \quad (3-16)$$

L_2 is the path length from the source to the reference arm reflection and back to the detector, also defined as:

$$L_2 = d_0 + 2d_2 + d_3 \quad (3-17)$$

The detector measures the irradiance I , which is proportional to the square of the amplitude of the optical field, and it is defined in equation (3-18) below.

$$I = \varepsilon \cdot \nu \cdot E^2 \quad (3-18)$$

Here, ε is the permittivity of the material and ν is the electromagnetic wave speed. Since ε and ν simply scale the results but do not affect the equation development, the terms will be assumed to be equal to 1 such that:

$$I = E^2 \quad (3-19)$$

By applying equation (3-19) to (3-10), the irradiance measured by the is:

$$I_3 = E_3^2 \quad (3-20)$$

$$= (E_1 + E_2)^2 \quad (3-21)$$

$$= (E_1 + E_2)(E_1 + E_2) \quad (3-22)$$

$$= (E_1^2 + E_2^2 + E_1 E_2^* + E_1^* E_2) \quad (3-23)$$

$$= I_1 + I_2 + \underbrace{(E_1 E_2^* + E_1^* E_2)}_{I_{INT}} \quad (3-24)$$

Examining the results of equation (3-24), the irradiation measured by the detector consists the sum of the irradiation down the two optical paths and an interference component I_{INT} . To gain a further understanding of (3-24), the interference term, I_{INT} is expanded.

Applying equations (3-12) and (3-13) to I_{INT} in eqn. (3-24) results in:

$$I_{INT} = E_1 \cdot e^{i\phi_1(t)} \cdot E_2 \cdot e^{-i\phi_2(t)} + E_1 \cdot e^{-i\phi_1(t)} \cdot E_2 \cdot e^{i\phi_2(t)} \quad (3-25)$$

$$= E_1 \cdot E_2 \cdot e^{i(\phi_1(t) - \phi_2(t))} + E_1 \cdot E_2 \cdot e^{-i(\phi_1(t) - \phi_2(t))} \quad (3-26)$$

$$= E_1 \cdot E_2 \cdot (e^{i(\phi_1(t) - \phi_2(t))} + e^{-i(\phi_1(t) - \phi_2(t))}) \quad (3-27)$$

Equation (3-27) can be simplified further by utilizing the trigonometric identity $2 \cdot \text{Cos}(\theta) = e^{i\theta} + e^{-i\theta}$. Letting $\theta = \phi_1(t) - \phi_2(t)$, the equation expansion results in:

$$I_{INT} = E_1 \cdot E_2 \cdot \underbrace{\left(e^{i(\phi_1(t) - \phi_2(t))} + e^{-i(\phi_1(t) - \phi_2(t))} \right)}_{2 \cdot \text{Cos}(\phi_1(t) - \phi_2(t))} \quad (3-28)$$

$$= 2 \cdot E_1 \cdot E_2 \cdot \text{Cos}(\phi_1(t) - \phi_2(t)) \quad (3-29)$$

Substituting equation (3-14) and (3-15) into equation (3-29) results in:

$$I_{INT} = 2 \cdot E_1 \cdot E_2 \cdot \text{Cos}(k(t) \cdot (L_1 - \omega \cdot t) - k(t) \cdot (L_2 - \omega \cdot t)) \quad (3-30)$$

$$= 2 \cdot E_1 \cdot E_2 \cdot \text{Cos}(k(t) \cdot [(L_1 - \omega \cdot t) - (L_2 - \omega \cdot t)]) \quad (3-31)$$

$$= 2 \cdot E_1 \cdot E_2 \cdot \text{Cos}(k(t) \cdot [L_1 - \omega \cdot t - L_2 + \omega \cdot t]) \quad (3-32)$$

$$= 2 \cdot E_1 \cdot E_2 \cdot \text{Cos} \left(k(t) \cdot \left(\underbrace{L_1}_{d_0 + 2d_1 + d_3} - \underbrace{L_2}_{d_0 + 2d_2 + d_3} \right) \right) \quad (3-33)$$

$$= 2 \cdot E_1 \cdot E_2 \cdot \text{Cos}(k(t) \cdot ((d_0 + 2d_1 + d_3) - (d_0 + 2d_2 + d_3))) \quad (3-34)$$

$$= 2 \cdot E_1 \cdot E_2 \cdot \text{Cos} \left(2 \cdot k(t) \cdot \underbrace{(d_1 - d_2)}_{\Delta x} \right) \quad (3-35)$$

Applying equation (3-9) to equation (3-35):

$$I_{INT} = 2 \cdot E_1 \cdot E_2 \cdot \text{Cos} \left(\left(\frac{2 \cdot n_{eff}}{c} \cdot (\alpha \cdot t + \omega_0) \right) \cdot \Delta x \right) \quad (3-36)$$

$$= 2 \cdot E_1 \cdot E_2 \cdot \text{Cos} \left(\underbrace{\frac{2 \cdot n_{eff}}{c} \cdot \Delta x}_{\Delta \tau} \cdot (\alpha \cdot t + \omega_0) \right) \quad (3-37)$$

$$= 2 \cdot E_1 \cdot E_2 \cdot \text{Cos} \left(\alpha \cdot \Delta \tau \cdot t + \underbrace{\Delta \tau \cdot \omega_0}_{\theta} \right) \quad (3-38)$$

$$= 2 \cdot E_1 \cdot E_2 \cdot \text{Cos}(\alpha \cdot \Delta \tau \cdot t + \theta) \quad (3-39)$$

Equation (3-19) can be substituted into equation (3-39) resulting in:

$$I_{INT} = 2 \cdot \underbrace{E_1}_{E_1 = \sqrt{I_1}} \cdot \underbrace{E_2}_{E_2 = \sqrt{I_2}} \cdot \text{Cos}(\alpha \cdot \Delta \tau \cdot t + \theta) \quad (3-40)$$

$$= 2 \cdot \sqrt{I_1 \cdot I_2} \cdot \text{Cos}(\alpha \cdot \Delta \tau \cdot t + \theta) \quad (3-41)$$

At this point, one can express a unified equation for the light energy as seen by the detector by applying equation (3-41) to equation (3-24) such that:

$$I_3(t) = I_1 + I_2 + 2 \cdot \sqrt{I_1 \cdot I_2} \cdot \text{Cos}(\alpha \cdot \Delta\tau \cdot t + \theta) \tag{3-42}$$

Reviewing the results thus far, it is clear that the optical energy as seen by the detector has a constant contribution of irradiance from the reference and measurement optical paths and a time dependent component that varies as the function of the cosine of the product of the wavelength and the optical path length (OPL) difference.

Examining equation (3-42), the OPL difference linearly modulates the frequency of the signal, such that an increase in distance results in an increase in the modulation frequency as illustrated in Figure 3-2.

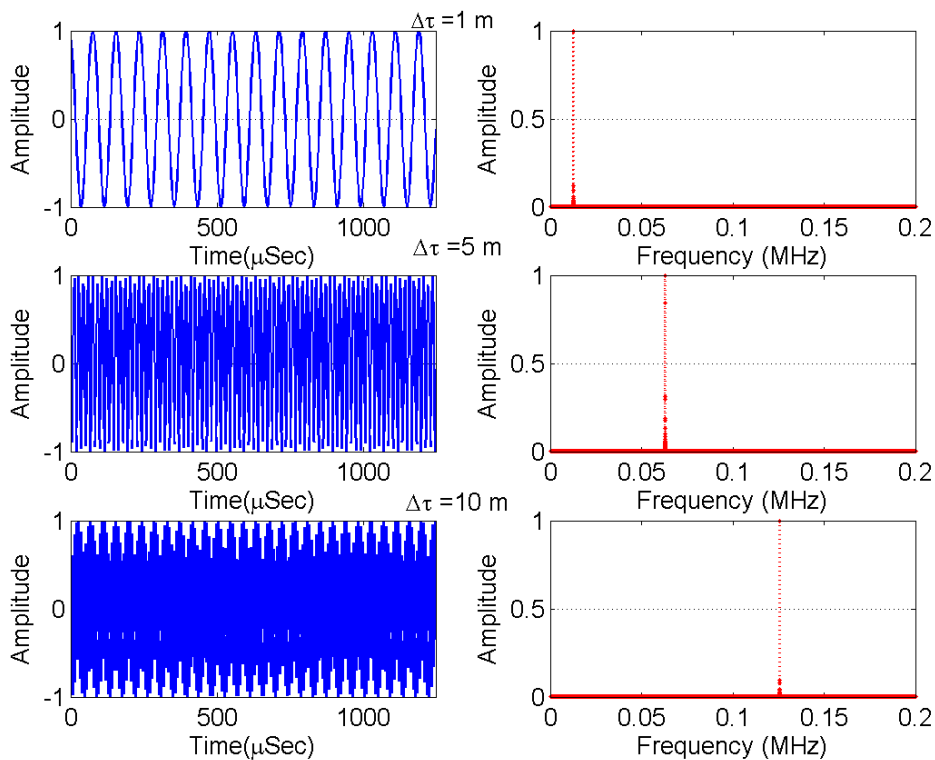


Figure 3-2. Wavelength and Frequency of an unbalanced Michelson interferometer with different optical path length differences with nominally similar end reflections

Figure 3-2 was produced by ignoring the DC terms expressed in (3-42). To further simplify the formulation, the amplitude scaling is assumed to be $2 \cdot \sqrt{I_1 \cdot I_2} \approx 1$ such that;

$$I_3(t) = \text{Cos} \left(\underbrace{\frac{2 \cdot n_{eff} \cdot \Delta x}{c}}_{\Delta\tau} \cdot (\alpha \cdot t + \omega_0) \right) \tag{3-43}$$

$$= \text{Cos}(\Delta\tau \cdot (\alpha \cdot t + \omega_0)) \quad (3-44)$$

3.2 Distributed reflection Analysis

The distributed reflection analysis will be performed using two methods. The first section will perform a theoretical analysis using Coupled-mode theory, a mathematical approach commonly used for the analysis of electromagnetic wave propagation and interaction with media. A thorough review of the concept is presented in Refs. 77 and 78. A derivation will then be done in a similar fashion to that in section 3.1.2 resulting in equations that will be used in the multi-reflection simulation model, which will form the basis of the static and dynamic strain investigation to be discussed in the latter chapters of this document.

3.2.1 Coupled-Mode Theory derivation

Consider a continuum of multi-point reflections along the fiber under test (FUT) between 0 and L as depicted in Figure 3-3.

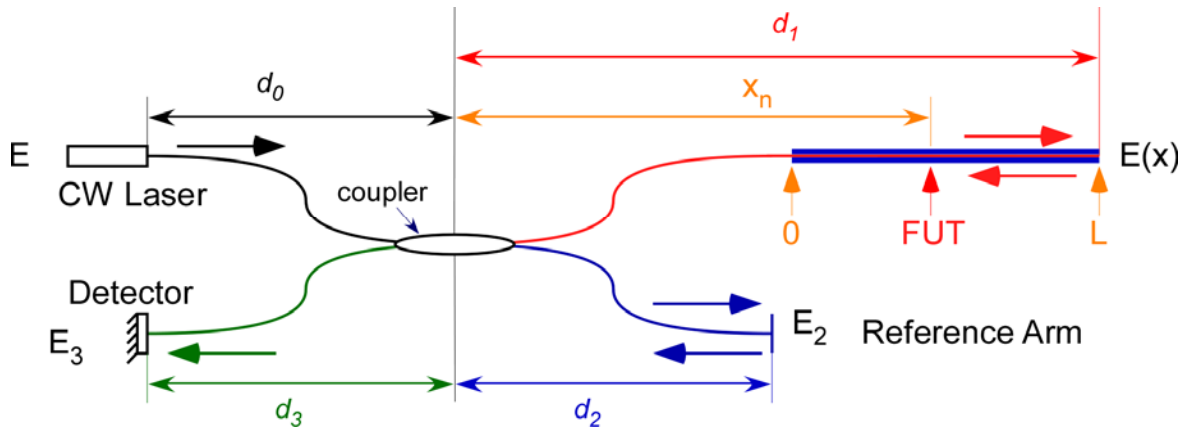


Figure 3-3. Optical network depicting distributed reflection

To further simplify equation development, the effect of the reference arm of the interferometer is included by defining $\tau = \tau_1 = \Delta\tau$. τ_2 is thus:

$$\tau_1 - \tau_2 = \Delta\tau \quad (3-45)$$

$$\Delta\tau - \tau_2 = \Delta\tau \quad (3-46)$$

$$\tau_2 = \Delta\tau - \Delta\tau \quad (3-47)$$

$$\tau_2 = 0 \quad (3-48)$$

As illustrated in Figure 3-4, as the field intensity E^+ traverses reflective zones inherent in the fiber, a small fraction of the energy proportional to the magnitude of the local reflective event is

reflected in the opposite direction toward the detector. This continuum of back reflection represents the Rayleigh backscatter of the fiber and is termed as $\kappa(x)$.

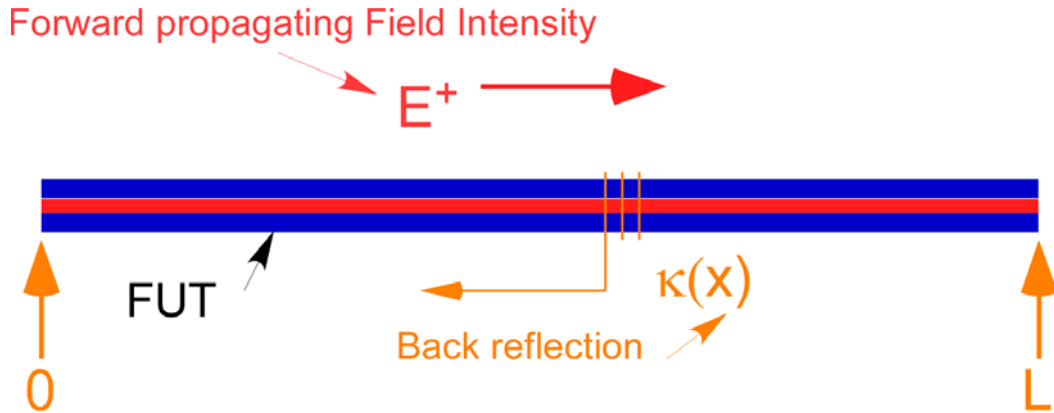


Figure 3-4. Optical network depicting detailed back reflection of Rayleigh scatter

Applying equation (3-11), the accumulated back reflected field intensity can be represented as the product of the back reflection function and the forward propagating field intensity as shown in equation (3-49) below:

$$E^-(0, \omega) = \int_0^L \underbrace{E_1 \cdot e^{-i \cdot k \cdot x}}_{E^+(x, \omega)} \cdot \kappa(x) \cdot dx \tag{3-49}$$

Equation (3-49) is expanded further by multiplying both sides of the equation by $\frac{E_2}{2\pi} \cdot e^{-i \cdot \omega \cdot \tau}$, the modulation term of the reference arm of the interferometer, and taking the integral from $-\infty$ to $+\infty$ resulting in the inverse Fourier transform of the total back-reflected field intensity as illustrated below:

$$\underbrace{\frac{1}{2\pi} \int_{-\infty}^{\infty} E^-(0, \omega) \cdot E_2 \cdot e^{-i \cdot \omega \cdot \tau} \cdot d\omega}_{IFFT(E^-(0, \omega))} = \frac{1}{2\pi} \int_{-\infty}^{\infty} \int_0^L E_1 \cdot \kappa(x) \cdot e^{-i \cdot k \cdot x} \cdot E_2 \cdot e^{-i \cdot \omega \cdot \tau} dx \cdot d\omega \tag{3-50}$$

The first-order dispersion approximation for the propagation number k as a function of angular frequency ω as defined in equation (3-5) can then be applied. It is important to note that the higher-order terms can be significant in influencing the measurements, but they are ignored here for simplicity. The integration limits are modified here such that $[0, L]$ extends to $[-\infty, \infty]$. This is possible by postulating that $\kappa(x)$ only exists between $[0, L]$ and is zero everywhere else. Equation (3-50) then becomes:

$$\mathfrak{F}^{-1}[E^-(0, \omega)] = \frac{1}{2\pi} \int_{-\infty}^{\infty} \int_{-\infty}^{\infty} E_1 \cdot \kappa(x) \cdot e^{-i \left(\frac{2 \cdot n}{c} \cdot x \right)} \cdot E_2 \cdot e^{-i \cdot \omega \cdot \tau} dx \cdot d\omega \quad (3-51)$$

$$= \frac{1}{2\pi} \int_{-\infty}^{\infty} E_1 \cdot E_2 \cdot \kappa(x) \cdot \int_{-\infty}^{\infty} e^{-i \left(\frac{2 \cdot n}{c} \cdot x + \tau \right) \cdot \omega} d\omega \cdot dx \quad (3-52)$$

$$= \frac{1}{2\pi} \int_{-\infty}^{\infty} E_1 \cdot E_2 \cdot \kappa(x) \cdot 2\pi \cdot \delta \left(\frac{2 \cdot n_{eff}}{c} \cdot x - \tau \right) \cdot dx \quad (3-53)$$

Examining equation (3-53) it is noted that the Dirac function, $\delta(y)$ has the value zero everywhere except at $y=0$ where, by definition, its value is infinitely large in such a way that its total integral is 1. Therefore, over the integration limits $[-\infty, \infty]$, the only non-zero value will occur when the quantity $t - \frac{2 \cdot n_{eff}}{c} x - \tau$ is equal to zero. Taking the inner quantities of the

Dirac function and solve for x results in:

$$0 = \frac{2 \cdot n_{eff}}{c} x - \tau \quad (3-54)$$

$$\frac{2 \cdot n_{eff}}{c} x = \tau \quad (3-55)$$

$$x = \frac{c}{2 \cdot n_{eff}} \tau \quad (3-56)$$

Evaluating the integral in equation (3-53) using the results from eqn. (3-56) it can be shown that:

$$IFFT(E^-(0, \omega)) = E_1 \cdot E_2 \cdot \kappa \left(\frac{c}{2 \cdot n_{eff}} \tau \right) \quad (3-57)$$

Equation (3-57), demonstrates that for distributed reflective events, the Fourier transform yields a continuum of reflective peaks located in the transform domain corresponding to the optical path length difference between the reflective event and the reference reflector. The amplitude of the reflected event is modulated by the forward propagating intensity from the source such as a tunable laser. The positional information in the transform domain is a spatial frequency that correlates to the physical location of the reflective event. Figure 3-5 shows a Fourier transform of a measurement signal where two partially reflecting mirrors are located at two locations, L_1 and L_2 on the FUT. The reflective events are clearly seen as distinct peaks with amplitudes

corresponding to the reflectivity of the event. The base signal at ~ -100 dB corresponds to the Rayleigh scatter of the FUT.

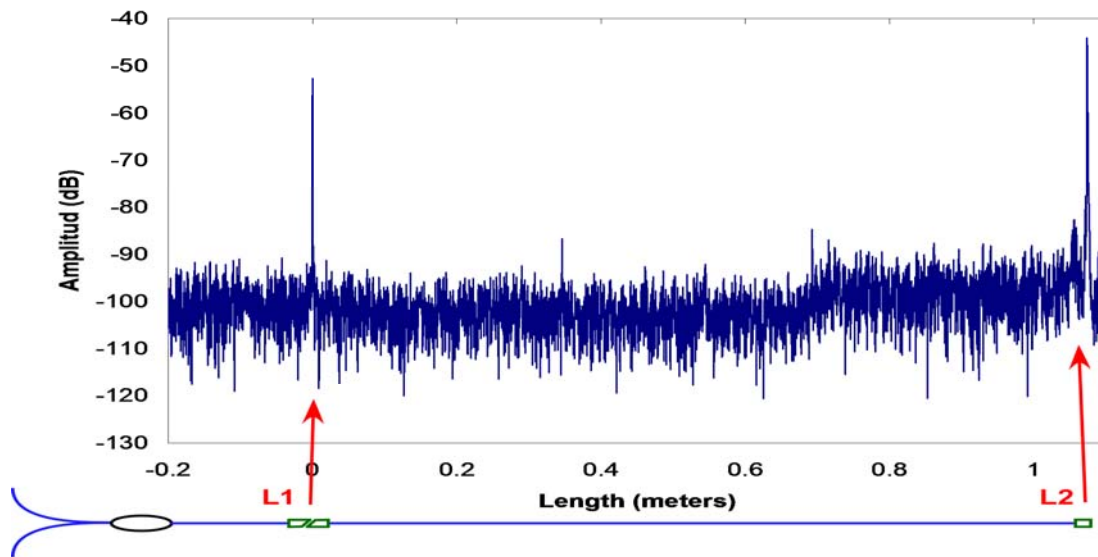


Figure 3-5. A distributed scan with two partially reflecting mirrors

3.2.2 Multi-point Simulation Derivation

To begin the simulation equation analysis, Figure 3-3 is referenced and is presented below for the reader’s convenience.

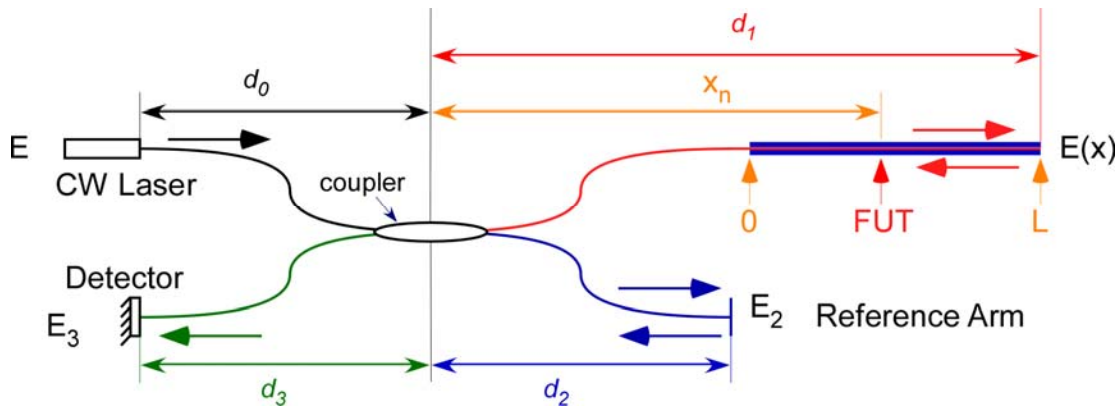


Figure 3-3. Optical network depicting distributed reflection

Recall that equation (3-10), defines the electric field as seen at the detector during system signal acquisition as the superposition of the electric field of the reference and measurement arms of the interferometer as shown below.

$$E_3 = E_1 + E_2 \tag{3-10}$$

E_I now represents a continuum of reflections along all points from 0 to L and hence will be defined as:

$$E_1(t) = \sum_n \underbrace{E_0 \cdot \rho_1^n}_{E_1^n} \cdot e^{i\phi_1^n(t)} \quad (3-58)$$

$$E_1(t) = \sum_n E_1^n \cdot e^{i\phi_1^n(t)}$$

where E_1^n represents the reflectivity along the core of the fiber at position x^n . The superscript n represents the index of the arrays in the summation. $\phi_1^n(t)$ is defined as:

$$\phi_1^n(t) = k \cdot L_1(x^n) \quad (3-59)$$

where $L_1(x^n)$ represents the optical path length from the source to point of reflection in the fiber under test and back to the detector, defined as:

$$L_1(x_n) = d_0 + d_3 + 2x^n \quad (3-60)$$

Recall that E_2 is defined as:

$$E_2(t) = E_2 \cdot e^{i\phi_2(t)} \quad (3-13)$$

Recall further that the irradiance as seen at the detector was shown to be a constant term, $I_1 + I_2$ and a time dependent intensity term, I_{INT} .

$$I_3 = I_1 + I_2 + \underbrace{(E_1 E_2^* + E_1^* E_2)}_{I_{INT}} \quad (3-24)$$

Like the single point derivation, the time dependent intensity term is of interest. Recasting I_{INT} for multi-reflection analysis results in:

$$I_{INT} = \sum_n [E_1^n \cdot e^{i\phi_1^n(t)}] \cdot E_2 \cdot e^{-i\phi_2(t)} + \sum_n [E_1^n \cdot e^{-i\phi_1^n(t)}] \cdot E_2 \cdot e^{i\phi_2(t)} \quad (3-61)$$

$$= \sum_n [E_1^n \cdot E_2 \cdot e^{i((\phi_1(t) - \phi_2^n(t)))}] + \sum_n [E_1^n \cdot E_2 \cdot e^{-i((\phi_1(t) - \phi_2^n(t)))}] \quad (3-62)$$

$$= \sum_n \left[E_1^n \cdot E_2 \cdot \underbrace{e^{i((\phi_1(t) - \phi_2^n(t)))} + e^{-i((\phi_1(t) - \phi_2^n(t)))}}_{2 \cdot \text{Cos}(\phi_1^n(t) - \phi_2(t))} \right] \quad (3-63)$$

$$= \sum_n \left[E_1^n \cdot E_2 \cdot 2 \cdot \text{Cos} \left(\underbrace{\phi_1^n(t) - \phi_2(t)}_{\Delta\phi^n(t)} \right) \right] \quad (3-64)$$

$$= 2 \cdot E_2 \cdot \sum_n \left[E_1^n \cdot \text{Cos}(\Delta\phi^n(t)) \right] \quad (3-65)$$

The phase differential follows as:

$$\Delta\phi^n(t) = \phi_1^n(t) - \phi_2(t) \quad (3-66)$$

$$= k(t) \cdot L_1(x^n) - k(t) \cdot L_2 \quad (3-67)$$

$$= k(t) \cdot (L_1(x^n) - L_2) \quad (3-68)$$

$$= k(t) \cdot ((d_0 + d_3 + 2x^n) - (d_0 + 2d_2 + d_3)) \quad (3-69)$$

$$= 2 \cdot k(t) \cdot (x^n - d_2) \quad (3-70)$$

A further expansion of the phase term can be attained by applying equation (3-9) to eqn. (3-70) resulting in:

$$\Delta\phi^n(t) = 2 \cdot \left(\frac{n_{eff}}{c} \cdot (\alpha \cdot t + \omega_0) \right) \cdot (x^n - d_2) \quad (3-71)$$

$$= \left(\frac{2 \cdot n_{eff}}{c} \cdot (\alpha \cdot t + \omega_0) \right) \cdot (x^n - d_2) \quad (3-72)$$

Applying equation (3-72) to eqn. (3-65), results in the final form of the time dependent intensity variation as shown below:

$$I_{INT} = 2 \cdot E_2 \cdot \sum_n \left[E_1^n \cdot \text{Cos} \left(\left(\frac{2 \cdot n_{eff}}{c} \cdot (\alpha \cdot t + \omega_0) \right) \cdot (x^n - d_2) \right) \right] \quad (3-73)$$

Using equation (3-73), multi-peak events in the FUT can be simulated as illustrated in Figure 3-6, where a series of simulated detector signals and the corresponding Fourier transforms of the events are depicted. Modeled therein was a series of 2, 4 and 6 events at optical path length differences corresponding to various combinations of 1m, 2m, 4m, 5m, 7m and 8m. The Fourier series x -axis has been scaled to position.

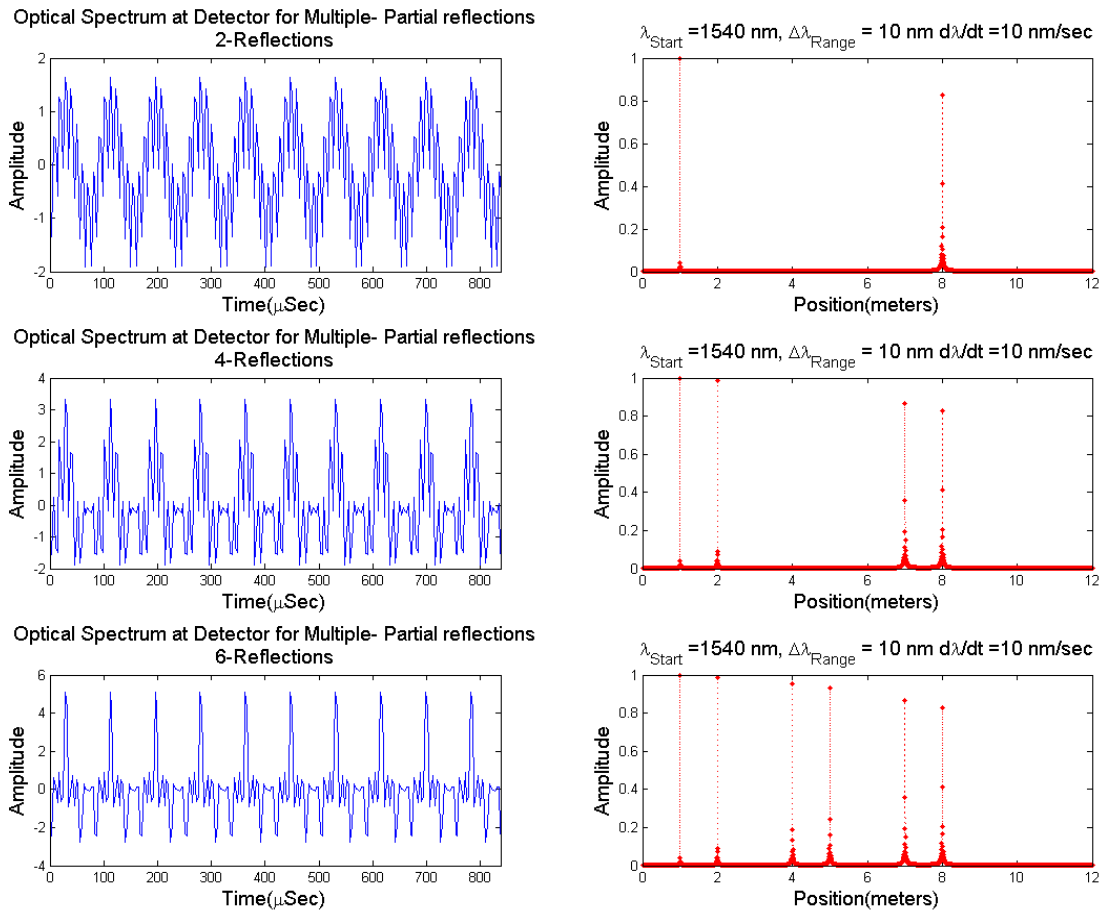


Figure 3-6. Simulated data showing the signal at the detector and the Fourier transform of the same.

If the reflection density between two points is increased to simulate a reflection continuum, the Fourier transform of the acquired signal will correspondingly show the reflection series.

Figure 3-7 and Figure 3-8 show the detector intensity and corresponding Rayleigh scatter generated using the simulation model based on equation (3-73). Here, a 33 cm fiber with a 20 micron spatial resolution was modeled. Reflective events at 3 cm and 30 cm were added to the model. The simulated laser parameters were a sweep rate of 10nm/sec, a range of 40nm and a center wavelength of 1550 nm.

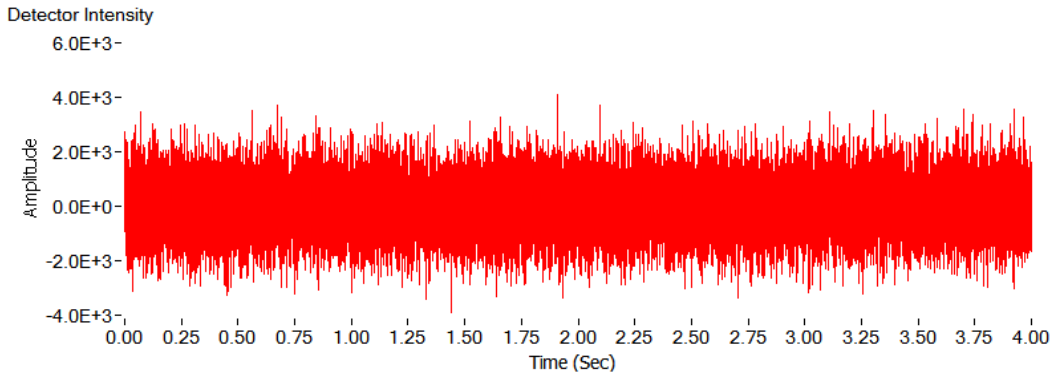


Figure 3-7. Detector intensity from simulation model of an optical fiber

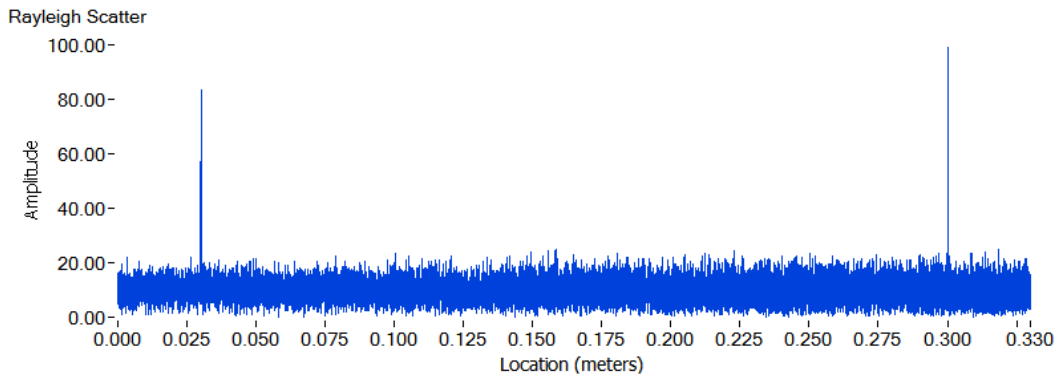


Figure 3-8. Rayleigh scatter from simulation model of an optical fiber

The data shown above was generated by creating positional and amplitude vectors representative of the Rayleigh scatter. The array, E_1^n was generated by producing a Gaussian white noise distribution to represent the location amplitudes. The reflection position array, x^n was generated to have a uniform spacing corresponding to the simulated system acquisition resolution. A uniform random signal of peak amplitude corresponding to half the acquisition resolution was then added to the array to simulate the random location about the mean of the reflective boundaries within the fiber. Figure 3-9 illustrates Rayleigh Scatter with comparative data sets where x^n is modeled with positional mean variance and equal spacing. It is necessary to include the uniform mean variance to the position array because the location of the reflective events occur at the atomic boundaries which are aperiodic. A uniform spacing would correspond to a Fiber Bragg grating signal simulation. The Fourier transform of the generated intensity signal yields the Rayleigh scatter of the fiber. This modeling schema will be used from this point forward.

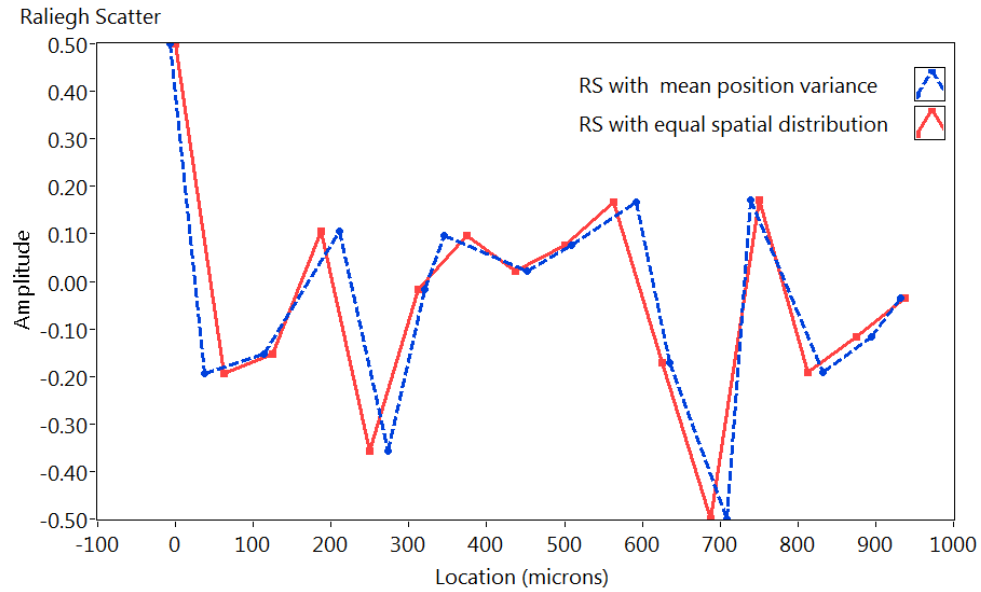


Figure 3-9. An illustration of the mean positional variance introduced to simulate Rayleigh scatter.

3.3 Summary

It has been shown that in OFDR, the positional information is encoded in the phase of the signal, whereas, the magnitude of the event is coupled to the signal amplitude. Similarly, an event that modulates or otherwise perturbs the fiber at that location, such as strain or vibration, is encoded in the phase of the signal.

4 Static Strain Theory

In this chapter, a presentation on the measurement of static strain will be documented as a precursor to dynamic strain (vibration) and is presentation of material available in the public domain. The discussion commences by tracing the data flow from the point of acquisition to the analysis and presentation of strain measurements. The analysis is supplemented with a numerical simulation as an aid to understanding the theoretical analysis.

4.1 Rayleigh Scatter Acquisition

Thus far, discussion has focused on the utility of OFDR for acquiring reflection as a function of position through the use of an interferometer has been presented. For review, a tuneable laser source is linearly swept through a finite wavelength range. The optical signal generated is transmitted through a reference and a measurement arm. A portion of the transmitted optical power is reflected back at spatial sites along the measurement and reference arm of the reflectometer. The mixed signal is then acquired at an optical detector. The Fourier transform of the detected signal, which is the aggregate spectral response of all reflective points along the fiber, yields the reflection as a function of position. This signal is considered the Rayleigh backscatter.

To better understand this backscattered optical signal, the effects of data acquisition with a tuneable source (Laser) with limited bandwidth are examined. The investigation begins by postulating that the reflective sites have a spatial distribution at the atomic level produced by interactions at the inter-atomic boundaries. It can also be stated that the amplitude and phase of the reflective sites are spatially random and static but, are spectrally functional. This simply translates to each reflective site having a defined, repeatable response to frequency.

Extending this discussion to a simulated data set, it is presumed that the detector has an infinite bandwidth relative to the Rayleigh scatter spectra such that all content to the atomic level is acquired in a 1mm domain as illustrated in Figure 4-1. For the simulation, the Rayleigh scatter is represented as a 262,144 length random array resulting in a 4 nm, 2-point resolution.

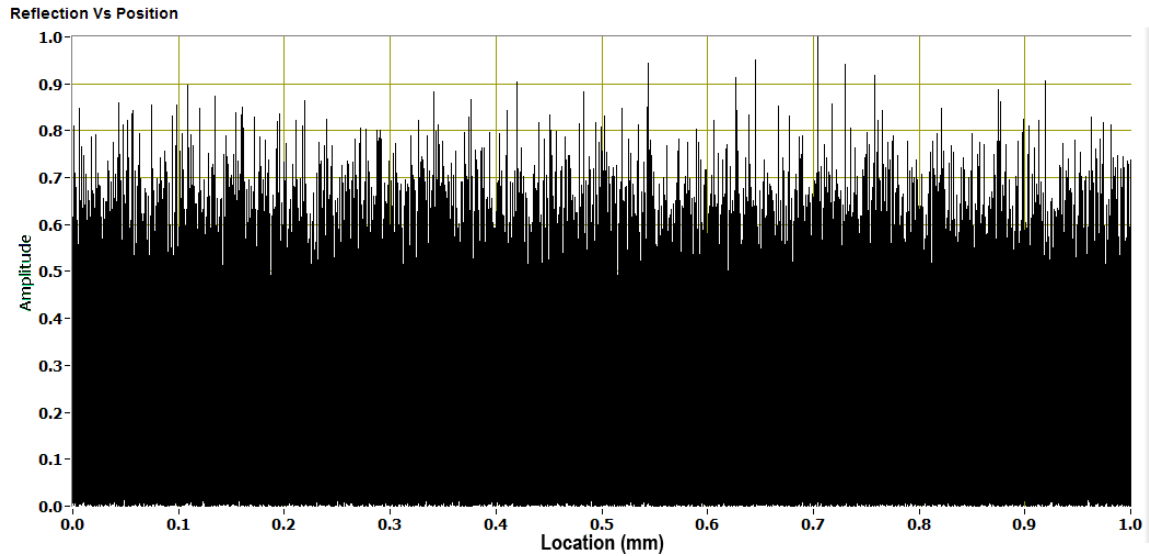


Figure 4-1. An example of Rayleigh scatter reflections at atomic resolution

Due to the finite sweep window afforded by a tuneable laser source, the full spectrum of the measurement cannot be acquired. Instead, a small window of the spectrum defined by the performance specifications of the tuneable device is traversed. This results in the functional equivalent of applying a band-pass filter to the spectral content of the data in Figure 4-1. The spectrum is shown in Figure 4-2.

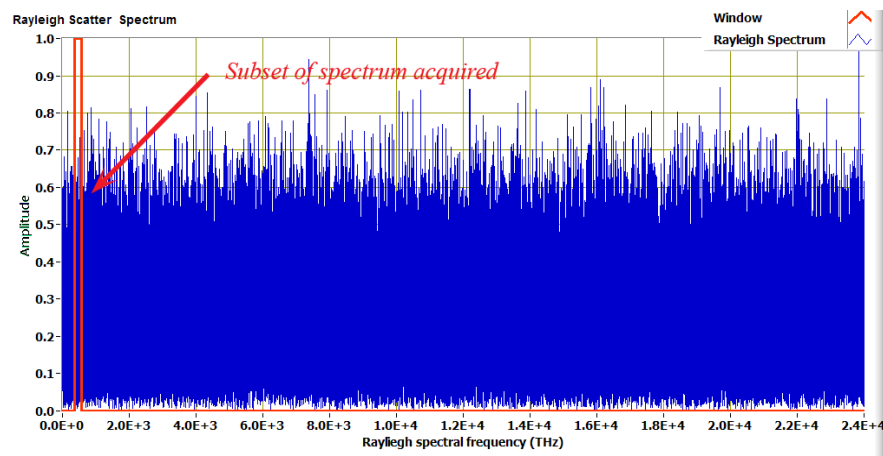


Figure 4-2. An example of Rayleigh scatter measurement spectrum at full atomic resolution and corresponding window representing laser angular frequency sweep range.

The effect of the physical limitation on scan range can be illustrated by representing the region of acquisition as a rectangular window with a value of 1 at the pass band and 0 everywhere else. Applied to the Rayleigh scatter spectrum, the window produces a filtered array of equal length to the original data as illustrated in Figure 4-3 below. Note that the windowed signal amplitude is

lower with increased variation over the subset of data examined. A further examination of a smaller portion of the domain reveals an amplitude modulation of the full Rayleigh spectrum reflection as seen in the figure inset.

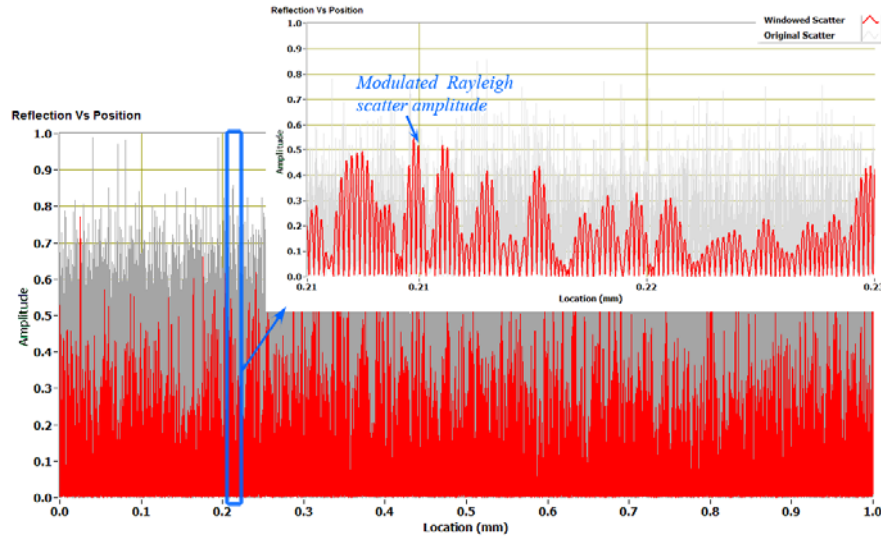


Figure 4-3. An example of Rayleigh scatter measurement spectrum at full atomic resolution and corresponding window representing laser angular frequency sweep range.

Knowing that the laser only traverses a portion of the spectrum, an inverse transform is performed of only the segment traversed by the device. The segment length, or rather, the laser sweep range determines the spatial resolution of the Rayleigh reflection as a function of position. An examination of Figure 4-4 indicates that the segmented array produces a decimated representation of the windowed array.

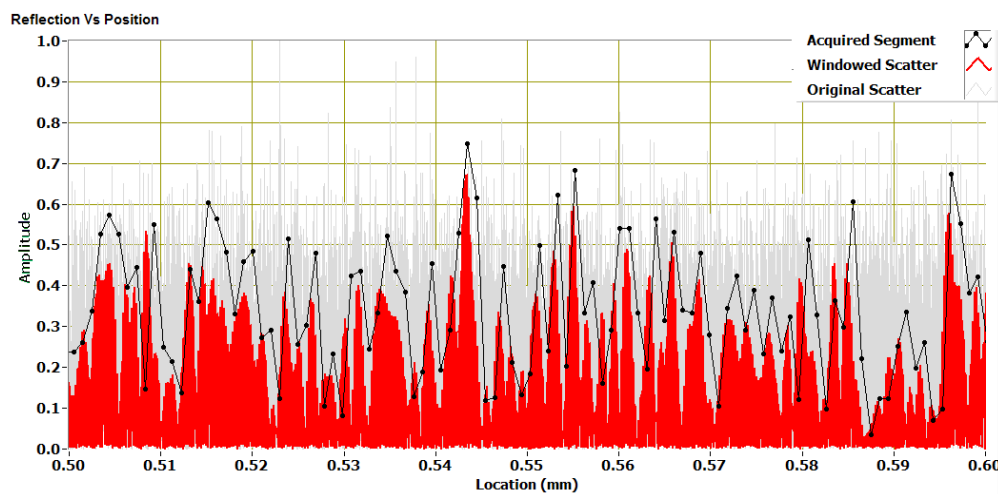


Figure 4-4. Rayleigh scatter reflection versus position for original scatter (grey and in the background), Windowed spectra (red), and segmented array over the laser sweep region (black with points)

The limited spectral bandwidth of the source produces a representative decimated data set of the spectral response of the reflective sites along the fiber, with the spatial resolution being inversely proportional to the spectral width traversed by the laser during acquisition.

Mathematically, the modified Rayleigh scatter distribution can be represented as the product of the full atomic spatial distribution and a phase modulation term, $e^{-i \cdot k_0 x}$ such that:

$$\widehat{\kappa}(x) = E(x) \cdot e^{-i \cdot \phi(x)} \cdot e^{-i \cdot k_0 x} \tag{4-1}$$

where $\widehat{\kappa}(x)$ represents the Rayleigh scatter function, $E(x)$ represents the Rayleigh scatter amplitude as a function of position and k_0 is the propagation number at the center of the pass-band. Equation (4-1) will subsequently be used as the representative Rayleigh distributed reflectivity function.

4.2 The strain function

An analysis of axial strain applied to an axial bar is performed to gain an understanding of how strain would couple into optical fiber, which can be loosely modelled as a 1-dimensional structure. Assume that the application of strain onto a point x_1 will result in a displacement δx .

The new reflection event will occur at a displaced location $x^1 + \sum_{i=0}^1 \varepsilon \cdot \delta x^i$. Similarly, a second point, x_2 adjacent to the first, experiencing the same constant strain profile, will have a total displacement equal to the sum of the displacement of the first point and that of its own local displacement resulting in a new location equal to $x^2 + \sum_{i=0}^2 \varepsilon \cdot \delta x^i$ as illustrated in Figure 4-5.

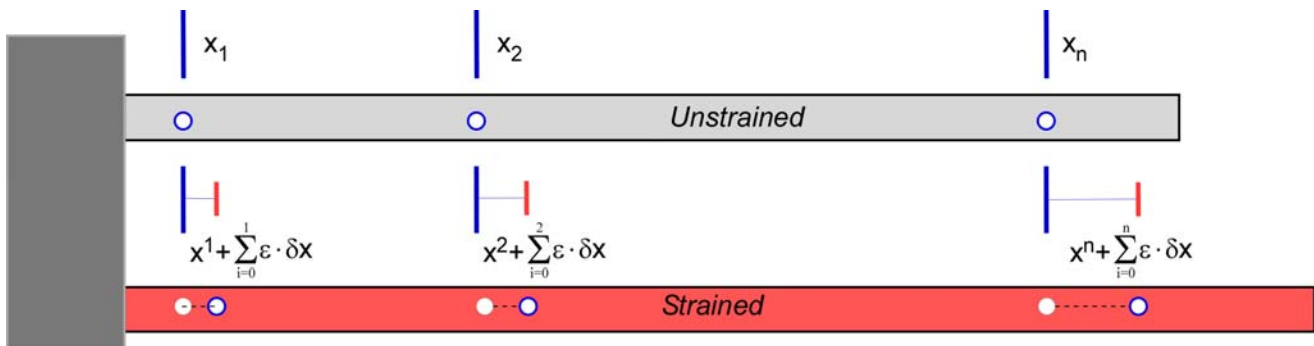


Figure 4-5. Axial strain applied to axial bar

From the above illustration, the strain profile takes the functional form equivalent to:

$$x^n \Big|_{\text{strained}} = x^n + \sum_{i=0}^n \varepsilon \cdot \delta x^i \quad (4-2)$$

Taking the limit of equation (4-2) results in:

$$x \Big|_{\text{strained}} = x + \int_0^x \varepsilon \cdot dx' \quad (4-3)$$

By extending the derivation to an arbitrary strain field it can be shown that:

$$x \Big|_{\text{strained}} = x + \int_0^x \varepsilon(x') \cdot dx' \quad (4-4)$$

Reviewing the above equation, it is recognized that the strained location of any point positioned along a 1 dimensional element is resolved by the sum of its previous location to the accumulated strain displacement to the point.

4.3 Resolving strain in Rayleigh scatter temporal domain

As discussed earlier in section 2.3.2.4.1, Rayleigh backscatter for a given fiber has a random but static scatter amplitude and phase pattern as a function of distance. In order to make any sense of the acquired measurements, deterministic content needs to be reconstructed from these random events. Revisiting the modulated Rayleigh scatter equation, (eqn. (4-1)) and applying it to equation (4-4) to define both the strained and unstrained states, the following is obtained:

$$\widehat{\kappa}(x) = E(x) \cdot e^{-i \cdot \phi(x)} \cdot e^{-i \cdot k_0 \cdot x} \quad (4-5)$$

$$\widehat{\kappa}\left(x + \int \varepsilon(x)\right) = E\left(x + \int \varepsilon(x)\right) \cdot e^{-i \cdot \phi\left(x + \int \varepsilon(x)\right)} \cdot e^{-i \cdot k_0 \cdot \left(x + \int_0^x \varepsilon(x) \cdot dx\right)} \quad (4-6)$$

The strain coupled into the phase of the perturbed state can be resolved by conjugating the perturbed state and multiply it with the reference static measurement resulting in:

$$\widehat{\kappa}(x) \cdot \widehat{\kappa}^*\left(x + \int \varepsilon(x)\right) = E(x) \cdot e^{-i \cdot \phi(x)} \cdot e^{-i \cdot k_0 \cdot x} \cdot \left(E\left(x + \int \varepsilon(x)\right) \cdot e^{-i \cdot \phi\left(x + \int \varepsilon(x)\right)} \cdot e^{-i \cdot k_0 \cdot \left(x + \int_0^x \varepsilon(x) \cdot dx\right)} \right)^* \quad (4-7)$$

$$= E(x) \cdot e^{-i \cdot \phi(x)} \cdot e^{-i \cdot k_0 \cdot x} \cdot E\left(x + \int \varepsilon(x)\right) \cdot e^{i \cdot \phi\left(x + \int \varepsilon(x)\right)} \cdot e^{i \cdot k_0 \cdot \left(x + \int_0^x \varepsilon(x) \cdot dx\right)} \quad (4-8)$$

$$= E(x) \cdot E\left(x + \int \varepsilon(x)\right) \cdot e^{i\left[-\phi(x) - k_0 x + \phi(x + \int \varepsilon(x)) + k_0 \left(x + \int_0^x \varepsilon(x) dx\right)\right]} \quad (4-9)$$

$$= E(x) \cdot E\left(x + \int \varepsilon(x)\right) \cdot e^{i\left(-\phi(x) - k_0 x + \phi(x + \int \varepsilon(x)) + k_0 x + k_0 \int_0^x \varepsilon(x) dx\right)} \quad (4-10)$$

$$= E(x) \cdot E\left(x + \int \varepsilon(x)\right) \cdot e^{i\left(\phi(x + \int \varepsilon(x)) - \phi(x) + k_0 \int_0^x \varepsilon(x) dx\right)} \quad (4-11)$$

At this point, assume that the strain perturbation function is sufficiently small relative to the variable x such that:

$$x + \int \varepsilon(x) \approx x \quad (4-12)$$

The implication of the assumption above is that the sampling resolution at data acquisition has to be coarser than the accumulated positional shift at the point of interest. That is:

$$\Delta x \gg \int_0^x \varepsilon(x) \cdot dx \quad (4-13)$$

where Δx is the sampling resolution and x is the position of interest. Now, applying equation (4-12) to eqn. (4-11), results in:

$$\widehat{\kappa}(x) \cdot \widehat{\kappa}^*\left(x + \int \varepsilon(x)\right) = E(x) \cdot E(x) \cdot e^{i\left(\phi(x) - \phi(x) + k_0 \int_0^x \varepsilon(x) dx\right)} \quad (4-14)$$

$$= E^2(x) \cdot e^{i \cdot k_0 \int_0^x \varepsilon(x) dx} \quad (4-15)$$

Equation (4-15), shows that the complex correlation yields a phase term that is the product of the pass-band center propagation number k_0 and the accumulated strain to the point of interest. Of primary interest here is the unknown strain function. The function can be recovered by simply taking the derivative of the measured phase resulting in:

$$\frac{d\phi}{dx} = \frac{d}{dx} \left[k_0 \int_0^x \varepsilon(x) \cdot dx \right] \quad (4-16)$$

$$= k_0 \cdot \varepsilon(x) \quad (4-17)$$

It is clear that the phase derivative results in the local strain function scaled by the propagation number. The phase derivative is thus linearly proportional to the strain function.

4.4 Resolving strain in Rayleigh scatter spectrum

4.4.1 Constant strain approximation

An alternative method is to perform a similar investigation in the spectrum of the acquired signal. The analysis begins by revisiting (3-49) and the backscatter expressions for the strain-free and the strained states as stated in eqns. (4-5) and (4-6). For the strain free state, it can be shown that:

$$\underbrace{E^-(0, \omega)}_{E_0^-} \Big|_{\Delta \varepsilon = 0} = \int_0^L E_2 e^{i(\omega t - k \cdot x)} \cdot E_1(x) \cdot e^{-i\phi(x)} \cdot e^{-i k_0 x} \cdot dx \quad (4-18)$$

$$= \int_0^L E_2 \cdot E_1(x) \cdot e^{i(\omega t - k \cdot x - \phi(x) - k_0 x)} \cdot dx \quad (4-19)$$

Repeating the above to get the function for the strained state results in:

$$\underbrace{E^-(x, \omega)}_{E_{\int \varepsilon(x) dx}^-} \Big|_{\Delta \varepsilon = \int \varepsilon(x) dx} = \int_0^L E_2 \cdot e^{i(\omega t - k \cdot x)} \cdot E_1 \left(x + \int_0^x \varepsilon(x') dx' \right) e^{-i\phi(x + \int \varepsilon(x) dx)} \cdot e^{-i k_0 \left(x + \int_0^x \varepsilon(x') dx' \right)} dx \quad (4-20)$$

$$= \int_0^L E_2 \cdot E_1 \left(x + \int_0^x \varepsilon(x') dx' \right) e^{i \left(\omega t - k \cdot x - \phi(x + \int \varepsilon(x) dx) - k_0 \left(x + \int_0^x \varepsilon(x') dx' \right) \right)} dx \quad (4-21)$$

If the segment is sufficiently small, the strain field across the segment can be approximated as a constant. The phase term due to strain, $k_0 \int_0^x \varepsilon(x') dx'$ then becomes:

$$\phi(x) \Big|_{\Delta \varepsilon} = k_0 \int_0^x C \cdot dx \quad (4-22)$$

$$= k_0 \cdot C \cdot x \quad (4-23)$$

where C is the strain constant. Modifying equation (4-21):

$$E_{\int \varepsilon(x) dx}^- = \int_0^L E_2 \cdot E_1(x + Cx) e^{i(\omega t - k \cdot x - \phi(x + Cx) - k_0(x + Cx))} dx \quad (4-24)$$

The strain change is then postulated to be sufficiently small such that the perturbed amplitude and phase terms are approximately equal to the unperturbed states.

$$E(x) \approx E(x + Cx) \quad (4-25)$$

$$\phi(x) \approx \phi(x + Cx) \quad (4-26)$$

Applying equations (4-25) and eqns. (4-26) to equation (4-24):

$$E_{f\varepsilon(x)dx}^- = \int_0^L E_2 \cdot E_1(x) \cdot e^{i(\omega t - k \cdot x - \phi(x) - k_0(x+Cx))} dx \quad (4-27)$$

To determine the strain field, the variation between eqns. (4-21) and (4-27) needs to be compared. This is achieved by performing a cross correlation, defined as:

$$f * g = \Im[\overline{E_{f\varepsilon(x)dx}^-}(\tau) \cdot E_0^-(\tau)] \quad (4-28)$$

where f and g are both functions of angular frequency. \Im denotes the Fourier transform and \overline{E} denotes the complex conjugate. The Fourier transform results in:

$$\Im[E_{f\varepsilon(x)dx}^- \cdot E_0^-(\tau)] = 2\pi \int_0^L E_2 \cdot E_1(x) \cdot e^{-i(\omega t - k \cdot x - \phi(x) - k_0 x)} \cdot E_2 \cdot E_1(x) \cdot e^{i(\omega t - k \cdot x - \phi(x) - k_0(x+Cx))} e^{i \frac{\omega}{k} \tau} dx \quad (4-29)$$

The limits are extend to $[-\infty, \infty]$, by noting that the amplitude function is zero everywhere except between $[0, L]$.

$$\Im[E_{f\varepsilon(x)dx}^- \cdot E_0^-(\tau)] = 2\pi \cdot E_2^2 \int_{-\infty}^{\infty} E_1^2(x) \cdot e^{i(-\omega t + k \cdot x + \phi(x) + k_0 x + \omega t - k \cdot x - \phi(x) - k_0 x - k_0 Cx + 2n_{eff} kx)} dx \quad (4-30)$$

$$= 2\pi \cdot E_2^2 \int_{-\infty}^{\infty} E_1^2(x) \cdot e^{i(2n_{eff} kx - k_0 Cx)} dx \quad (4-31)$$

$$= 2\pi \cdot E_2^2 \int_{-\infty}^{\infty} E_1^2(x) \cdot e^{i \cdot x(2n_{eff} k - k_0 C)} dx \quad (4-32)$$

$$= 2\pi \cdot E_2^2 \cdot E_1^2 \cdot \frac{1}{2\pi} \delta(2n_{eff} k - k_0 C) \quad (4-33)$$

$$= E_1^2 \cdot E_2^2 \cdot \delta(2n_{eff} k - k_0 C) \quad (4-34)$$

The expression in equation (4-34), shows that a variation in strain results in a shift in the Rayleigh spectrum equivalent to the magnitude of the strain, scaled by the propagation number k_0 .

4.5 Summary

To this point, it has been demonstrated how one could acquire distributed temperature or strain from Rayleigh scatter by forming deterministic content from the random but static arrays through a cross-correlation between a reference and subsequent a measurement acquisitions. The mathematical operation yields a differential phase term that can be used to determine temperature or strain using either a temporal or spectral algorithms. The following chapter will

collate and computer simulations and laboratory experiments to support the theoretical work documented thus far.

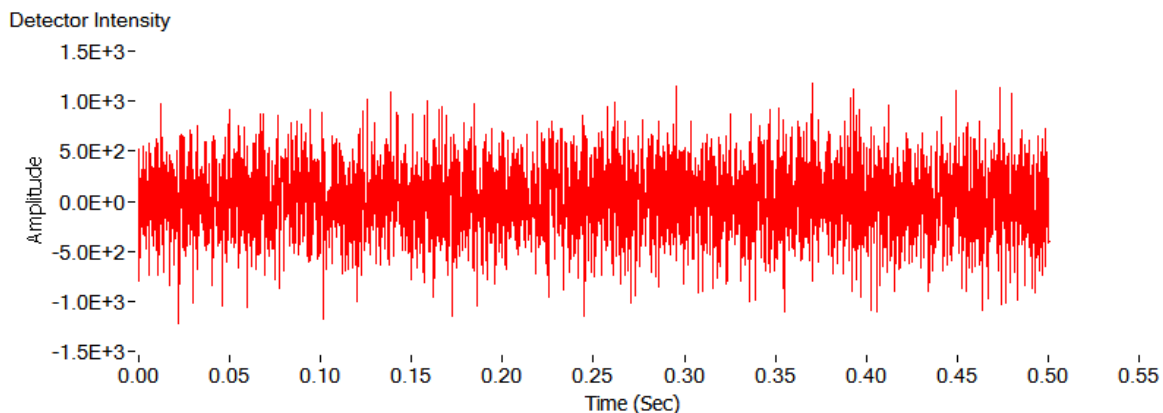
5 Static Strain Simulations and Experiments

This chapter contains computer simulations and experiments performed in support of the theoretical static strain analysis. The simulations begin with the acquiring strain in the temporal and spectral domain as discussed in sections 4.3 and 4.4. The chapter then presents new content developed by the author in improving the accuracy and fidelity of measurements obtained in the spectral domain. The section acts as a demarcation from what knowledge is from the public domain (such as papers and text books) and what is the author's contribution in advancing the knowledge in distributed sensing.

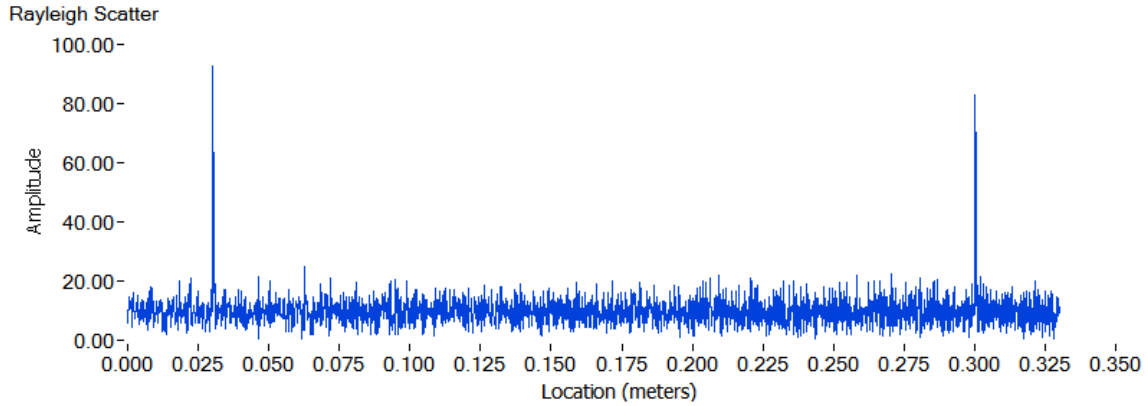
5.1 Phase Derivative Computer Simulation

A computer simulation model was used to generate Rayleigh scatter in an unstrained state based on equation (3-73) using the procedure discussed in Section 3.2.2. The strained scatter was generated using the same amplitude vector. However the position vector x'' was modified to account for strain based on equation (4-2).

Figure 5-1 and 2 show the Rayleigh scatter and detector intensity generated for the baseline and perturbed states. A 33 cm fiber with a 160 micron two point spatial resolution with reflective events at 3 cm and 30 cm was modeled corresponding to a laser sweep rate of 10nm/sec, a range of 5nm and a center wavelength of 1550 nm.

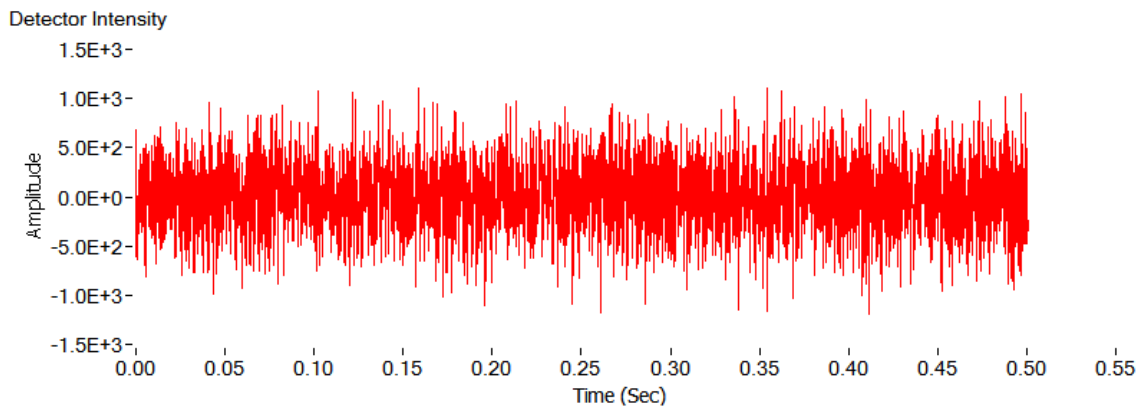


a) detector intensity

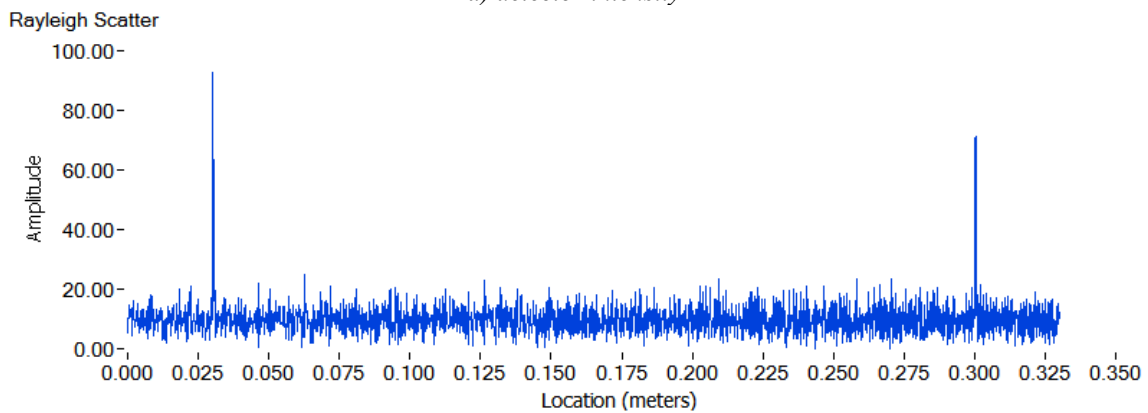


b) Rayleigh scatter

Figure 5-1. The Rayleigh scatter and detector intensity of unstrained fiber generated using a computer simulation model



a) detector intensity



b) Rayleigh scatter

Figure 5-2. The Rayleigh scatter and detector intensity of strained fiber generated using a computer simulation model

Figure 5-3 is an example of phase and phase derivative results from the fiber simulation model.

The data represents the phase term $k_0 \int_0^x \varepsilon(x) \cdot dx$ and the phase derivative $\varepsilon(x)$, which

corresponds to the input strain field.

As expected, the phase term yields an accumulation of the forward displacement due to strain to the point of interest as seen in Figure 5-3a. Figure 5-3b shows the phase derivative.

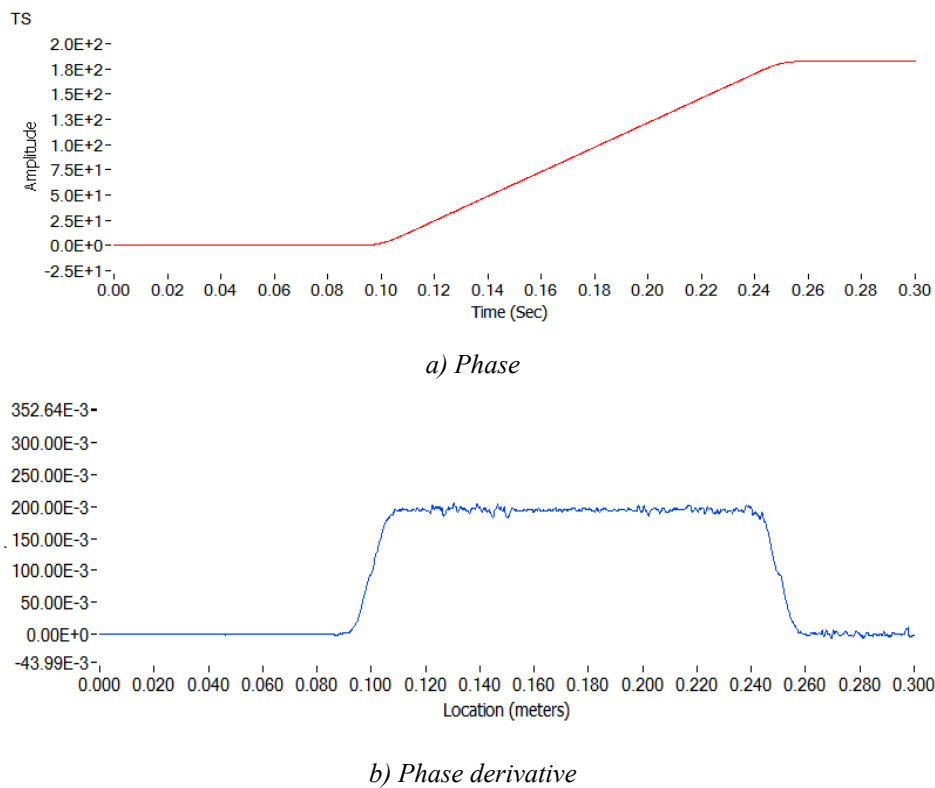


Figure 5-3 The phase and phase derivative for a constant strain field over a subset of the domain of the computer simulated dataset

5.2 Phase Derivative of Acquired Data

Figure 5-4 shows the phase and phase derivative computed from Rayleigh scatter acquired using the Optical Backscatter Reflectometer (OBR). A constant strain field was precisely induced by mounting a translation stage with a micrometer drive on a rail and clamping the communications grade single mode fiber onto the stage and on a distant point on the rail. Fusion splice protectors were used to grip the fiber; the splice protectors were clamped down to the linear stage and rail which had a total gage length of 0.31 meters. Using the translation stage, the fiber segment was elongated by 3, 5 and 8 microns inducing a step change in strain. The OBR traversed a 5nm wavelength range centred at 1550 nm. As expected, the strain field is a step function over the region of induced strain.

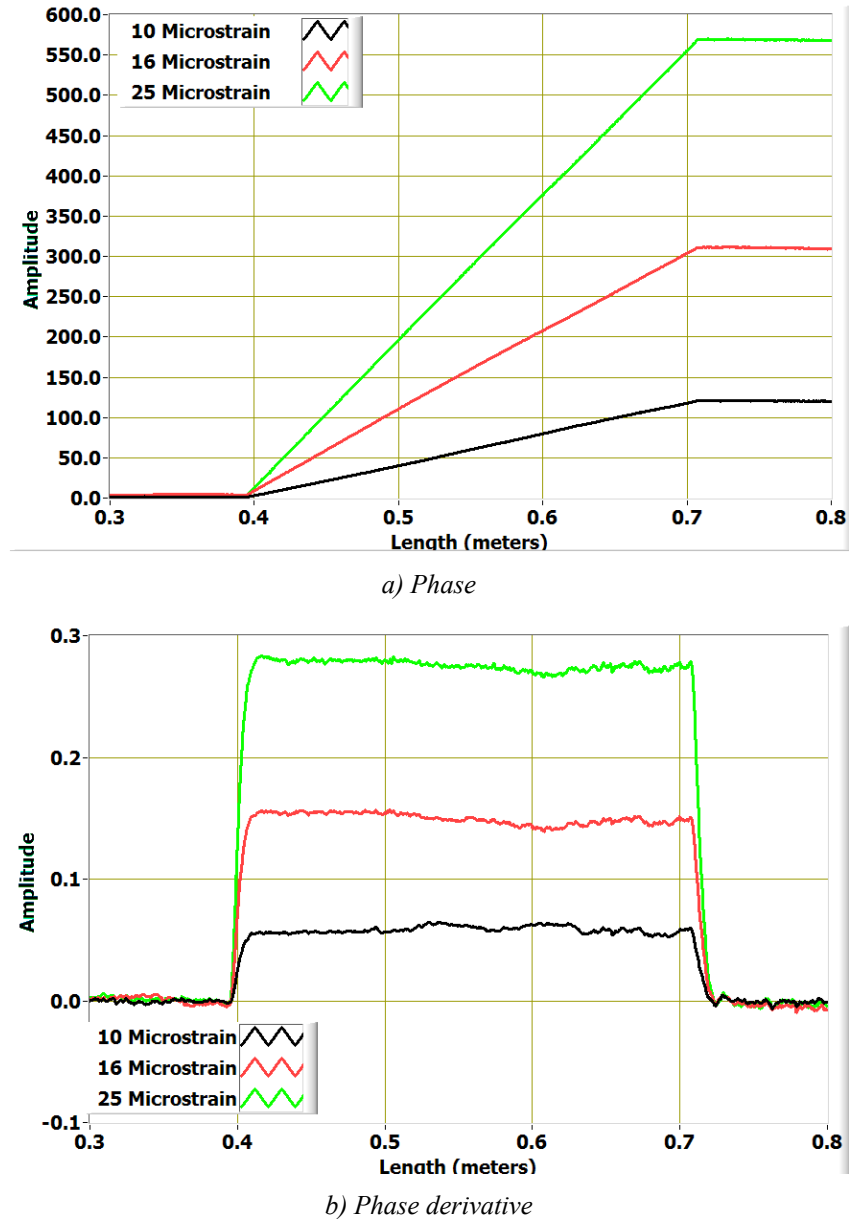


Figure 5-4 The phase and phase derivative for a constant strain field over a 0.31 Meter section of single mode fiber from experimental data acquired using the Optical Backscatter Reflectometer

5.3 Constant Strain Computer Simulation

Figure 5-5 shows the strain profile computed using a constant strain approximation in the Rayleigh scatter spectrum. The data set discussed in section 1.1 was used in this simulation. The spectral shift between the reference and perturbed states was computed for each segment sequentially across the domain and compiled thus forming the strain response as seen in Figure 5-5a. The segment width and spacing was 5mm and 2 mm respectively. Figure 5-5 b shows the strain (which is a function of the spectral shift) seen at A and B as indicated in a. c shows the

temporal shift of the measurement, which correlates to the elongation of the fiber as a function of position. Notice the similarity in shape and form to the phase function illustrated in Section 4.3.

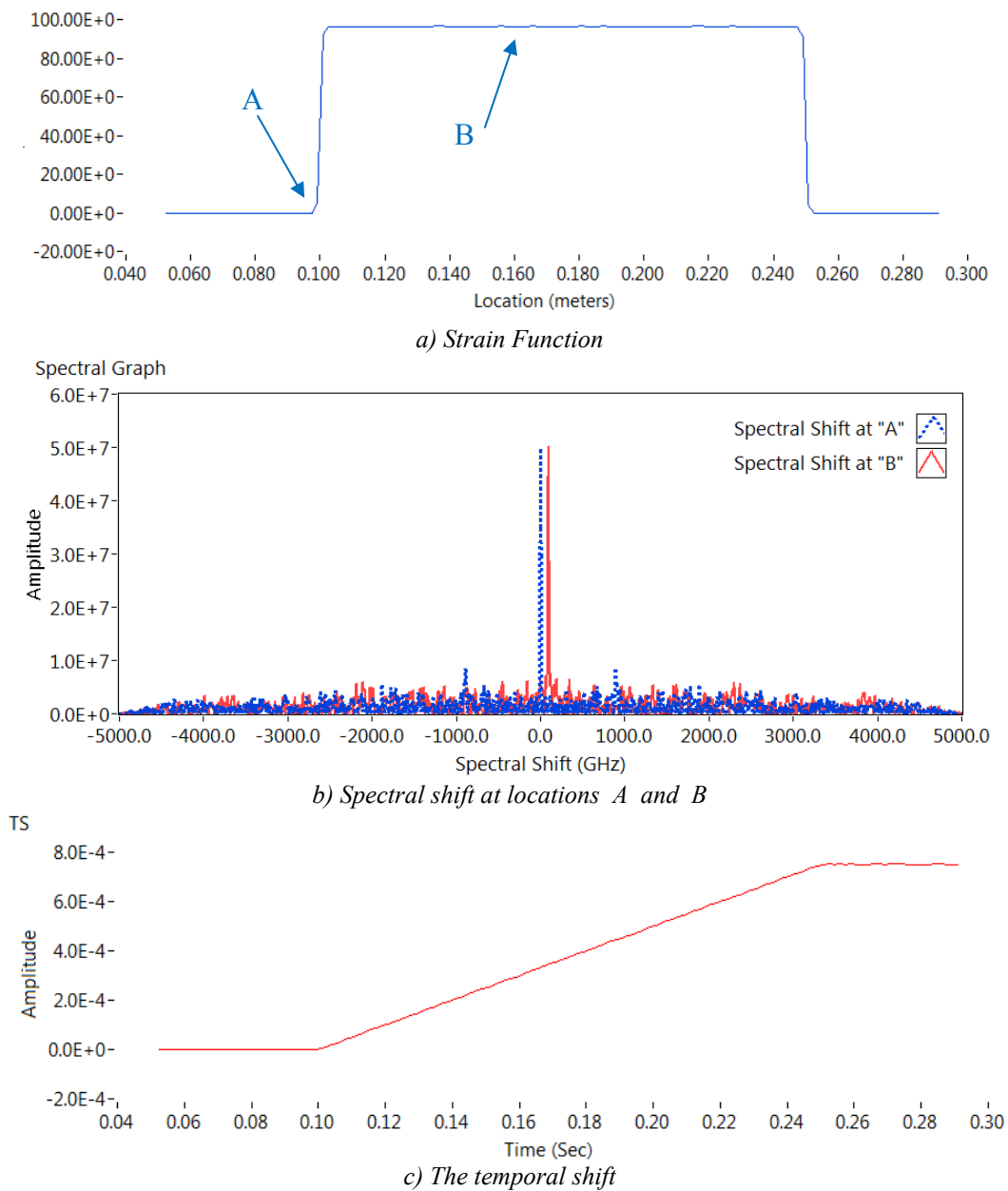
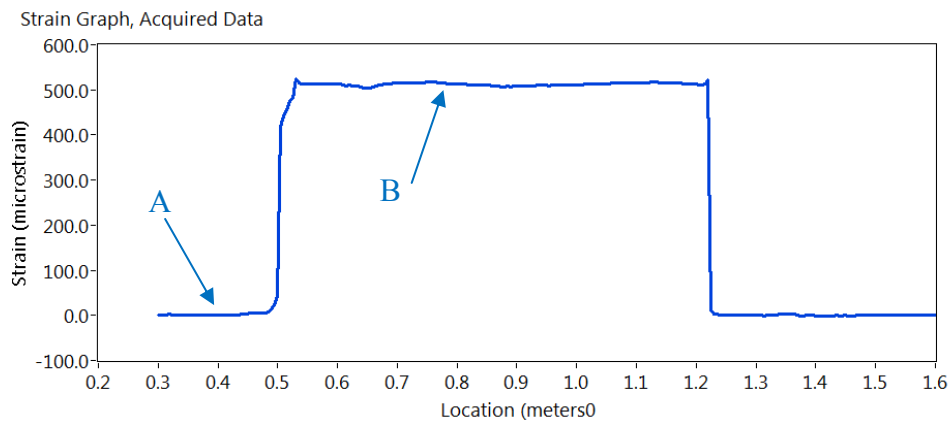


Figure 5-5. The strain function computed from the computer simulated Rayleigh scatter spectrum.

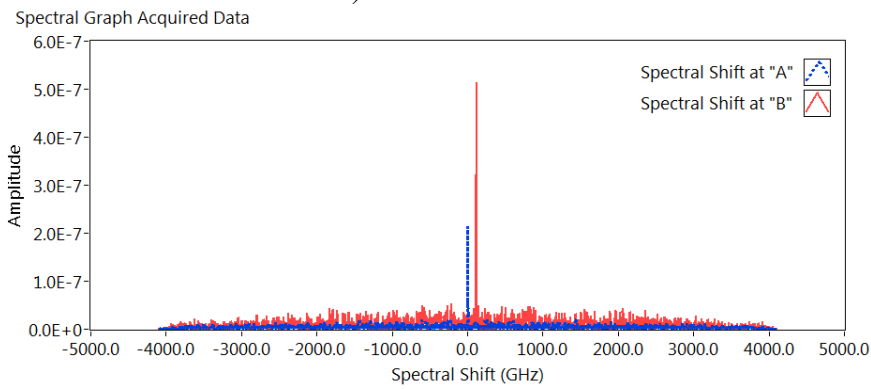
5.4 Constant Strain Experimental Data

Figure 5-6 shows the results computed from Rayleigh scatter acquired using the Optical Backscatter Reflectometer (OBR). A constant strain field was induced by using a 0.7 m translation stage. Using the attached micrometer drive, the fiber segment was elongated by 500 $\mu\epsilon$. The OBR was configured to traverse a 20nm wavelength range centred at 1550 nm. A

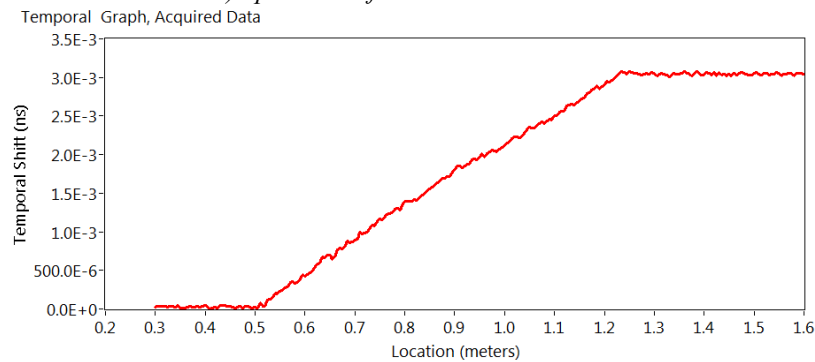
segment width and spacing of 1cm and 0.5 cm respectively was used to compute the strain along the fiber. Figure 5-6a shows the strain results; as expected, the strain field is a step function over the region of induced strain. Figure 5-6 b shows the corresponding spectral shift computed at locations A and B as indicated in Figure 5-6 a. Figure 5-6c shows the temporal shift as a function of position.



a) Strain Function



b) Spectral shift at locations A and B



c) The temporal shift

Figure 5-6. The strain function computed from the experimentally acquired Rayleigh scatter spectrum.

5.5 Linear Strain Approximation

There are instances where a constant strain approximation is not sufficient to accurately compute the spectral shift in a segment. This is particularly true in instances of distributed high temperature measurements, where a zone of a high thermal gradient exists between the low and high temperature region as illustrated in Figure 5-7.

Here, gold-coated single-mode fiber was used during the thermal testing between 25 - 850°C⁸⁰. The test setup is illustrated in Figure 5-8. An optical fiber was passed through a 17 Mellen box furnace and was sheathed in a Ø0.080 thin-walled stainless steel capillary tube. This was then inserted into a Ø0.25 x 24 medium pressure stainless steel tube for structural support. The outer tube minimized thermal fluctuations in the heated zone. The fiber temperature was also monitored using a type K thermocouple inserted within the outer tube, adjacent to the stainless steel capillary at the furnace center. The data was acquired at a 20µm 2-point spatial resolution. A 1cm segment width was used to compute the spectral shift over a 1 meter domain.

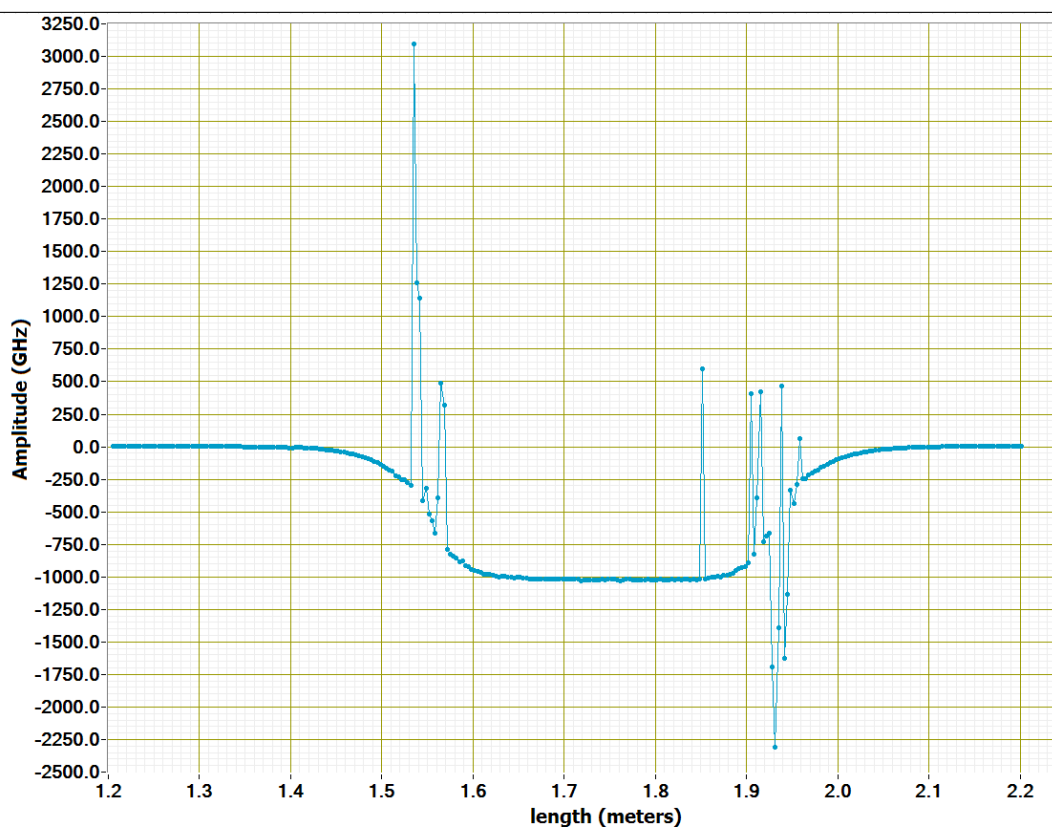
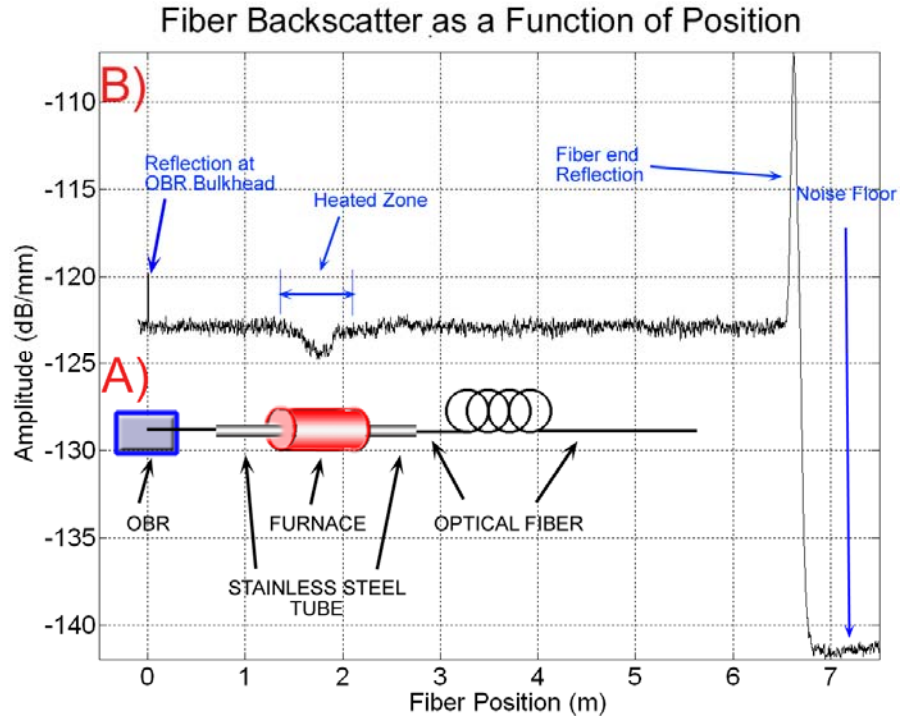


Figure 5-7. Experimental data of Spectral shift versus position in a high temperature test



b) High temperature test setup also showing Rayleigh scatter trace of fiber
Figure 5-8. Experimental test setup, also showing the Rayleigh scatter trace of the fiber

Notice the spurious data at the shoulders in a due to aggressive change in temperature as the fiber enters and exits the furnace. To increase the signal to noise ratio at the region of high strain gradient, the approximation of the strain field across the segment is assumed to be a linear function rather than a being a constant across the segment. Reformulating the phase term due to strain,

$$k_0 \int_0^x \varepsilon(x') dx' :$$

$$\phi(x)_{\Delta \varepsilon} = k_0 \int_0^x m \cdot x' \cdot dx' \tag{5-1}$$

$$= k_0 \cdot m \cdot \frac{x^2}{2} \tag{5-2}$$

where m is the strain slope. Modifying equation (4-21) using the expression from (4-25), (4-26) and results in:

$$E_{\int \varepsilon(x) \cdot dx}^- = \int_0^L E_2 \cdot E_1(x) \cdot e^{i \left(\omega t - k \cdot x - \phi(x) - k_0 \left(x + k_0 m \frac{x^2}{2} \right) \right)} dx \tag{5-3}$$

The expression for the strain field is then determined based on equation (4-28).

$$\Im[E_{f_{\varepsilon(x)}^-}(\tau) \cdot E_0^-(\tau)] = 2\pi \int_{-\infty}^{\infty} \left[E_2 \cdot E_1(x) \cdot e^{-i(\omega t - k \cdot x - \phi(x) - k_0 x)} \cdot E_2 \cdot E_1(x) \cdot e^{i(\omega t - k \cdot x - \phi(x) - k_0(x + k_0 m \frac{x^2}{2}))} e^{i 2n_{eff} k} \right] \cdot dx \quad (5-4)$$

$$= 2\pi \cdot E_2^2 \int_{-\infty}^{\infty} \left[E_1^2(x) \cdot e^{i(-\omega t + k \cdot x + \phi(x) + k_0 x + \omega t - k \cdot x - \phi(x) - k_0 x - k_0 m \frac{x^2}{2} + 2n_{eff} k x)} \right] \cdot dx \quad (5-5)$$

$$= 2\pi \cdot E_2^2 \int_{-\infty}^{\infty} \left[E_1^2(x) \cdot e^{i(2n_{eff} k x - k_0 m \frac{x^2}{2})} \right] \cdot dx \quad (5-6)$$

$$= 2\pi \cdot E_2^2 \int_{-\infty}^{\infty} \left[E_1^2(x) \cdot e^{i x (2n_{eff} k - k_0 m \frac{x}{2})} \right] \cdot dx \quad (5-7)$$

$$= 2\pi \cdot E_2^2 \cdot E_1^2 \cdot \frac{1}{2\pi} \delta(2n_{eff} k - k_0 C) \quad (5-8)$$

$$= E_1^2 \cdot E_2^2 \cdot \delta\left(2n_{eff} k - k_0 m \frac{x}{2}\right) \quad (5-9)$$

Again, the spectral shift is proportional to the linear strain field scaled by k_0 .

Figure 5-9 shows the spectral shift computation based on the same raw dataset illustrated in Figure 5-7. The data was processed using a slope correction algorithm implementing a linear strain approximation over the computation segment as described above. A 1 cm segment width was used.

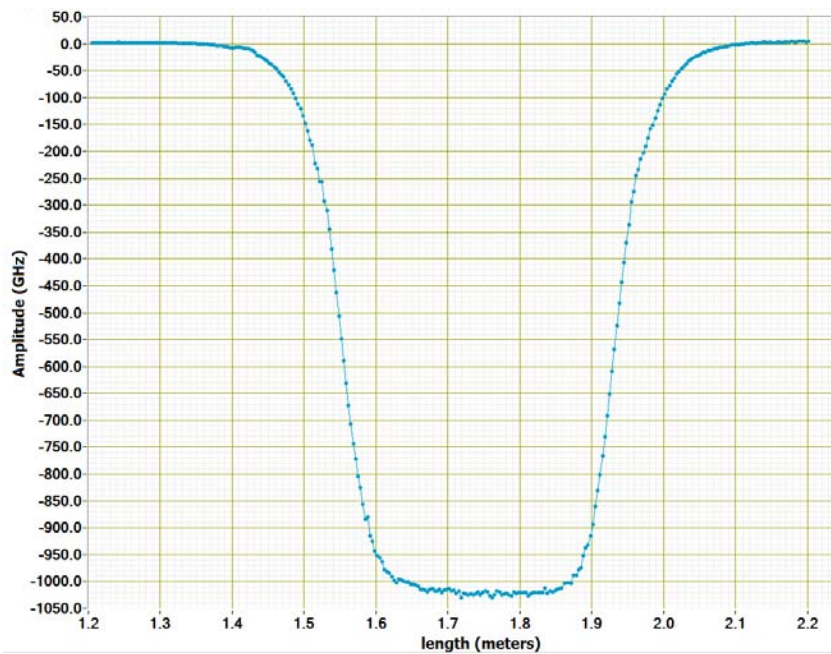


Figure 5-9 Spectral shift computed using an algorithm that implemented a linear slope estimate over the high gradient region

Notice that all the outliers in the transition zone between low and high temperature that was evident in a have been eliminated. Further information on this experiment is reported in Reference 80 that is included in Appendix C: Supporting Works by the Author. The section includes works that cite experiments with increased levels of complexity relative to the examples modeled in this document.

5.6 Summary

This chapter has shown computer simulation and experimental data that validates the theoretical derivations done in Chapter 4. The computer simulations and experiments demonstrated distributed strain or temperature measurements using a temporal or spectral technique by processing the Rayleigh scatter of a reference and a perturbed state. A new method of making parameter measurements in regions of aggressive spatial gradients (such as the temperature profile ingressing or egressing a furnace) using the spectral technique that previously yielded spurious content. The spectral correlation technique will form the basis of the dynamic strain analysis to be covered in Chapter 6.

6 Dynamic Strain Theory

In this chapter, a description on the measurement of dynamic strain (vibration) will be presented to the reader. The document will illustrate how dynamic strain couples into Rayleigh backscatter, thus forming a basis of how one could de-couple the exciting mechanism. The effort will begin by investigating a basic single point interferometer, extending to a distributed measurement and finally illustrating the concept of a distributed vibration decoupling algorithm. The analysis will build upon theory developed during the static strain analysis. All work performed herein presumes that transverse vibration loads couple into the fiber causing axial displacement. This can be presumed true for most cases because of the scale difference of the fiber cross-section relative to the vibrating member cross-section.

6.1 Understanding the basics of Vibration coupling into OFDR measurement

To better understand vibration effects on a fiber, the vibration free, single point development in section 3.1.2 will be revisited. The investigation begins by reviewing the Michelson interferometer, where the mirror in the measurement arm is experiencing a vibration that is causing a small displacement of $\pm\epsilon$ as illustrated in Figure 6-1.

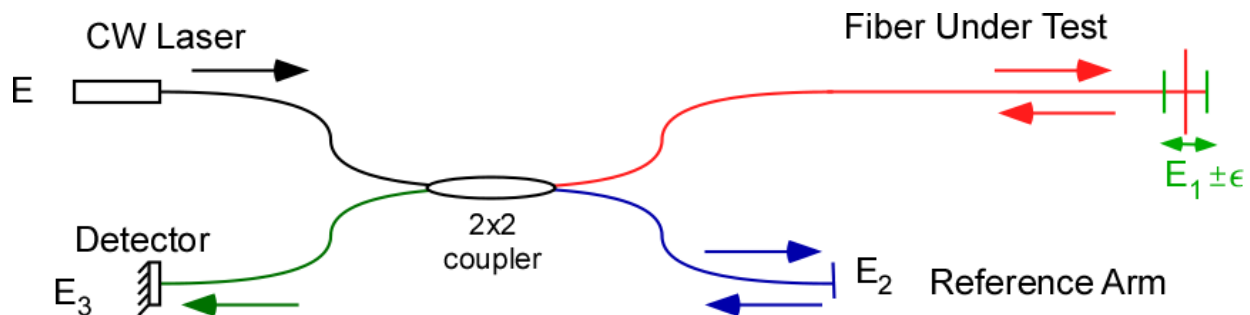


Figure 6-1. A Michelson Interferometer in optical fiber with a vibrating mirror on the measurement arm

Without the vibration effect, it was shown that the field intensity as seen by the optical detector was:

$$I_3(t) = I_1 + I_2 + 2 \cdot \sqrt{I_1 \cdot I_2} \cdot \text{Cos} \left(\alpha \cdot \underbrace{\Delta\tau}_{\frac{n_{eff} \cdot \Delta x}{c}} \cdot t + \theta \right) \quad (3-42)$$

Inspecting equation (3-42), it is evident that the optical energy as seen by the detector has a constant contribution from the reference and measurement arms of the interferometer, and it also

has a time-dependent component that varies as the function of the cosine of the product of the wavelength and the optical path length difference. With the reference arm oscillating, equation (3-42) can be reformulated to be:

$$I_3(t) = I_1 + I_2 + 2 \cdot \sqrt{I_1 \cdot I_2} \cdot \text{Cos} \left(\alpha \cdot \frac{n_{eff}}{c} \cdot \overbrace{\Delta x(t)}^{x(t)} \cdot t + \theta \right) \quad (6-1)$$

where the optical path length difference x is now a function of time. To illustrate how the point vibration couples into the signal, assume $x(t)$ is a small, periodic function in the form of:

$$x(t) = x + A_{vib} \cdot \text{Cos}(\omega_{vib} \cdot t) \quad (6-2)$$

where A_{vib} and ω_{vib} is the amplitude and frequency of vibration. To further simplify the formulation, assume that the amplitude scaling $2 \cdot \sqrt{I_1 \cdot I_2} = 1$ and neglect the DC terms, I_1 and I_2 . Also neglecting the phase term $k_0 \cdot x(t)$, equation (6-1) becomes:

$$I_3(t) = \text{Cos} \left(\underbrace{k_0 \cdot x(t)}_{\text{neglect}} + \frac{2 \cdot n_{eff}}{c} \cdot x(t) \cdot (\alpha \cdot t + \omega_0) \right) \quad (6-3)$$

$$= \text{Cos} \left(\frac{2 \cdot n_{eff}}{c} \cdot x(t) \cdot (\alpha \cdot t + \omega_0) \right) \quad (6-4)$$

$$= \text{Cos} \left(\frac{2 \cdot n_{eff}}{c} \cdot (x + A_{vib} \cdot \text{Cos}(\omega_{vib} \cdot t)) \cdot (\alpha \cdot t + \omega_0) \right) \quad (6-5)$$

Figure 6-2 is an illustration of a vibration signal modulating a reflection at 0.5m down a fiber. The modeling parameters used were, a scan rate 10nm/sec, starting wavelength $\lambda_{start} = 1540 \cdot nm$, wavelength range $\Delta\lambda = 20 \cdot nm$ and a system spatial range of 10 meters. See Appendix B for equation development relating parameters in equation (6-5) to the indicated values above.

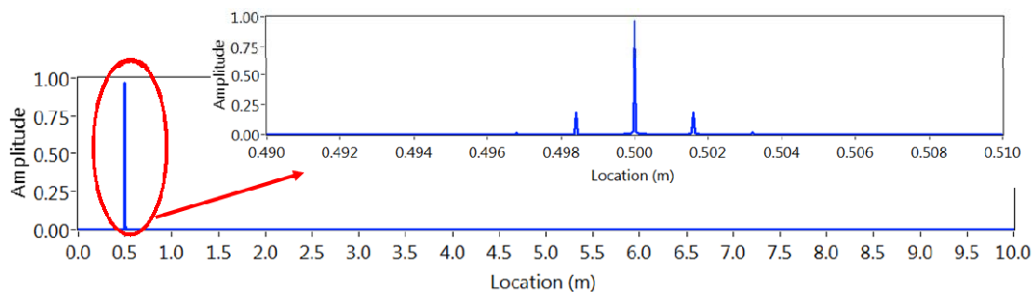


Figure 6-2. A single point on a fiber vibrating to a 20Hz signal Inset shows a close-up of the peak

6.1.1 Frequency variation effects

To investigate amplitude effects, vibration frequencies of 20Hz, 40Hz and 60Hz all at displacement amplitude of $30 \times 10^{-9} \text{m}$ were modeled. Figure 6-3 shows the intensity and Rayleigh scatter response of the signal. Examining the figure, it is evident that the symmetric side lobes mirrored around the modeled point reflection progressively move away from the center reflection with increasing vibration frequency. It is also clear that the amplitude of the side lobe peak amplitude remains constant with varying vibration frequency.

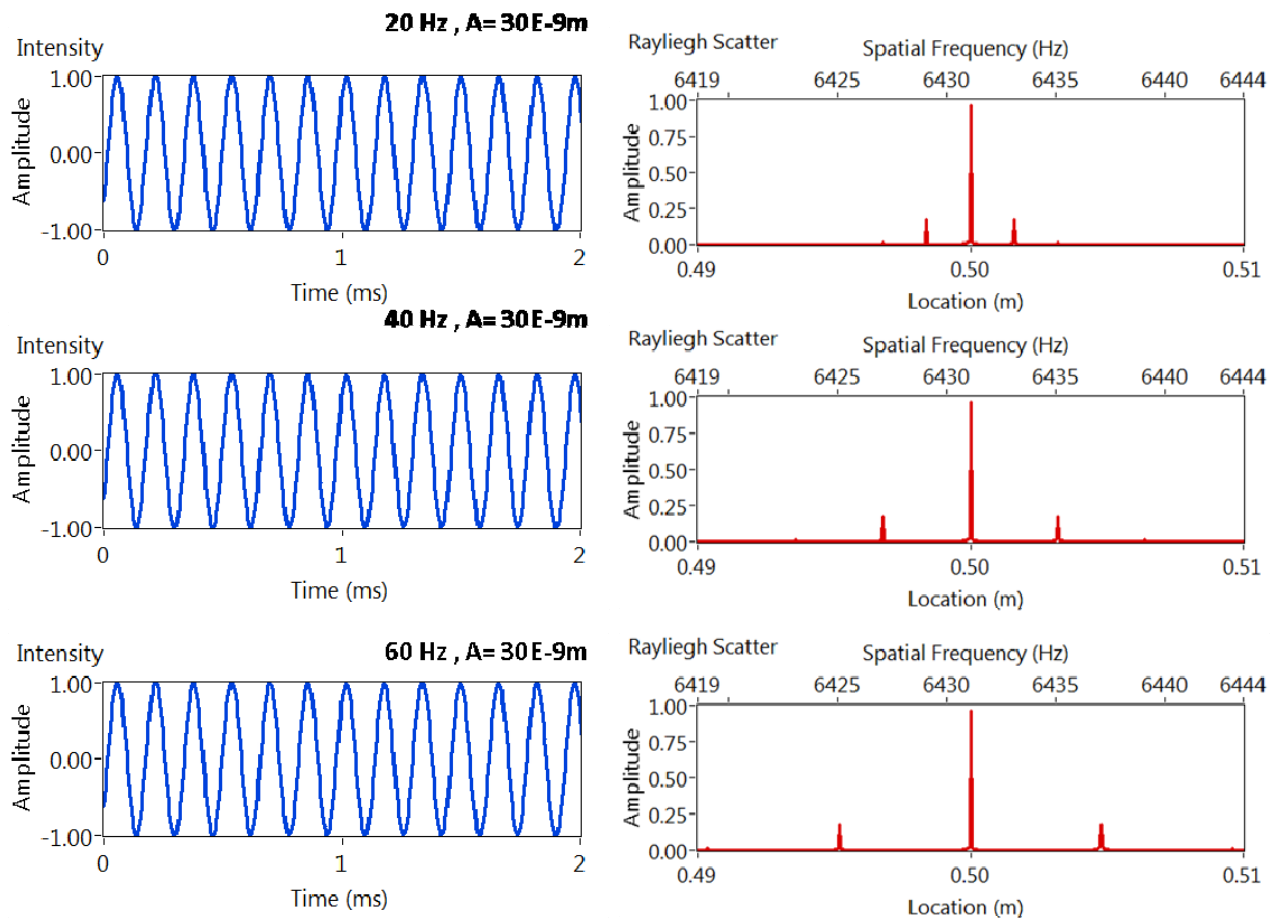


Figure 6-3. Detector intensity and modeled Rayleigh Scatter of a single point

6.1.2 Amplitude variation effects

Figure 6-4 depicts the effects of the vibration amplitude for a 20Hz vibration frequency. As the input energy is increased, not only does the side lobe amplitude increase, but the emergence of secondary side lobes that correspond to higher-order resonant frequencies is observed.

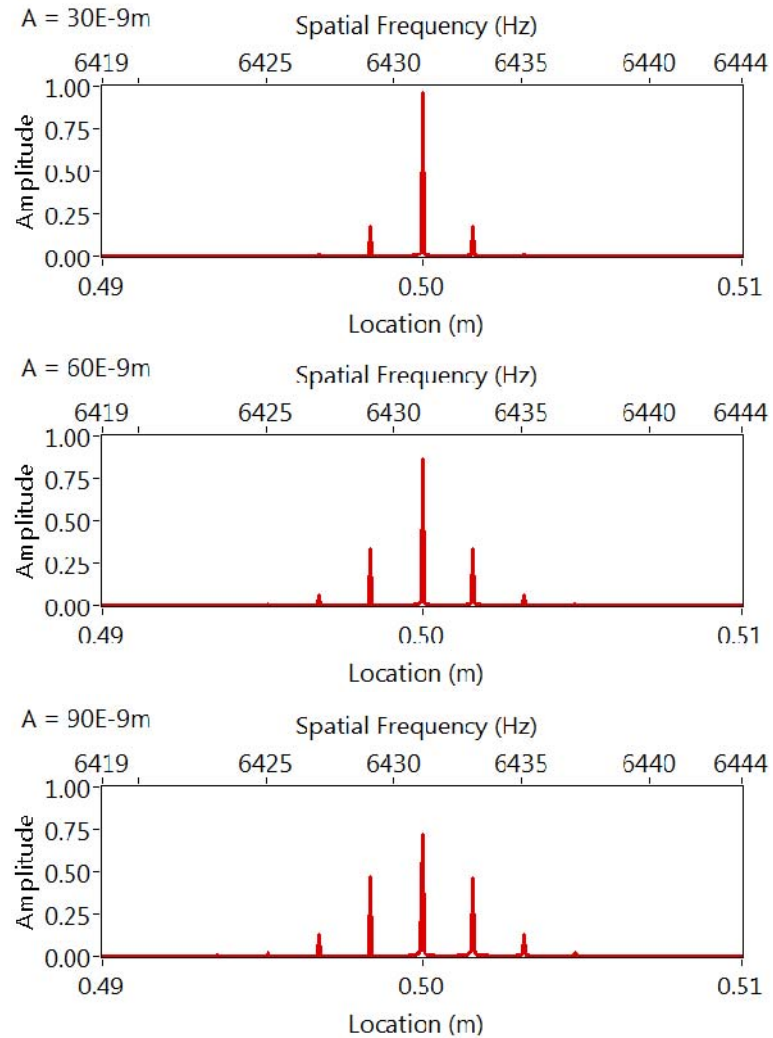


Figure 6-4. Effects of a 20Hz vibration signal with increasing amplitude.

From the simulation above, it can be concluded that in general, vibration has a smearing effect on Rayleigh scatter. The smearing length is proportional to the amplitude and frequency of the vibration signal. It is also clear that vibration leads to the degradation of the amplitude of the modeled point with the decay proportional to the amplitude of vibration.

6.1.3 Baseband shift of amplitude signal

To this point, it is clear that the side-lobe's offset and amplitude relative to the modeled optical path length (OPL) correlate to the exciting frequency. To extract further information, one can take advantage of the fact that OPL is also a function of frequency and shift it to the baseband such that the simulated point (in this case, where $\Delta x = 0.5\text{m}$) is at 0 frequency as shown in

Figure 6-5. The x axis in the graph is the spatial frequency. Yet again the y axis depicts the point Rayleigh scatter amplitude of the measurement.

Examining the graph, it is evident that the side lobe offset from the simulated point is equal to the frequency of the vibration signal, an observation that will be consequential during the development of the distributed vibration measurement algorithm.

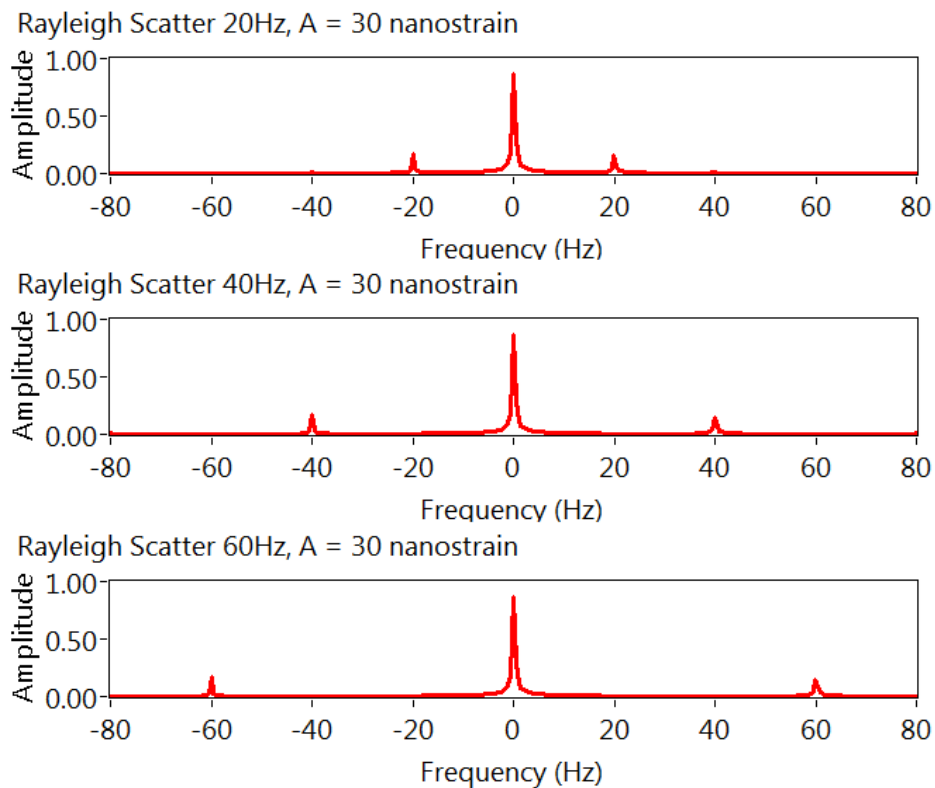


Figure 6-5. Base band-shifted frequency signal of an optical path length =1 at various vibration signal modulation frequencies.

6.1.4 Vibration extraction from single point measurement

Having demonstrated the effects of vibration on a single point along a fiber the focus can now shift to methods of extraction of the vibration effects. By examining Figure 6-5 and looking only at positive frequencies, it can be observed that, absent the 0 frequency term, the amplitude represents the vibration spectrum, or rather, the Fourier transform of the vibration signal. Hence, one can postulate that the eliminating of the terms near the zero frequency and performing an inverse Fourier transform on processed data would yield the vibration time signal. Figure 6-6 shows the procedural recovery of the vibration signal where the input vibration signal is 20Hz. Figure 6-6a) shows the base-band shifted amplitude signal with a rectangular window applied

around the center frequency. Figure 6-6b) is the amplitude of the positive frequencies as a function of frequency. All the frequencies under the rectangular window have been eliminated resulting in the vibration spectrum. Figure 6-6c) shows the inverse Fourier transform of the vibration spectrum. Absent the windowing effects, it is apparent that the resulting signal is the vibration function.

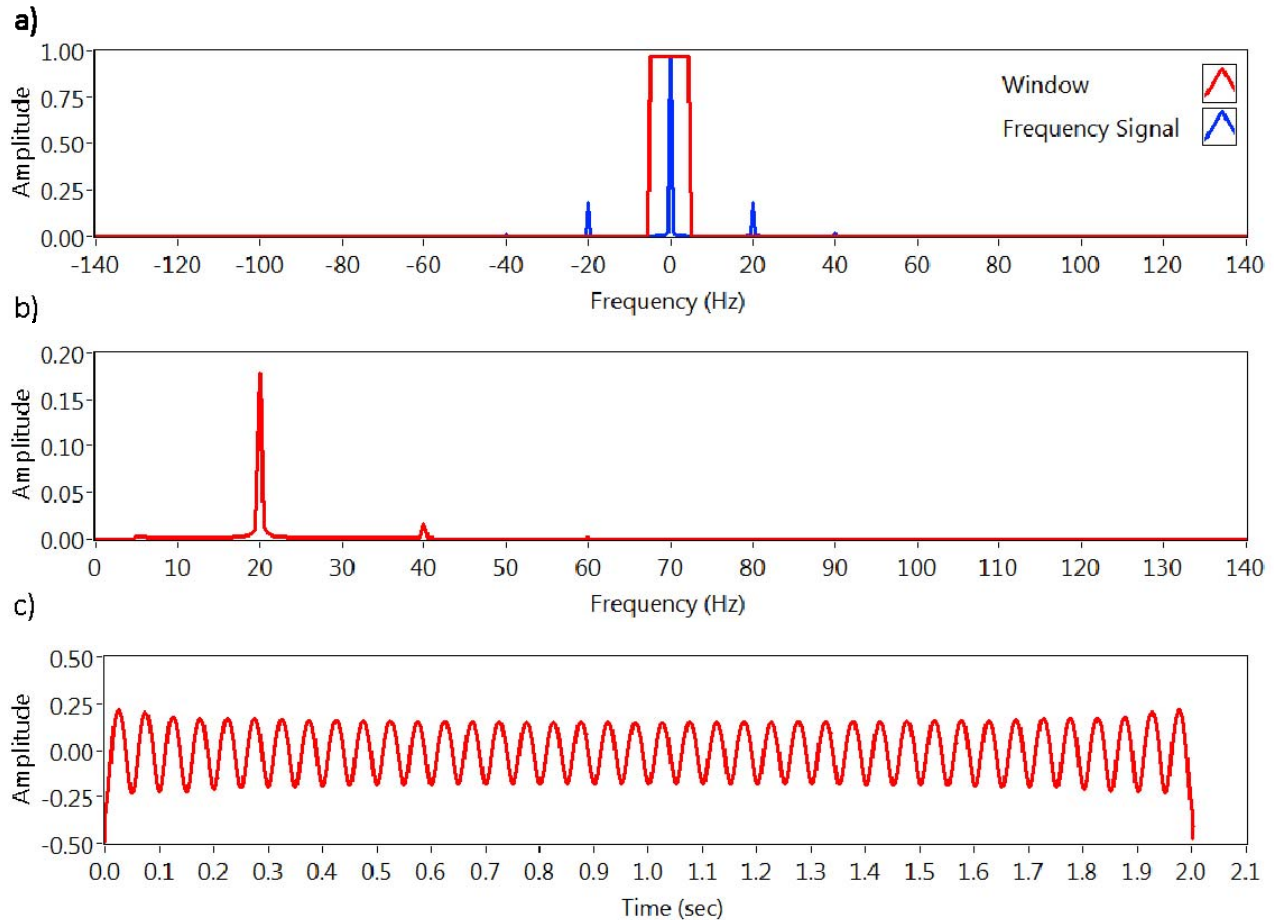


Figure 6-6. Procedural recovery of 20Hz input vibration signal.

Figure 6-7 illustrates successful multi-tonal signal recovery of vibration input frequencies were of 10Hz, 15Hz, and 70Hz using the procedure articulated above.

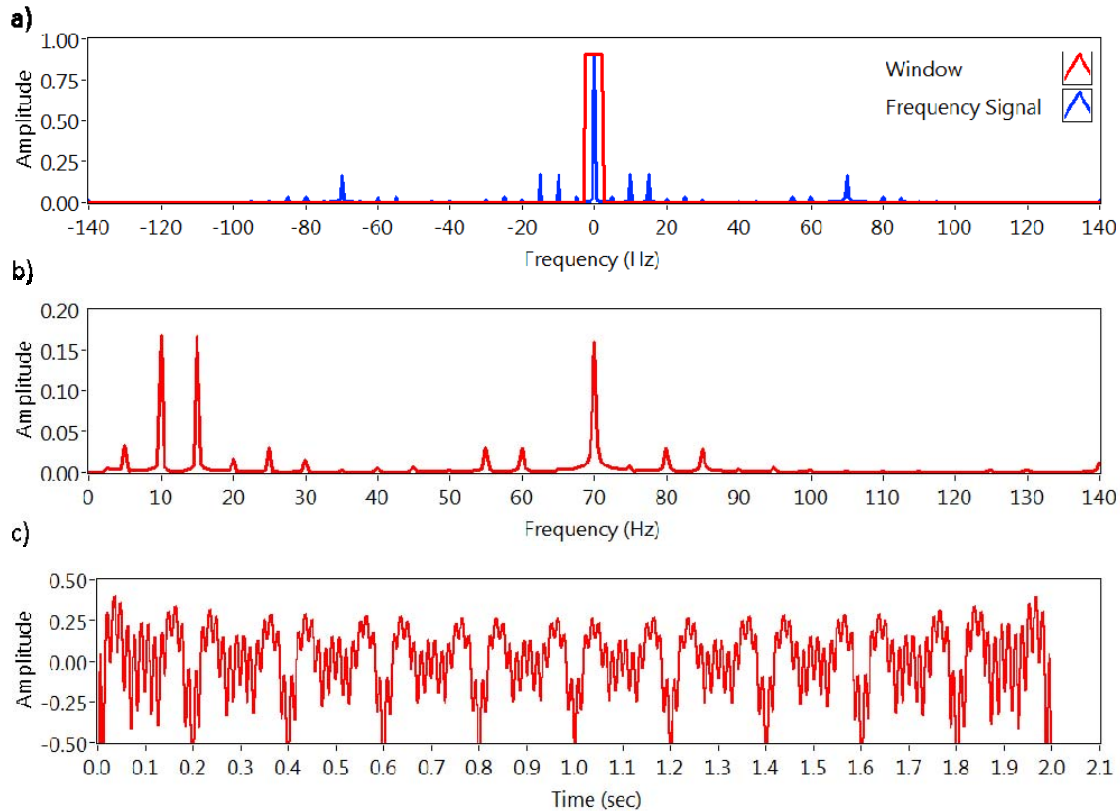


Figure 6-7. Procedural recovery of 10Hz, 15Hz and 25 Hz input vibration signal.

From the single point investigation, it can be concluded that, vibration signals spreads the Rayleigh scatter amongst its nearest neighbors with the smear distance proportional to the amplitude and frequency of the vibration. From a frequency analysis, the symmetric spatial distance from the point of vibration corresponds to spectral bandwidth. As a consequence, if one need account for a high vibration frequency, a correspondingly large fiber segment (and thus a large spectral bandwidth) is required to capture all the coupled content.

It can further be observed that, in the presence of a high contrast reflection, illustrated by the single point in this section, one can recover the vibration spectrum and, thus, the vibration time signal at the specified location, an attribute that will be utilized in the vibration decoupling from the measurement later in this chapter.

6.2 Vibration coupling into a distributed measurement

6.2.1 Dynamic strain only

The investigation is now extended to a continuum of multi-point reflections along the fiber experiencing dynamic strain over a defined region starting at V_s and ending in V_e . Figure 6-8 illustrates the representative optical network.

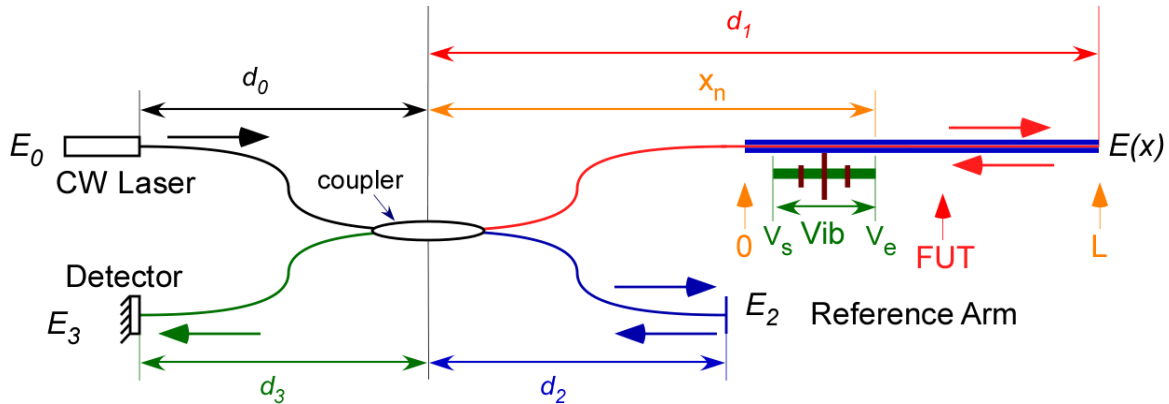


Figure 6-8. Optical network depicting distributed reflection where the FUT is oscillating

Without the dynamic strain effect, it was shown that the field intensity as seen by the optical detector due to the continuum of reflections to be:

$$I_3(t) = 2 \cdot E_2 \cdot \sum_n \left[E_1^n \cdot \text{Cos} \left(\left(\frac{2 \cdot n_{eff}}{c} \cdot (\alpha \cdot t + \omega_0) \right) \cdot (x^n - d_2) \right) \right] \quad (3-73)$$

With a subset of the optical fiber oscillating, the positional array, x^n becomes a function of time. Reformulating equation (3-73) results in:

$$I_3(t) = 2 \cdot E_2 \cdot \sum_n \left[E_1^n \cdot \text{Cos} \left(\left(\frac{2 \cdot n_{eff}}{c} \cdot (\alpha \cdot t + \omega_0) \right) \cdot (x^n(t) - d_2) \right) \right] \quad (6-6)$$

To accurately model $x^n(t)$, one must remember that vibration is a dynamic strain event and, as a consequence, it has a behavior similar to that of static strain described in Section 4.2. For the reader's convenience, is presented again, where the strain relationship to displacement is seen.

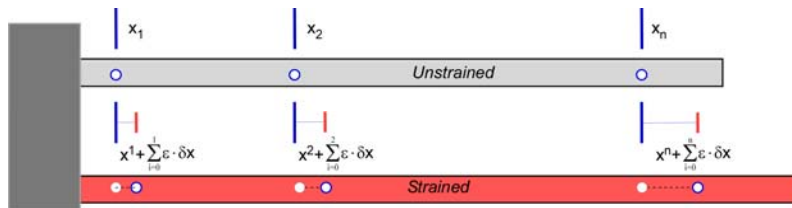


Figure 4-5. Axial strain applied to axial bar

Recall that the strained location of any point positioned along a 1 dimensional element is resolved by the sum of its previous location to the accumulated strain displacement to the point resulting in:

$$x^n \Big|_{strained} = x^n + \sum_{i=0}^n \varepsilon \cdot \delta x^i \quad (4-2)$$

Utilizing equation (6-2), equation (4-2) can be recast to account for time varying relationship as shown below.

$$x^n(t) = x^n + \sum_{i=0}^n [A_{vib}^i \cdot \text{Cos}(\omega_{vib}^i \cdot t)] \quad (6-7)$$

where the term under the summation represents the accumulated vibration to point n . Utilizing equation (6-7) in eqn. (6-6) a discretized form of the time varying intensity signal as seen by the optical detector in a fiber experiencing vibration can be formulated resulting in:

$$I_3(t) = 2 \cdot E_2 \cdot \sum_n \left[E_1^n \cdot \text{Cos} \left(\left(\frac{2 \cdot n_{eff}}{c} \cdot (\alpha \cdot t + \omega_0) \right) \cdot \left(x^n + \sum_{i=0}^n [A_{vib}^i \cdot \text{Cos}(\omega_{vib}^i \cdot t)] - d_2 \right) \right) \right] \quad (6-8)$$

where A_{vib}^n and ω_{vib}^n are functional between V_s and V_e and zero everywhere else.

6.2.2 Vibration and Strain

In instances where vibration and strain are present, equation (6-7) can be recast to include the presence of strain such that:

$$x^n(t) = x^n + \sum_{i=0}^n [\delta x^i + A_{vib}^i \cdot \text{Cos}(\omega_{vib}^i \cdot t)] \quad (6-9)$$

Equation (6-6) can thus be modified using equation to account for both static and dynamic strain (vibration) resulting in:

$$I_3(t) = 2 \cdot E_2 \cdot \sum_n \left[E_1^n \cdot \text{Cos} \left(\left(\frac{2 \cdot n_{eff}}{c} \cdot (\alpha \cdot t + \omega_0) \right) \cdot \left(x^n + \sum_{i=0}^n [\delta x^i + A_{vib}^i \cdot \text{Cos}(\omega_{vib}^i \cdot t)] - d_2 \right) \right) \right] \quad (6-10)$$

6.3 Summary

A theoretical analysis has been performed illustrating how vibration couples into a single vibrating point along a fiber. It was seen that symmetric side-lobes mirrored around the modeled point appeared with an offset and amplitude corresponding to the frequency of and energy of the exciting mechanism. Where the energy is particularly high, the emergence of subsequent side-lobes corresponding to resonant frequencies of the exciting mechanism, appeared, where the offset and amplitude represented the frequency and energy of the resonant frequency.

The theoretical analysis was then extended to a distributed dynamic strain events along a subset of the optical fiber. Equations were also developed for both static and dynamic strain events were present in the optical fiber.

7 Dynamic Strain Simulations and Experiments

This chapter contains computer simulations and experiments performed in support of the theoretical dynamic strain analysis. The simulations described herein begin with a distributed measurement utilizing equations developed in Chapter 6. The work is then extended to a computer simulation and experimental illustration of the capability to measure dynamic strain measurements in a distributed fashion, a feat that to this author's knowledge has never been demonstrated in optical fiber

7.1 Computer Simulation: Vibration Only

A simulation model was used to generate Rayleigh scatter in an unstrained state based on equation (6-8) using the procedure discussed in section 3.2.2. A 33 cm fiber segment with a 20 micron two point resolution with reflective events at 3 cm and 30 cm was modeled. A monotonic vibration signal with amplitude and frequency of 90×10^{-9} m and 20Hz was induced between 10 and 25 centimeters. The simulated parameters used to generate the signal were a laser sweep rate of 10nm/sec, a range of 40nm and a center wavelength of 1550 nm. Figure 7-1. shows the results.

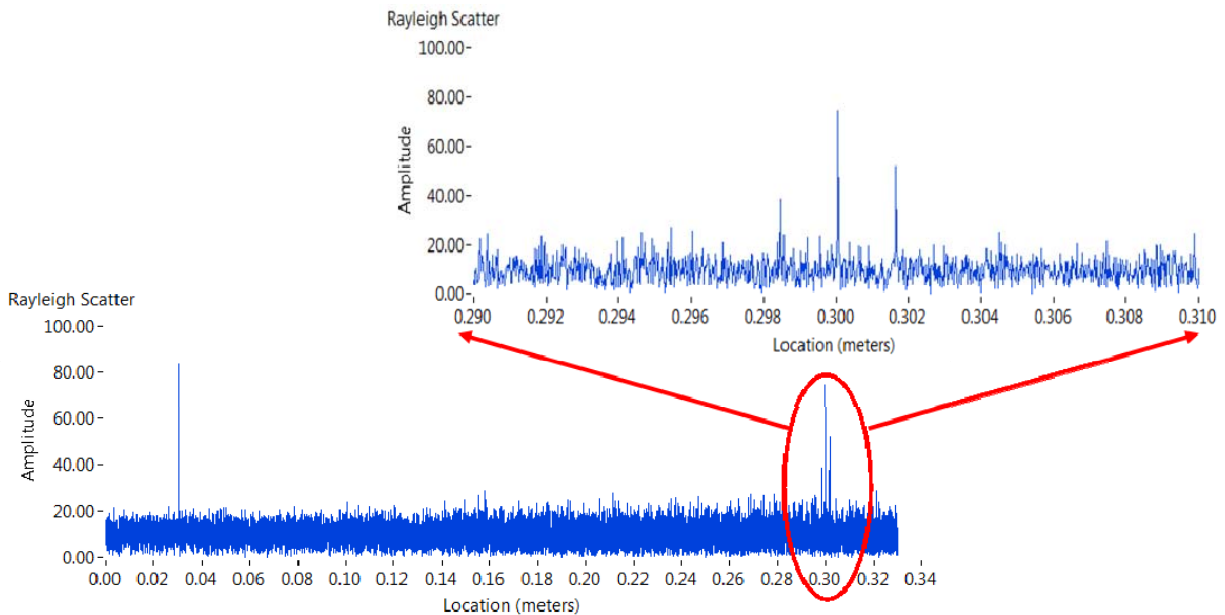


Figure 7-1. Modeled Rayleigh scatter with a 20Hz vibration signal perturbing the fiber

An inspection of the end reflection modeled 30cm down the fiber reveals the emergence of two spatially symmetric side lobes, a phenomenon similarly seen in the single-point analysis. Based

on equation (6-8), it can be stated that these side lobes represent the accumulated vibration along the length of the fiber.

Knowing the accumulated vibration by examining the end reflection is good, but it falls short of the goal of understanding the vibration as a function of position. To accomplish this, a way to obtain a high contrast peak along the entire length of the fiber will need to be determined. Recall the computation of the temporal and spectral shift terms in Section 4.4. For review, the temporal shift term is the cross-correlation of a baseline and measurement acquisition in the temporal space (the domain where the Rayleigh scatter is a function of position), whereas the spectral shift is the cross correlation of the same dataset after taking a Fourier transform. To propagate the shift terms along the fiber, one discretizes the fiber length into segments and processes each segment for temporal and spectral shift values.

To generate the correlation curves, vibration-free Rayleigh scatter data is modeled to the same specifications indicated at the beginning of this section, to be used as a reference for the cross correlation. Figure 7-2 and Figure 7-3 show spectral and temporal and shift curves at various locations on the fiber with and without vibration present. The curves were generated by cross-correlating a 2cm vibration-free reference segment with the vibration induced fiber at various points along the fiber covering regions with and without vibration.

Examining the spectral shift graphs, a correlation peak at the zero lag state that diminishes in amplitude is evident as one advances along the fiber. Inspecting the temporal shift, it is evident that the amplitude decay as a function of position. The emergence and growth in amplitude of side lobes is also apparent as one migrates down the fiber, a clear indication of vibration.

Two key effects of vibration that will be utilized moving forward are the amplitude decay (of both the temporal and spectral shift) and the emergence of side lobes in the temporal shift. The amplitude effect will be used to quantify the signal quality (i.e. the signal to noise ratio), whereas the side lobes will be used to reconstruct the vibration signal.

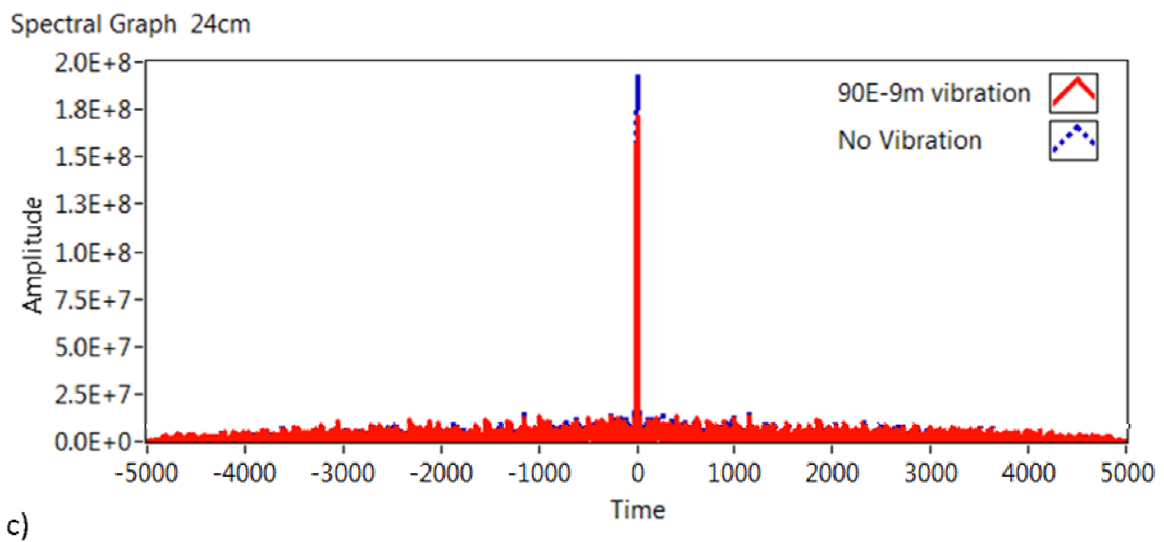
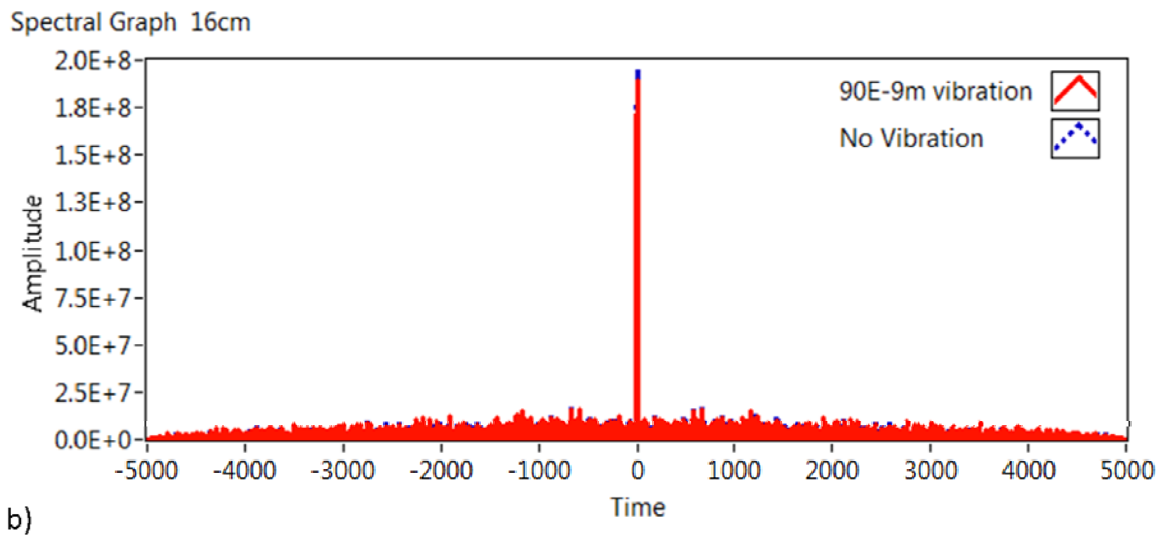
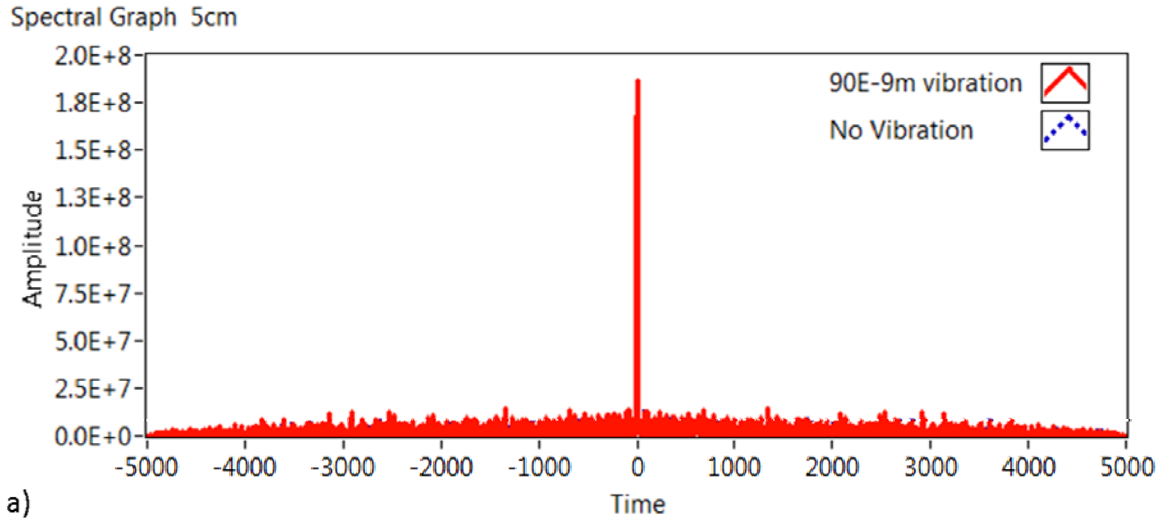


Figure 7-2. Spectral shift curves at various points of the fiber

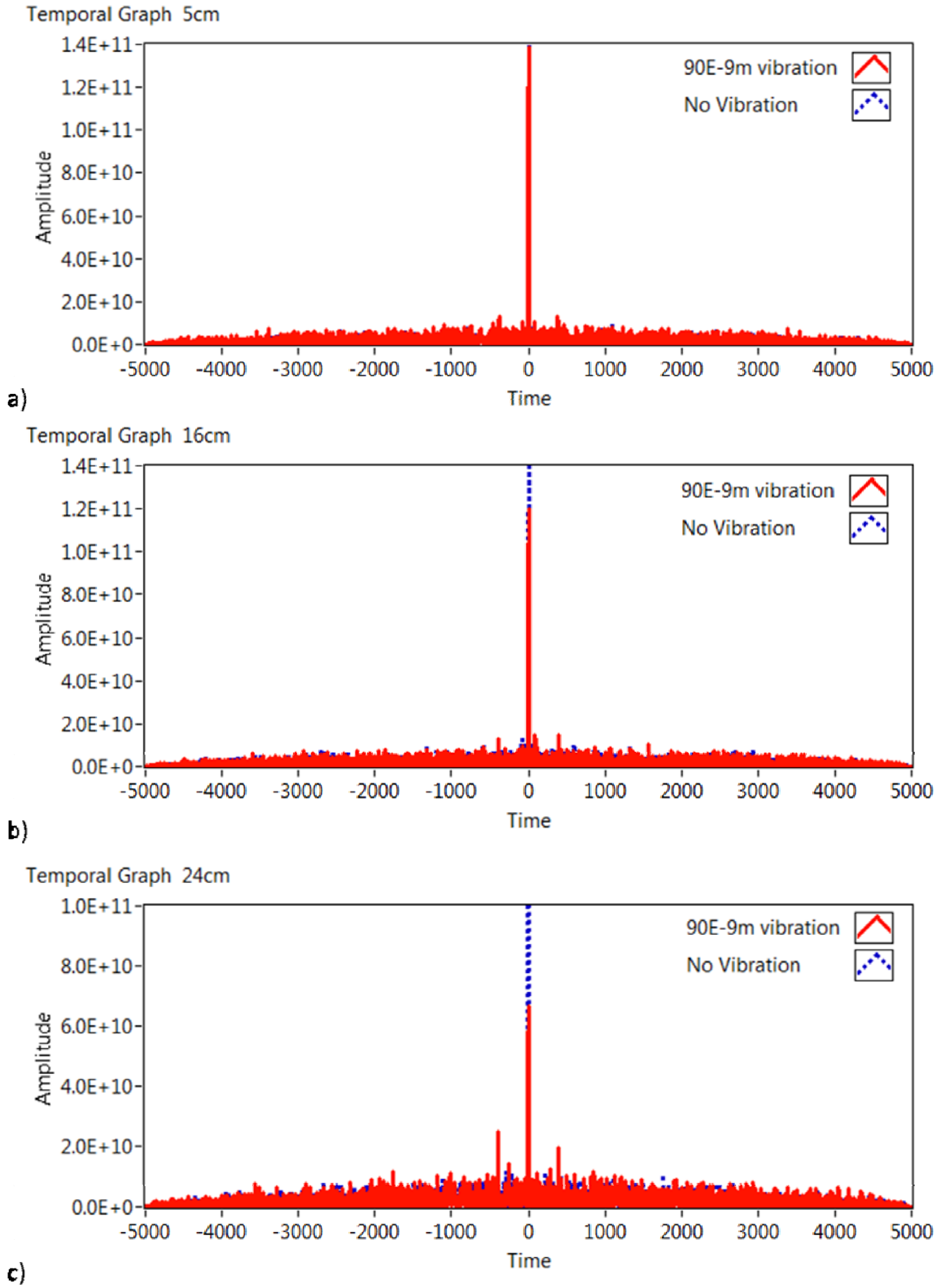


Figure 7-3. Temporal shift curves at various points of the fiber

Normalizing the signal amplitude with the average noise amplitude, one can develop an amplitude based signal quality parameter for both the temporal and spectral shift that can be used to quickly quantify the vibration effects during the modeling and subsequent testing as illustrated in Figure 7-4 and Figure 7-5.

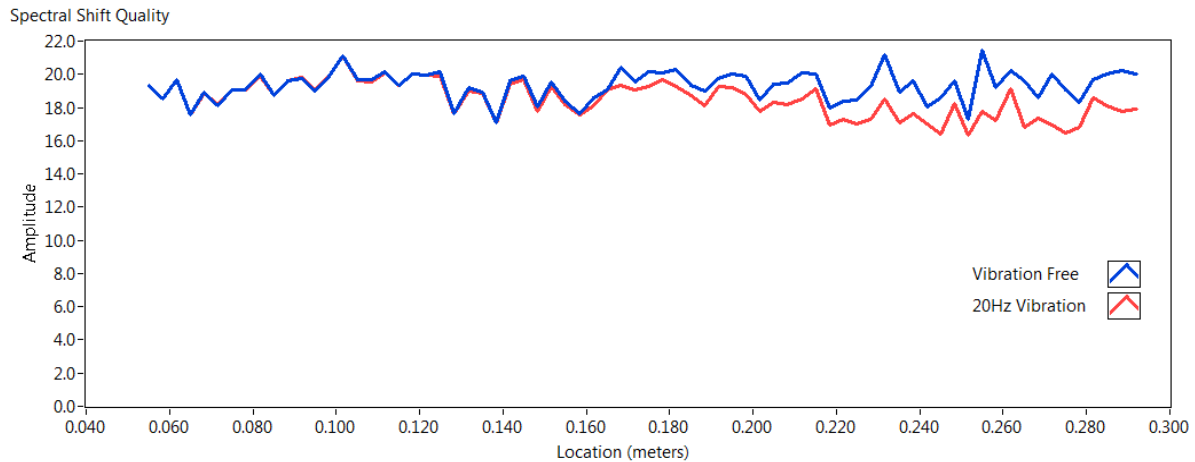


Figure 7-4. Spectral shift quality as a function of position. Reference compared to 20Hz vibration

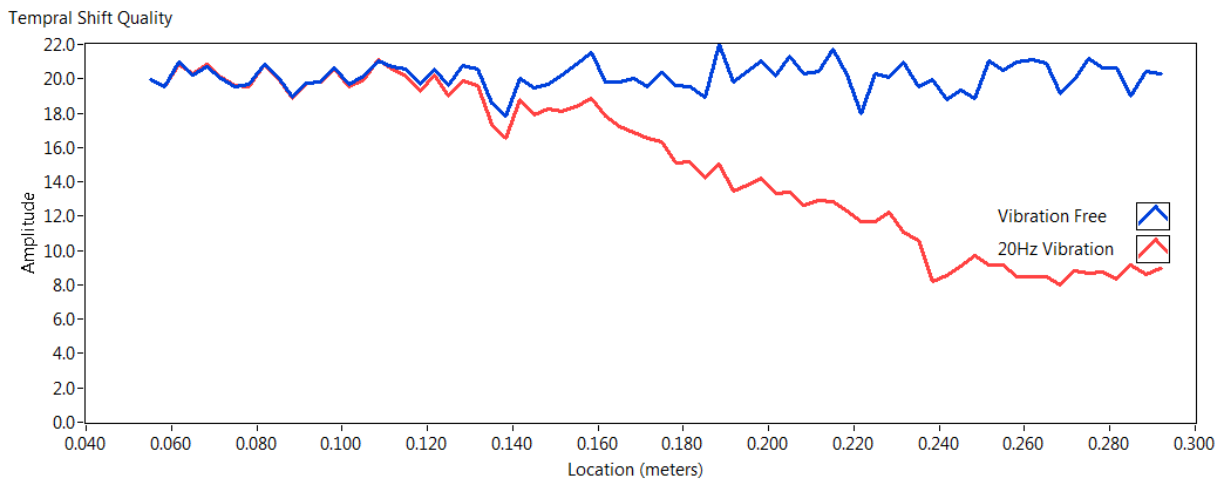


Figure 7-5. Temporal shift quality as a function of position. Reference compared to 20Hz vibration

The shift quality parameters show immediate signal decay as a function of position after vibration introduction at the 10cm location. The signal deterioration is more apparent in the temporal shift quality confirming the spot analysis demonstrated in Figure 7-5.

To this point, a way to create a high-contrast peak by comparing the perturbed state to a vibration free reference and performing a cross correlation in the temporal domain has been determined. The presence of vibration has a dual effect of amplitude decay and side lobe emergence. Utilizing techniques discussed in the single point analysis, the vibration seen at the region of the

temporal cross correlation can be reconstructed. However, recall that the vibration is cumulative. Therefore, any extracted signal via the temporal cross-correlation will represent the accumulated vibration from the front end of the fiber, to the point of cross correlation. Thus, in order to uniquely identify the vibration at anyone point, one needs to devise a mechanism to subtract *a-priori* content previous to the point of interest from all points ahead.

From the above, the emergence of a framework for a vibration measurement algorithm can be seen. First, a reference measurement that is vibration-free is required for use as a basis of comparison with subsequent measurements. Next, a temporal cross correlation starting at the beginning of the fiber on a fixed segment width is performed. A side lobe analysis is done and used to reconstruct the vibration signal. The extracted signal is subtracted from all subsequent points in the fiber. The process is repeated at the next segment, continuing with the process until the reaching the end of the fiber.

Figure 7-6 shows the vibration as a function of time and the corresponding Fourier transform at various locations along the modeled fiber after processing with the algorithm described above. It is clear that, at the points between 10cm and 25cm (the region where vibration was introduced in the simulation), the vibration content of similar amplitude at a frequency of 20Hz is extracted. The points 5cm and 30cm (outside the region of vibration) show low-amplitude, broad-spectrum noise absent of the 20Hz signal.

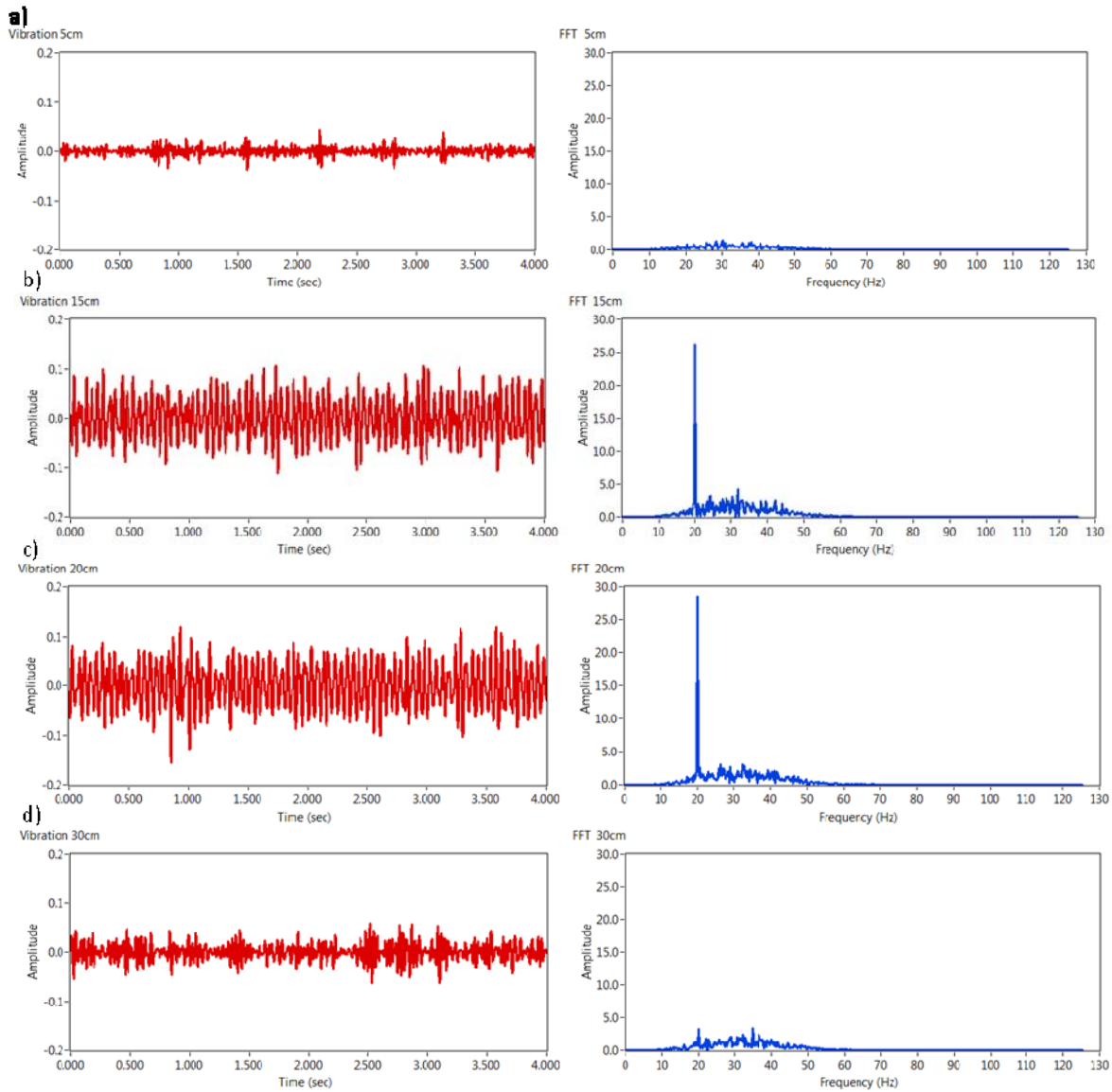


Figure 7-6. Vibration Signal at various locations along the fiber after processing with algorithm

A beneficial consequence of the procedure highlighted above is that the perturbed fiber is progressively cleaned of vibration. The expected result is that spectral and temporal shift quality parameters will improve and the attenuated end reflection of the fiber will recover compounded by the elimination of the emergent side lobes.

Figure 7-7 shows the Rayleigh scatter of the fiber modeled with a 20Hz vibration perturbation (as shown in) after processing with the vibration measurement/correction algorithm. In the figure, the recovery of the peak amplitude and the elimination of the side lobes is seen, evidence of the extraction of the vibration from the fiber.

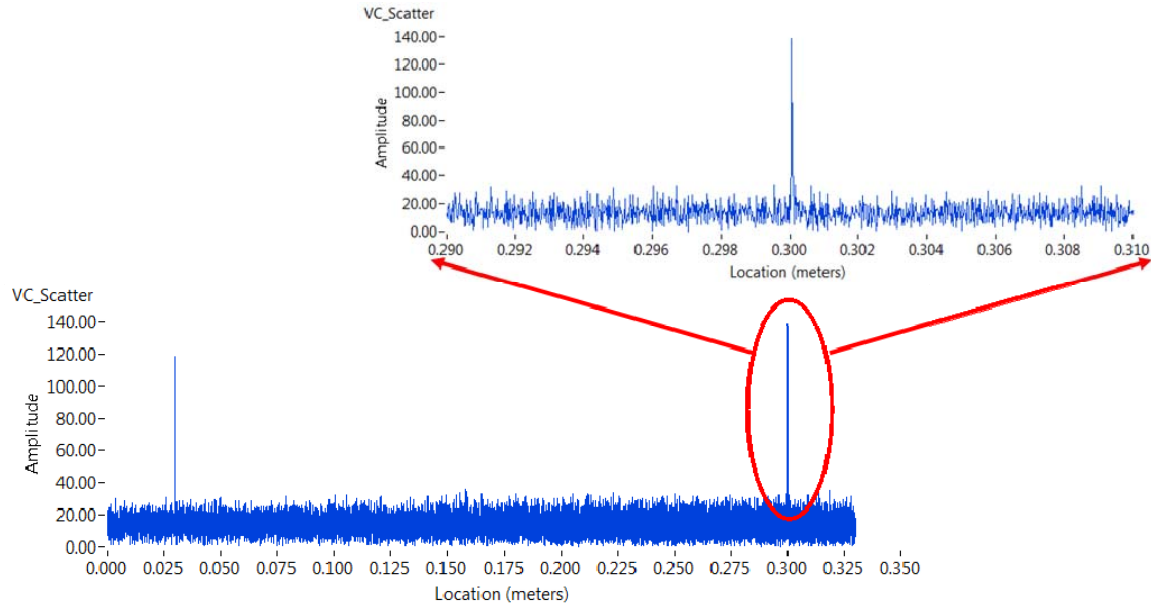


Figure 7-7. Rayleigh Scatter of fiber perturbed with 20Hz signal after vibration correction

Figure 7-8 and Figure 7-9 show the spectral and temporal shift quality as a function of position in the vibration free, perturbed and post measurement/correction state. It is clear that in both the temporal and spectral quality graphs, the algorithm recovers the fidelity of the signal. This is supported by the return of the shift quality to the pre-vibration state at regions at or after the region of vibration.

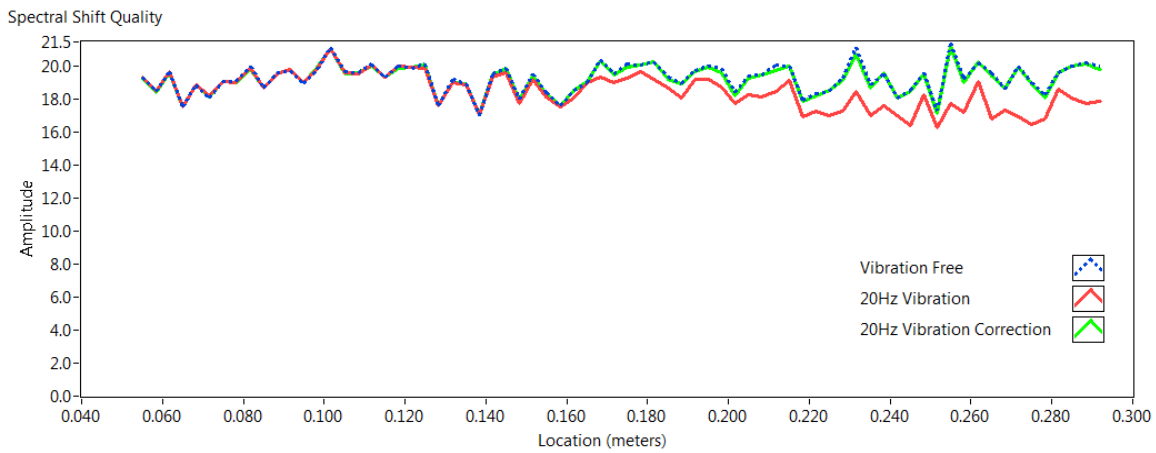


Figure 7-8 Spectral shift quality as a function of position for the fiber at states

The temporal shift quality sees a more aggressive recovery compared to the spectral shift, where a recovery from a low 8 to the nominal range of 22 is seen.

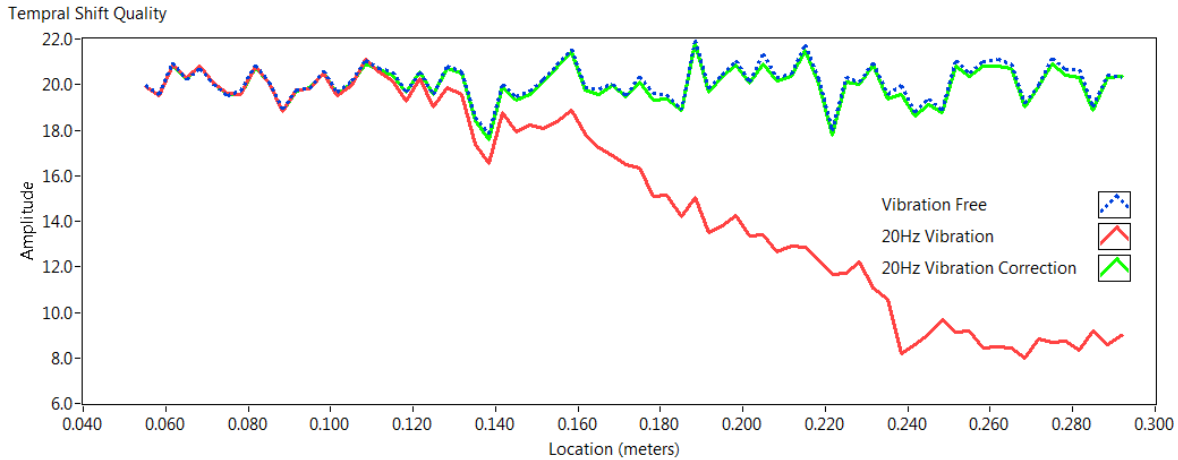


Figure 7-9. Temporal shift quality as a function of position for the fiber at states

7.2 Computer Simulation: Strain and Vibration

Utilizing the intensity model as seen by the detector as described in equation , one can proceed with a simulation of Rayleigh scatter experiencing both strain and vibration by implementing the procedure discussed in section 3.2.2. As was done previously, a 33 cm fiber segment with a 20 micron two point resolution with reflective events at 3 cm and 30 cm was modeled. A monotonic vibration signal with amplitude and frequency of 120×10^{-9} m and 20Hz was induced between 8cm and 18 cm. Further, a $400 \mu\epsilon$ strain field was applied between 10cm and 25cm.

The simulated parameters used to generate the signal were a laser sweep rate of 10nm/sec, a range of 40nm and a center wavelength of 1550 nm. Figure 7-10 shows the modeled results where the attenuation of the end reflection and the emergence of multiple peaks is seen, representing the 20Hz signal and higher ordered modes, present. It is also worth noting that the expected peak event modeled at 30cm is attenuated to a level lower than the vibration modal peaks.

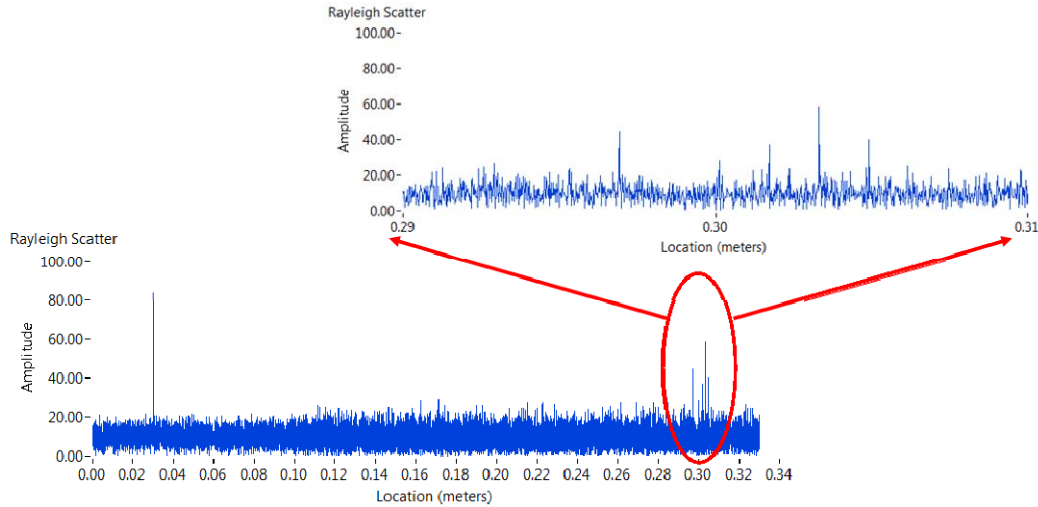


Figure 7-10. Rayleigh Scatter of fiber perturbed with 20Hz signal and 400 $\mu\epsilon$ strain field

Figure 7-11 shows the Rayleigh scatter after correction of the 20Hz vibration perturbation after processing using the vibration measurement/correction algorithm. The multiple peak events previously scattered in the vicinity of the end peak are reconstructed at the expected location, 30cm down the fiber, the region where the end termination was modeled.

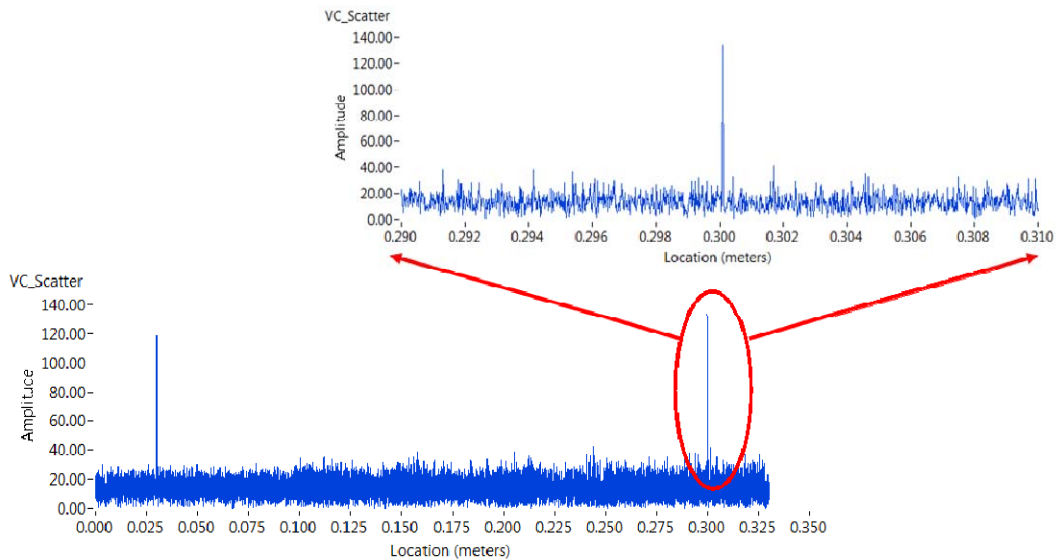


Figure 7-11. Rayleigh Scatter of fiber after correction of 20Hz vibration signal where a 400 $\mu\epsilon$ strain field present

The overall effectiveness of the vibration correction can be examined by inspecting the temporal and spectral shift quality parameters. Figure 7-12 shows the temporal shift as a function of position in the vibration free, perturbed and post measurement/correction state. The signal to noise ratio (SNR) is recovered until 24cm down the fiber, where the algorithm yields improved results relative to vibrated state, but less than the original SNR.

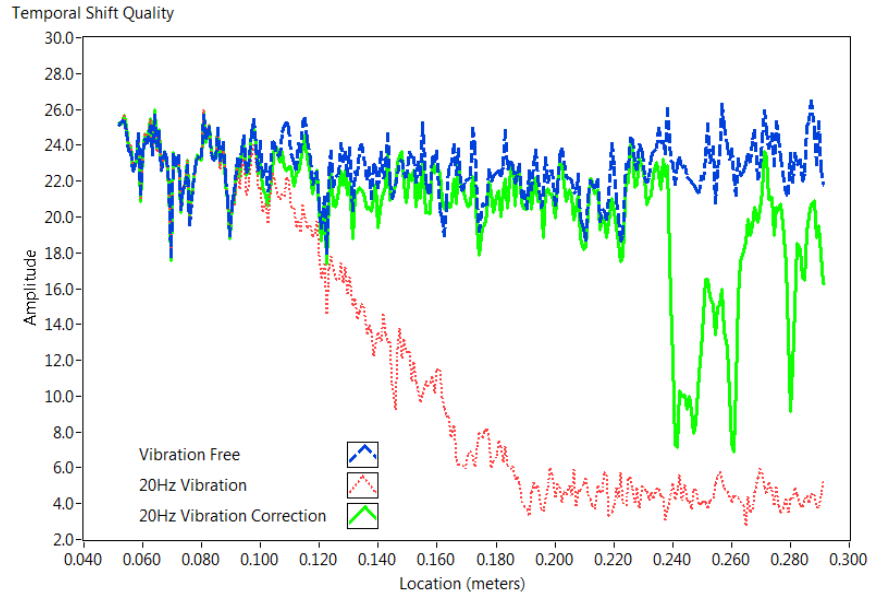


Figure 7-12. The temporal shift quality of strained fiber at before, with and after vibration correction

Figure 7-13 shows the spectral shift quality as a function of position in the vibration free, perturbed and post measurement/correction state. Yet again, signal recovery is obtained until 24cm, where degraded SNR relative to the unperturbed state is evidenced.

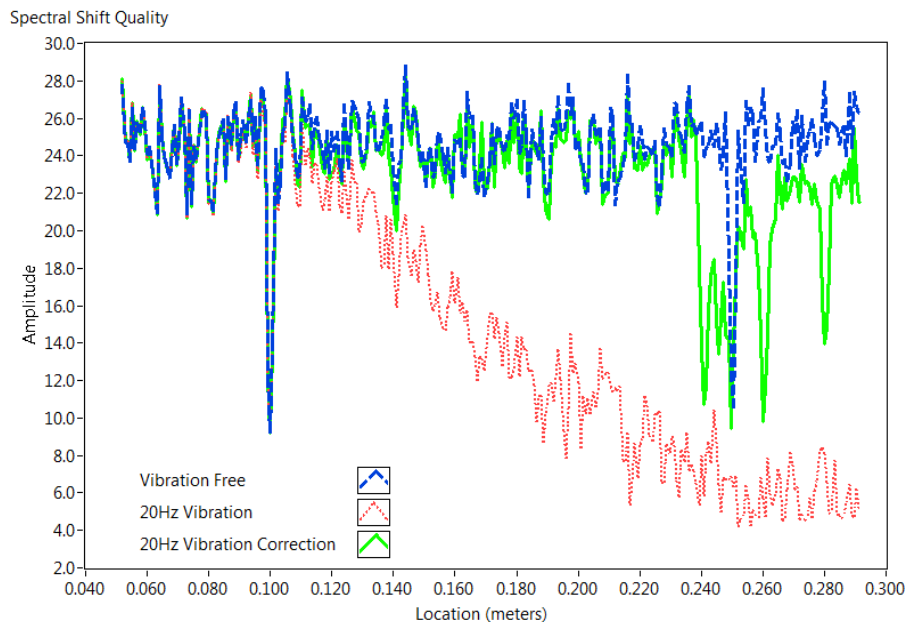


Figure 7-13. The spectral shift quality of strained fiber at before, with and after vibration correction

A hypothesis for the degraded performance is the high strain gradient between the strained and unstrained sections of fiber which, as discussed in Section 1, leads to reducing SNR, where one utilizes a constant strain approximation as one performs a cross correlation to yield the shift

parameters. It is worth noting that in this model, a linear strain approximation model was not implemented as evidenced in the degradation of the SNR in the vibration free state of the spectral shift quality into and out of the strained region.

Figure 7-14 shows the vibration as a function of time and the corresponding Fourier transform at various locations along the modeled fiber after vibration correction.

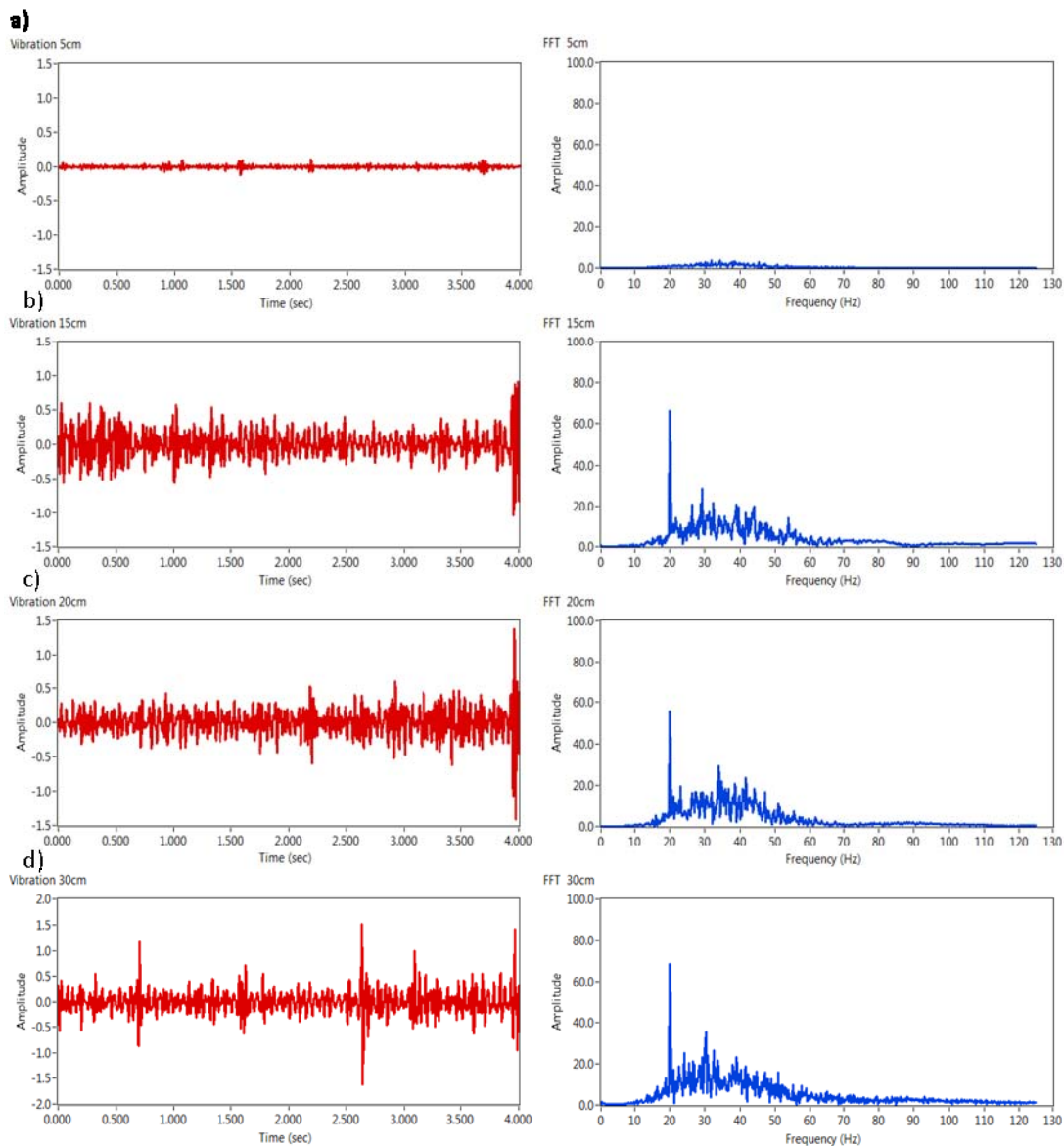


Figure 7-14. Rayleigh Scatter of fiber perturbed with 20Hz signal and $400\mu\epsilon$ strain field

As expected, vibration content is absent at 5cm. A 20Hz signal is present at 15cm, 20cm and 30cm. However, in the model, the 30cm point is outside the region of applied vibration. This indicates a failure of the algorithm to extract the vibration content from the fiber from points

previous to the 30cm location. It is theorized that this is a consequence of the reduced SNR due to the strain gradient at the end of the applied region, leading to an inaccurate vibration signal. It is also hypothesized that the introduction of a linear strain approximation within the vibration measurement algorithm infrastructure will address this deficiency.

Figure 7-15 shows the strain as a function of position in the vibration free and perturbed state. A sensor gage length and spacing of 4mm and 1mm respectively was used for this computation. As the end of the strain field is neared, the perturbed state begins reporting spurious data and does not recover past the strained location.

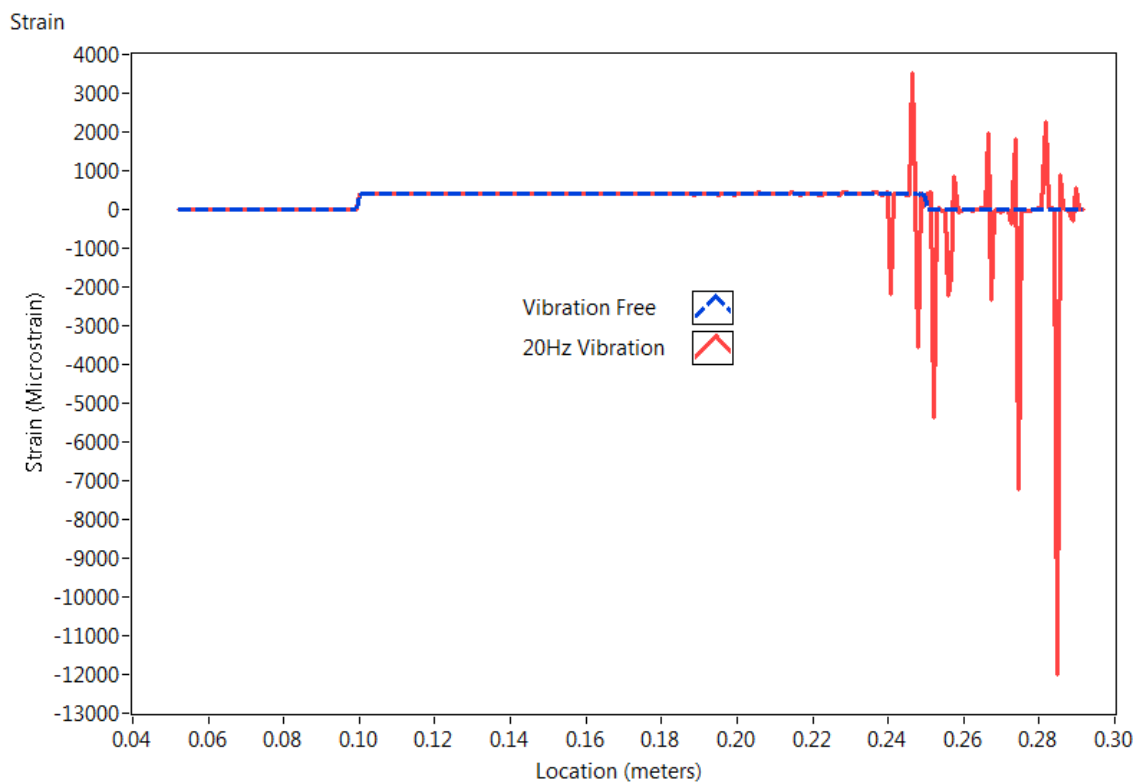


Figure 7-15. Strain as a function of position of the vibration free and vibrating segment

Figure 7-16 shows the strain as a function of position in the vibration free and post measurement/correction state. The recovery of the strain across the full domain is noted with small deviations from the expected results after the 24cm mark.

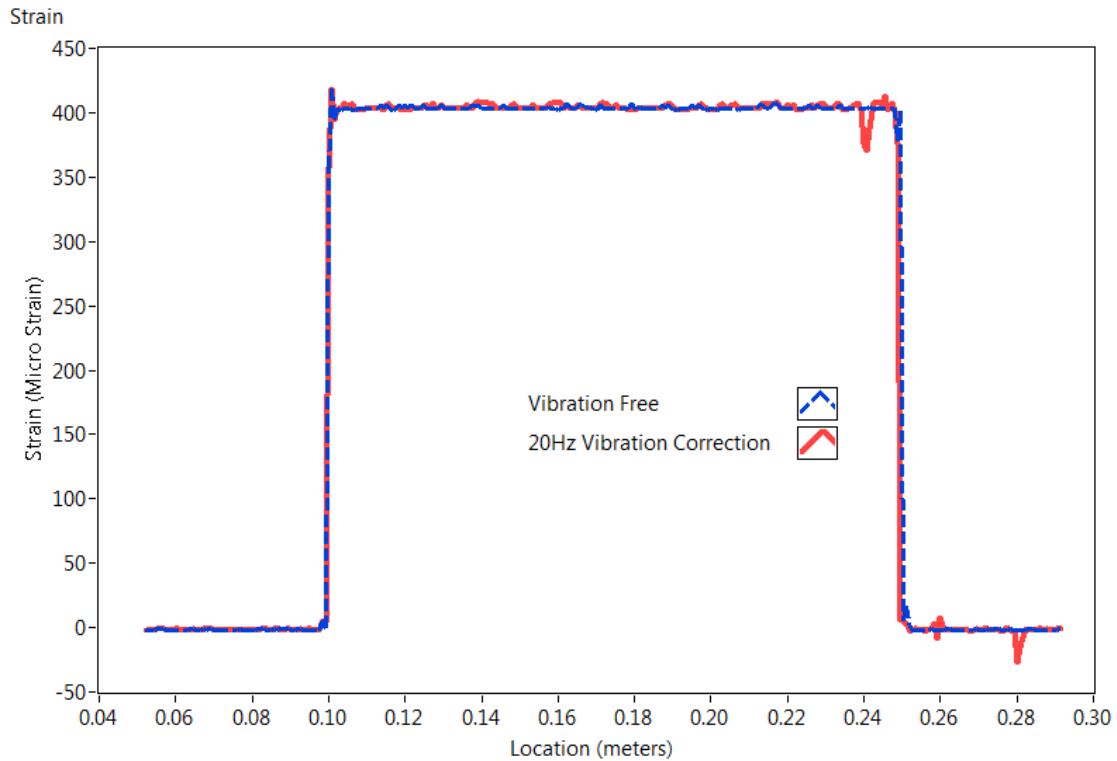


Figure 7-16. Strain as a function of position of the vibration free and vibration corrected segment

7.3 Experimental implementation of strain and vibration algorithm

To supplement the numerical simulation, a subset of the analysis was repeated experimentally. Figure 7-17 shows the experimental setup utilized for this demonstration. An optical fiber was anchored to both a beam cantilevered from a support post and a speaker. One end of the fiber was attached to an Optical Backscatter Reflectometer with the other placed on the test bench in the vicinity of the setup. A signal generator was used to impart a controlled vibration signal into the setup during data acquisition. A uniform vibration was applied to the fiber by migrating the cantilevered beam away from or toward the speaker.

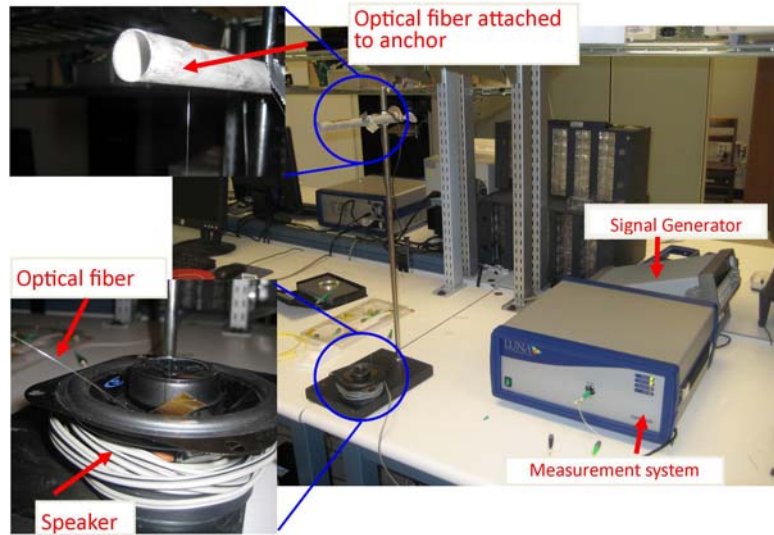


Figure 7-17. Experimental setup for vibration extraction modeling.

Figure 7-18 shows the end peak reflection of Rayleigh scatter acquired using the Optical Backscatter Reflectometer (OBR) before and after vibration correction. A 20Hz, 2 Volt peak-to-peak signal was induced using the signal generator and speaker. Further, an arbitrary constant strain field was applied by translating the cantilevered tubular away from the speaker, resulting in fiber elongation.

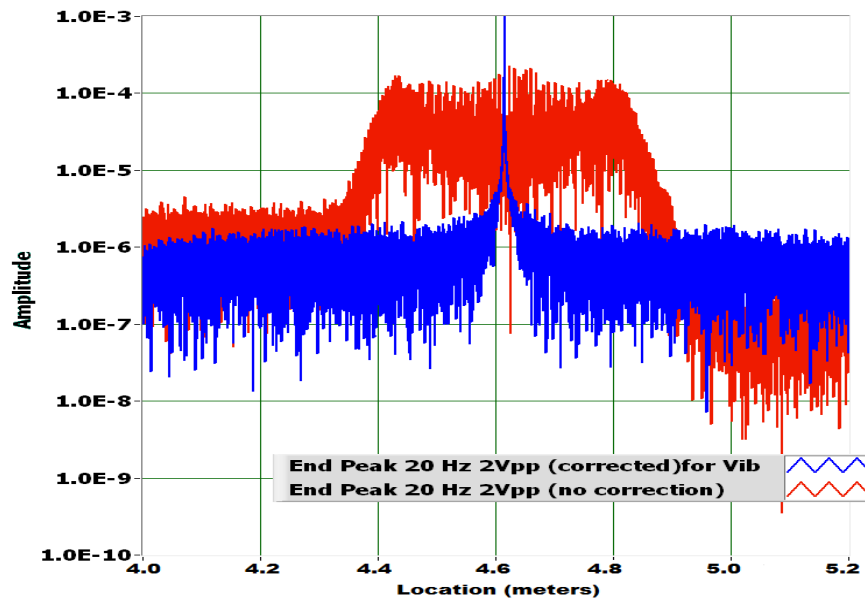


Figure 7-18. End peak reflection of strained optical fiber before and after vibration correction where a 2Vpp 20Hz vibration was induced to the measurement.

The OBR was configured to traverse a 20nm wavelength range centred at 1550 nm at a sweep rate of 10nm/sec. As was seen in the simulation, a recovery of the end peak reflection after

processing and extracting the vibration content is seen using the measurement/correction algorithm.

Figure 7-19 shows the spectral shift as a function of position in the vibration perturbed and corrected state of the experimental data. A sensor gage length and spacing of 1cm and 0.3 cm respectively was used to compute the strain along the fiber. As was seen in the strain simulation, the appearance of spurious data as one progresses across the constant strain field is seen, without recovery past the strain location due to the accumulation of vibration content.

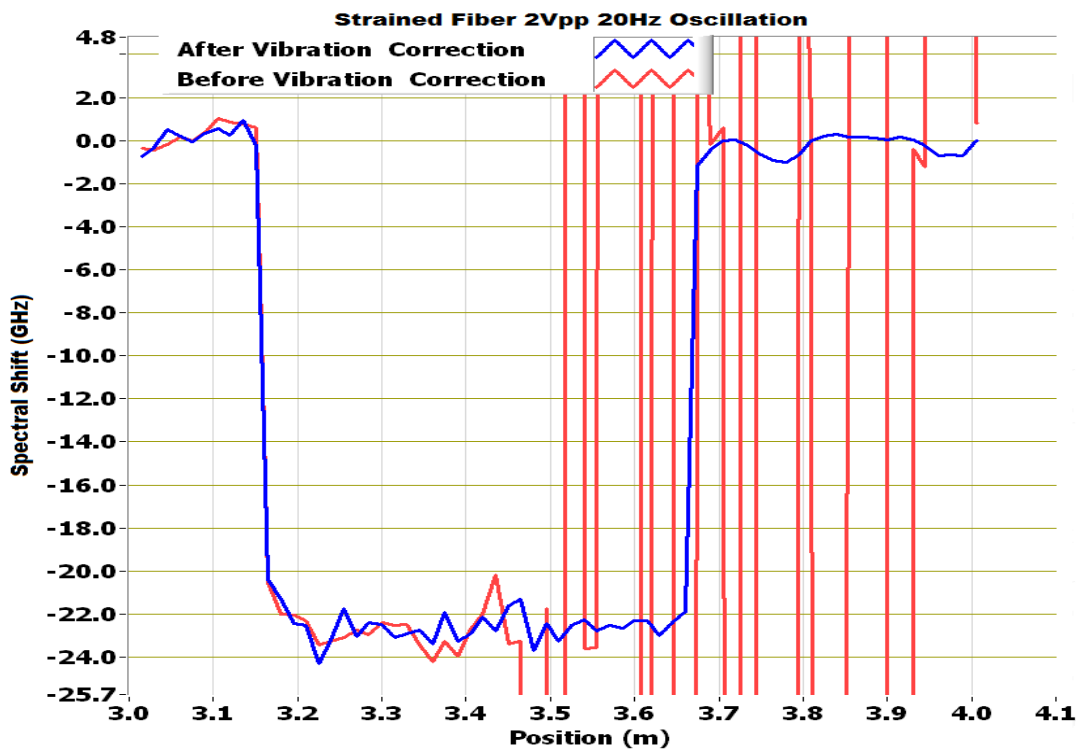


Figure 7-19. Spectral shift as a function of position of the vibration and vibration corrected segment

Figure 7-20 shows the spectral shift as a function of position in the vibration free and post measurement/correction state. The recovery of the strain content after vibration extraction across the full domain is noted.

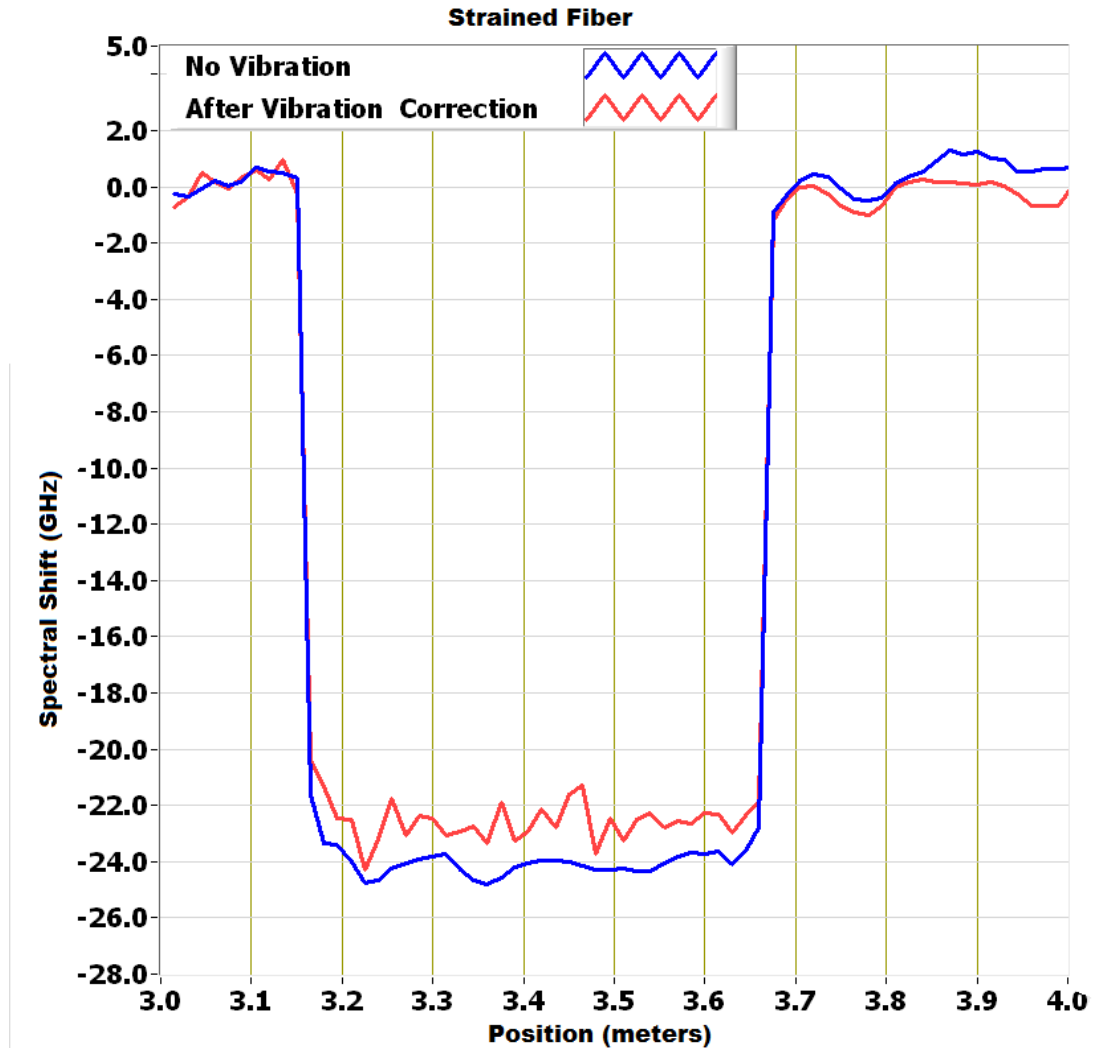


Figure 7-20. Spectral shift as a function of position of the vibration free and vibration corrected segment

7.4 Summary

From the experiment and simulation, it can be concluded that one can measure and correct for vibration in an optical fiber and, consequently, recover the static strain or temperature from the fiber if such were desired. It is also clear that the algorithm can be further optimized to improve results in the vicinity of high gradients through the implementation of a higher-order strain approximation during the computation of the cross correlation in the algorithm.

8 Summary and conclusions

In this chapter, a summary of content discussed is presented, highlighting core goals attained during the investigation. Components that require continued investigation to further advance this effort are then mentioned including aspects deemed useful to both industry and academia. Concluding remarks are then made.

8.1 Summary

The primary motivation behind this study was to supply engineers and scientists a new tool to measure vibration in a simple, yet effective, layout as a continuum over the device under test. The ability to determine the position-correlated vibration evolution of a structure will provide engineers the capability to improve structural design for future components and structures, while implementing robust structural health monitoring, with the capability to detect failure locations, for existing civil structures. An optical fiber sensing technique for vibration monitoring was determined to be the optimal method of choice because of inherent characteristics such as its light weight, EMI immunity and the need of a single source to stimulate the full fiber length.

Various distributed measurement techniques were discussed to give an overall understanding of current, commonly used distributed parameter measurement techniques used in various industries. A thorough description of the Optical Frequency Domain Reflectometry (OFDR) technique, the core foundation of this investigation, was then presented. A demonstration of single-point and multi-point reflection measurements relative to the OFDR technique was discussed supplemented with experimental and simulation data.

A presentation on the measurement of static strain was given as a foundation to the dynamic strain (vibration) analysis. The investigation began by tracing the data flow from the point of acquisition to the analysis and presentation of strain measurements. A successful demonstration of how one could acquire distributed strain or temperature from Rayleigh scatter was demonstrated. That was accomplished by forming deterministic content from the random, but static, arrays through a cross-correlation between a reference and subsequent measurement acquisitions. The mathematical operation was shown to yield a phase term that could be used to determine strain or temperature using either a temporal or spectral algorithm. It was also

demonstrated how the spectral technique can be modified to accommodate aggressive gradients along the fiber path that would otherwise lead to spurious content.

An illustration of how dynamic strain couples into Rayleigh backscatter in both a single-point and a multi-point array was presented. The obtained knowledge was then used to develop a new and unique distributed vibration measurement algorithm that was successfully demonstrated. A beneficial effect of the vibration measurement was the cleaning of the perturbed fiber leading to the recovery of the static strain or temperature field from an otherwise immeasurable state. A simple experimental implementation of the theory was accomplished.

8.2 Conclusions

From this investigation, it can be concluded that it is feasible for distributed vibration measurements to be acquired using telecommunications grade, single-mode optical fiber using the OFDR technique. A beneficial consequence to the vibration measurement is the “cleaning” or otherwise diminishing the effects of vibration on the perturbed fiber leading to the recovery of static strain or temperature measurements. It was also clear that the algorithm could be optimized to improve results in the vicinity of high gradients through the implementation of a higher-ordered strain approximation during the computation of the cross correlation in the algorithm.

8.3 Future work

An extension of this work could be made by improving the simulation model to include a random vibration, inherent fiber dispersion effects, laser tuning non-linearity, variable Rayleigh amplitude, etc. This would allow for further algorithm optimization based on lessons learned from the effects of the introduced parameters. One could extend the model, with small modification, to model fiber Bragg Gratings (FBGs), elements commonly used in distributed sensing measurements. This would allow for algorithm optimization where FBGs are the main elements used for distributed sensing.

This work could be extended to include a numerical simulation and experimental work on mode shape extraction from the distributed, dynamic strain measurements. This would allow for real time mode shape analysis of the aircraft structure during aircraft operation without sacrificing distributed static measurements such as temperature or strain.

9 Appendix A: Optical Path Length relationship Development

Given τ_1 and τ_2 are time of flight measurements from the laser to the detector of each of the two paths under investigation, the terms may be defined as constituents of the characteristic lengths:

$$\tau_1 = \frac{n}{c} \cdot (d_0 + 2 \cdot d_1 + d_3) \quad (11)$$

$$\tau_2 = \frac{n}{c} \cdot (d_0 + 2 \cdot d_2 + d_3) \quad (12)$$

Where d_0, d_1, d_2 and d_3 are the laser path, the measurement path, the reference path and the detector path respectfully. Defining the optical path length, $\Delta \tau$ difference as the difference between τ_1 and τ_2 resulting in:

$$\Delta \tau = \tau_1 - \tau_2 \quad (13)$$

$$\frac{n}{c} \cdot (d_0 + 2 \cdot d_1 + d_3) - \frac{n}{c} \cdot (d_0 + 2 \cdot d_2 + d_3) \quad (14)$$

$$\frac{n}{c} \cdot (d_0 + 2 \cdot d_1 + d_3 - d_0 - 2 \cdot d_2 - d_3) \quad (15)$$

$$\frac{n}{c} \cdot (2 \cdot d_1 - 2 \cdot d_2) \quad (16)$$

$$\frac{2 \cdot n}{c} \cdot (d_1 - d_2) \quad (17)$$

Now, one can linearly vary d_1 between $[0, L]$ such that:

$$d_1(x) = M \cdot x + C \quad (18)$$

Where M and C is the slope and intercept. The expected values of the function at the integration limits can then be specified.

$$d_1(0) = d_{Start} \quad (19)$$

$$d_1(L) = L \quad (20)$$

Solving for M and C from equation (18) resulting in:

$$d_1(0) = d_{Start} = M \cdot 0 + C \quad (21)$$

$$C = d_{Start} \quad (22)$$

$$d_1(L) = L = M \cdot L + d_{Start} \quad (23)$$

$$M = \frac{L - d_{Start}}{L} \quad (24)$$

$$M = 1 - \frac{d_{Start}}{L} \quad (25)$$

Substituting equations (22) and (25) into equation (18) results in:

$$d_1(x) = \left(1 - \frac{d_{Start}}{L}\right) \cdot x + d_{Start} \quad (26)$$

Using equations (17) and eqn. (26), the optical path length difference, $\Delta\tau$ as a function of x may now be defined as:

$$\Delta\tau(x) = \frac{2 \cdot n}{c} \cdot (d_1(x) - d_2) \quad (27)$$

$$\frac{2 \cdot n}{c} \cdot \left(\left\{ \left(1 - \frac{d_{Start}}{L} \right) \cdot x + d_{Start} \right\} - d_2 \right) \quad (28)$$

$$\underbrace{\frac{2 \cdot n}{c} \cdot \left(1 - \frac{d_{Start}}{L} \right) \cdot x}_{M_\tau} + \underbrace{\frac{2 \cdot n}{c} \cdot (d_{Start} - d_2)}_{C_\tau} \quad (29)$$

$$M_\tau \cdot x + C_\tau \quad (30)$$

10 Appendix B: Frequency related to Instrument Parameters

In order to model the optical intensity seen at the detector of the Michelson interferometer where the measurement mirror is oscillating, equation (1) below will need to be investigated.

$$I_3(t) = \text{Cos}\left(\frac{2 \cdot n_{eff}}{c} \cdot \Delta x \cdot (\alpha \cdot t + \omega_0)\right) \quad (1)$$

Parameters provides the starting wavelength, λ_{start} , the wavelength range, $\Delta\lambda$ and the scan rate $\frac{d\lambda}{dt}$. It is necessary to compute the angular frequency rate α which is defined as:

$$\alpha = \frac{d\omega}{dt} = \frac{\omega_{end} - \omega_{start}}{T} \quad (2)$$

Where T is the period. The angular frequency is defined as:

$$\omega = \frac{2 \cdot \pi \cdot c}{\lambda} \quad (3)$$

Based on the angular frequency definition, the start and end angular terms in eqn. (2) can be shown to be:

$$\omega_{start} = \frac{2 \cdot \pi \cdot c}{\lambda_{start}} \quad (4)$$

$$\omega_{end} = \frac{2 \cdot \pi \cdot c}{\lambda_{end}} \quad (5)$$

Expanding equation (2) components results in:

$$\omega_{end} - \omega_{start} = \frac{2 \cdot \pi \cdot c}{\lambda_{end}} - \frac{2 \cdot \pi \cdot c}{\lambda_{start}} \quad (6)$$

$$2 \cdot \pi \cdot c \cdot \left(\frac{1}{\lambda_{end}} - \frac{1}{\lambda_{start}} \right) \quad (7)$$

In order to get the period T , the wavelength range is divided by the scan rate such that:

$$T = \frac{\Delta\lambda}{\frac{d\lambda}{dt}} \quad (8)$$

Using eqns. (4), (5), (7) and (8), the angular frequency rate can then be computed to be:

$$\alpha = (\omega_{end} - \omega_{start}) \cdot \frac{1}{T} \quad (9)$$

$$2 \cdot \pi \cdot c \cdot \left(\frac{1}{\lambda_{end}} - \frac{1}{\lambda_{start}} \right) \cdot \frac{d\lambda/dt}{\Delta\lambda} \quad (10)$$

$$2 \cdot \pi \cdot c \cdot \left(\frac{\overbrace{\lambda_{start} - \lambda_{end}}^{-\Delta\lambda}}{\lambda_{end} \cdot \lambda_{start}} \right) \cdot \frac{d\lambda/dt}{\Delta\lambda} \quad (11)$$

$$2 \cdot \pi \cdot c \cdot \left(\frac{-\Delta\lambda}{\lambda_{end} \cdot \lambda_{start}} \right) \cdot \frac{d\lambda/dt}{\Delta\lambda} \quad (12)$$

$$-2 \cdot \pi \cdot c \cdot \frac{d\lambda/dt}{\lambda_{end} \cdot \lambda_{start}} \quad (13)$$

Re-writing it in terms of available components results in:

$$\alpha = -\frac{2 \cdot \pi \cdot c}{\lambda_{start}} \cdot \frac{d\lambda/dt}{(\lambda_{start} + \Delta\lambda)} \quad (14)$$

Now, using equations (4) and (14) into equation (1), results in:

$$I_3(t) = \text{Cos} \left(\frac{2 \cdot n_{eff}}{c} \cdot \Delta x \cdot \left(-\frac{2 \cdot \pi \cdot c}{\lambda_{start}} \cdot \frac{d\lambda/dt}{(\lambda_{start} + \Delta\lambda)} \cdot t + \frac{2 \cdot \pi \cdot c}{\lambda_{start}} \right) \right) \quad (15)$$

$$\text{Cos} \left(\frac{2 \cdot n_{eff}}{\epsilon} \cdot \Delta x \cdot \left(\frac{2 \cdot \pi \cdot \epsilon}{\lambda_{start}} \cdot \left[1 - \frac{d\lambda/dt}{(\lambda_{start} + \Delta\lambda)} \cdot t \right] \right) \right) \quad (16)$$

$$\text{Cos} \left(\frac{4 \cdot \pi \cdot n_{eff} \cdot \Delta x}{\lambda_{start}} \cdot \left[1 - \frac{d\lambda/dt}{(\lambda_{start} + \Delta\lambda)} \cdot t \right] \right) \quad (17)$$

The starting wavelength, range, location and scan speed can be used to model the intensity signal as seen by the detector in the Michelson interferometer. To determine the frequency of a reference length Δx , one references the definition with respect to the cosine as demonstrated below.

$$\text{Cos}(\omega_0 \cdot t) = \text{Cos}(2 \cdot \pi \cdot f \cdot t) \quad (18)$$

Regrouping terms in equation (17) on can show that:

$$2 \cdot \pi \cdot f = \frac{4 \cdot \pi \cdot n_{eff} \cdot \Delta x}{\lambda_{start}} \cdot \frac{d\lambda/dt}{(\lambda_{start} + \Delta\lambda)} \quad (19)$$

$$2 \cdot \pi \cdot f = \frac{4 \cdot \pi \cdot n_{eff} \cdot \Delta x \cdot d\lambda/dt}{\lambda_{start} \cdot (\lambda_{start} + \Delta\lambda)} \quad (20)$$

$$f = \frac{2 \cdot n_{eff} \cdot \Delta x \cdot d\lambda/dt}{\lambda_{start} \cdot (\lambda_{start} + \Delta\lambda)} \quad (21)$$

11 Appendix C: Supporting Works by the Author

Millimeter resolution distributed dynamic strain measurements using optical frequency domain reflectometry

A. K. Sang, M. E. Froggatt, S. T. Kreger, D. K. Gifford
Luna Technologies Inc., 3157 State Street, Blacksburg, Virginia 24060

ABSTRACT

We describe the use of swept wavelength interferometry for millimeter resolution dynamic fiber optic strain measurements on a cyclically loaded aluminum coupon using single mode fiber. The interrogation method is based on measuring the phase along the optical fiber and correlating the change in the phase derivative to strain via calibration. This technique enabled data acquisition at 150 Hz at a 1mm spatial resolution. A maximum spatial and strain range of 8 ms and $\pm 7,500 \mu\epsilon$, respectively, can be obtained. Measurements of the strain profile near a notch on the coupon demonstrate the utility of the high spatial resolution made possible with this technique.

Keywords: fiber optic sensing, distributed sensing, strain, structural health monitoring, dynamic strain

1. INTRODUCTION

Optical fiber, by nature of its physical characteristics, is an ideal distributed sensing medium. The light weight and small size enable easy integration into simple or complex multi-surface platforms with minimal impact to structural form or design. The dielectric nature of fiber further enables use in high electromagnetic interference (EMI) environments with no degradation to the measurand. Distributed strain measurements may be used for structural integrity in civil, automotive and aerospace structures. Such measurements may also be used as feed back for automation and control loops of various manufacturing processes and components such as automobiles, aircraft, robots etc.

There are several methods currently in use for distributed sensing using optical fiber. These include techniques based on inherent light scattering phenomena such as Raman¹, Brillouin², and Rayleigh³ as well as those involving multiplexed Fiber Bragg Gratings (FBGs)⁴. Techniques based on Raman and Brillouin scatter measurements typically employ optical time domain reflectometry (OTDR) and thus are not well suited for applications that require high spatial resolution. Rayleigh based systems presented thus far provide high spatial resolution but have been limited to pseudo-static measurements due to slower acquisition rates. Methods that employ FBGs can use either wavelength division multiplexing⁵ (WDM) or optical frequency domain reflectometry⁶ (OFDR) for signal demodulation. These methods achieve higher resolution than Raman or Brillouin scatter measurements but are often limited by the number of gratings that can be multiplexed in a single fiber.

We present a technique for measuring distributed strain or temperature with millimeter spatial resolution at acquisition rates of up to 500 Hz. The technique discussed herein uses OFDR to measure the reflected amplitude and phase of the fiber under test as a function of length with high spatial resolution. Variations to the spatial derivative of the optical phase are directly proportional to the shift in the reflected wavelength and can be related to changes in temperature or strain. Recent OFDR-based measurements have depended on monitoring the spectral shift of the optical spectrum over small segments of the fiber and correlating the change to the applied stimuli leading to sub-centimeter spatial resolution at a sub-Hertz update rate^{7,8}. The technique discussed herein has resulted in at least an order of magnitude improvement in resolution and greater than a 100-fold increase in the acquisition rate due to the development of fast yet highly linear drive circuitry of the tunable laser source, and rapid phase derivative and spatial filtering calculations performed on an embedded processor. A frequency mixing technique was used in the digital signal processor (DSP) to electronically tune the sampling region over broader range of fiber length.

In this work, we demonstrate the instrument capabilities in making high density, dynamic strain measurements using fiber containing semi-continuous FBGs bonded on a notched aluminum coupon also instrumented with a foil strain gauge and an extensometer. We demonstrate measurements at 150 Hz which compare well with the reference transducers.

Figure 4 shows the strain as a function of location at various times during specimen cyclic loading. Figure 4a shows the strain profile in the test specimen edge *with* the notch whereas Figure 4b shows the edge *without* the notch (refer to Figure 2 for path location references). As the strain loading increases, we see a modulation in the strain profile in the vicinity of the notch (~63 cm) with a peak strain of $\sim \pm 1000\mu\epsilon$ over a 1 cm region. The notch-free edge of the test coupon (Figure 4b) shows minimal spatial strain variation with peak temporal levels of $\sim \pm 550\mu\epsilon$. The resulting strain mapping along the aluminum test specimen shows, for the first time, a spatial strain variation at sub-centimeter resolution during dynamic loading.

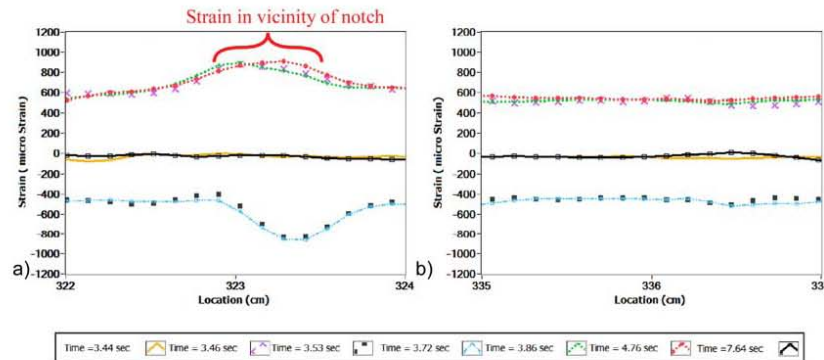


Figure 4. Strain profile as a function of position at both edges of the dog-bone test region

3. CONCLUSION

Luna Technologies has successfully demonstrated the unique ability of making millimeter resolution strain measurements at a 150 Hz acquisition rate over a 75 cm region and a 27 second duration on a notched aluminum test specimen by measuring the phase derivative of grating on an optical fiber. The measurement region could be shifted anywhere within a 8 m range from the instrument zero reference. The measurements were benchmarked against a standard foil strain gauge and an extensometer resulting in a favorable comparison. This method represents a practical, economical approach for high density, distributed strain measurements without compromising measurement accuracy.

REFERENCES

- [1] Dakin, J.P., Pratt, D.J., Bibby, G.W. and Ross, J.N., "Distributed Optical Fibre Raman temperature sensor using a semiconductor light source and detector", *Electron. Lett.*, 21, 1985, pp.569-570.
- [2] D.Culverhouse, F.Ferahi, C.N.Pannell, D.A.Jackson, "Exploitation of stimulated Brillouin scattering as a sensing mechanism for distributed temperature sensors and as a mean of realizing a tunable microwave generator", *Optical Fibre Sensors conference OFS'89, Springer Proceedings in Physics 44*, p.552, Springer-Verlag, Berlin, 1989.
- [3] M. Froggatt, B. Soller, D. Gifford, and M. Wolfe, "Correlation and keying of Rayleigh scatter for loss and temperature sensing in parallel optical networks," *OFC Technical Digest*, Los Angeles, March, 2004, paper PDP 17
- [4] Froggatt M., "Distributed measurement of the complex modulation of a photoinduced Bragg grating in an optical fiber", *Appl. Opt.* Vol35, p 5162, 1996
- [5] Araujo, F. M., Ferreira L. A., Santos, J. L. and Farahi F., "Demodulation scheme for fiber Bragg grating sensors based on active control of the spectral response of a wavelength division multiplexer", *Applied Optics*, Vol. 37, Issue 34, pp. 7940-7946, 1998
- [6] U. Glombitza and E. Brinkmeyer, "Coherent Frequency-Domain Reflectometry for Characterization of Single-Mode Integrated Optical waveguides", *J. Lightwave Technol.*, vol. 11, no. 8, pp. 1377 - 1384, 1993
- [7] S. Kreger, A. Sang, D. Gifford, M. Froggatt, "Distributed Strain and Temperature Sensing in Plastic Optical Fiber Using Rayleigh Scatter", *Proceedings SPIE Symposium on Defense, Security and Sensing*, April 2009
- [8] D. Gifford, S. Kreger, A. Sang, M. Froggatt, R. Duncan, M. Wolfe, B. Soller, "Swept-wavelength interferometric interrogation of fiber Rayleigh scatter for distributed sensing applications," *Proc. SPIE 6770*, (2007).

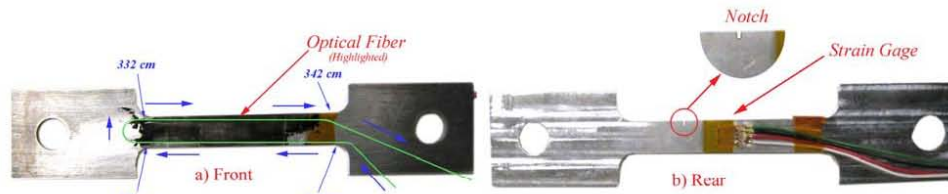


Figure 2. Mounted strain gauge and the optical fiber (a). Installation path Test specimen showing the notch (b)

An externally generated 20 Hz signal was used to control the load frame displacement profile over a 4 second period during which an external data acquisition system was used to record the extensometer and strain gauge data. The High Speed Distributed Sensing System (HSDSS) was configured to acquire data at 150 Hz, requiring the laser to sweep a 9 nm wavelength range at ~4,000 nm/sec. These settings result in HSDSS acquisition for a 27 second period over a 0.75 m window at a 1.4 mm spatial resolution with a $\pm 3,250 \mu\epsilon$ dynamic range. The 0.75 m window could be shifted to interrogate strain over a 8 m region.

Figure 3 shows the strain profile of the control signal (green), foil strain gauge (red), optical fiber (blue) and the extensometer (black) as a function of time. The spatial location on the optical fiber used for comparison was 3.23 m from the zero reference, which corresponds to instrument front panel. As a guide to the reader, the milled notch was located 3.24 m from zero. Examining Figure 3, we note the high correlation between the fiber optic, extensometer and foil strain gauge signals, with all oscillating at the 20 Hz input frequency. A peak-to-peak strain value of $520 \mu\epsilon$ was measured by all three transducers.

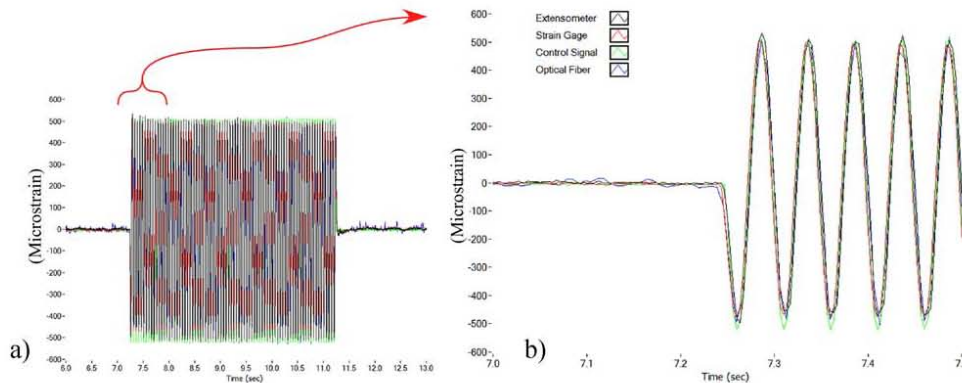


Figure 3. Strains as a function of time for the strain gauge, extensometer and optical fiber. a) Plot over time. b) Subset of test

To determine strain noise levels a three second data record prior to specimen dynamic loading shown in Figure 3 above (~4.25-7.25 sec) was analyzed. The key statistics are shown in Table 1 below. We note single digit standard deviation values for the foil strain gauge, extensometer and optical fiber. We remind the reader that the acquired optical measurements were at a 1.4 mm spatial resolution and 150 Hz sampling rate; a capability that, to this author's knowledge, has never been previously achieved.

Table 1 Statistics of Transducer data between 2.5 and 3.5 seconds

Transducer	Mean ($\mu\epsilon$)	1- σ Standard Deviation ($\mu\epsilon$)	Number of Points
Extensometer	1.58	3.38	921
Strain gauge	3.29	2.66	921
Control Signal	-4.59	2.28	921
Optical Fiber	-1.64	8.60	459

Figure 4 shows the strain as a function of location at various times during specimen cyclic loading. Figure 4a shows the strain profile in the test specimen edge *with* the notch whereas Figure 4b shows the edge *without* the notch (refer to Figure 2 for path location references). As the strain loading increases, we see a modulation in the strain profile in the vicinity of the notch (~63 cm) with a peak strain of $\sim \pm 1000\mu\epsilon$ over a 1 cm region. The notch-free edge of the test coupon (Figure 4b) shows minimal spatial strain variation with peak temporal levels of $\sim \pm 550\mu\epsilon$. The resulting strain mapping along the aluminum test specimen shows, for the first time, a spatial strain variation at sub-centimeter resolution during dynamic loading.

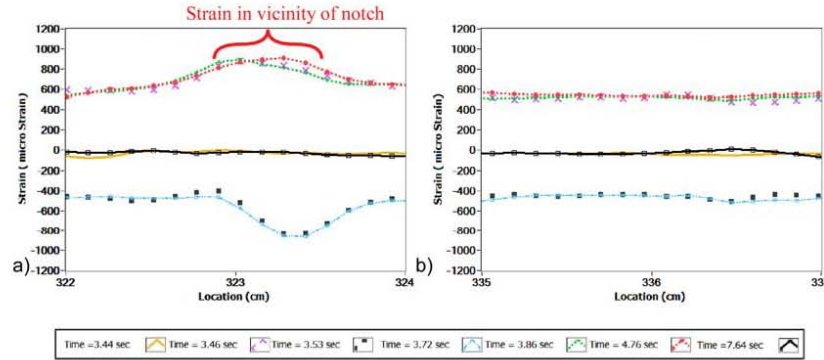


Figure 4. Strain profile as a function of position at both edges of the dog-bone test region

3. CONCLUSION

Luna Technologies has successfully demonstrated the unique ability of making millimeter resolution strain measurements at a 150 Hz acquisition rate over a 75 cm region and a 27 second duration on a notched aluminum test specimen by measuring the phase derivative of grating on an optical fiber. The measurement region could be shifted anywhere within a 8 m range from the instrument zero reference. The measurements were benchmarked against a standard foil strain gauge and an extensometer resulting in a favorable comparison. This method represents a practical, economical approach for high density, distributed strain measurements without compromising measurement accuracy.

REFERENCES

- [1] Dakin, J.P., Pratt, D.J., Bibby, G.W. and Ross, J.N., "Distributed Optical Fibre Raman temperature sensor using a semiconductor light source and detector", *Electron. Lett.*, 21, 1985, pp.569-570.
- [2] D.Culverhouse, F.Ferahi, C.N.Pannell, D.A.Jackson, "Exploitation of stimulated Brillouin scattering as a sensing mechanism for distributed temperature sensors and as a mean of realizing a tunable microwave generator", *Optical Fibre Sensors conference OFS'89, Springer Proceedings in Physics 44*, p.552, Springer-Verlag, Berlin, 1989.
- [3] M. Froggatt, B. Soller, D. Gifford, and M. Wolfe, "Correlation and keying of Rayleigh scatter for loss and temperature sensing in parallel optical networks," *OFC Technical Digest*, Los Angeles, March, 2004, paper PDP 17
- [4] Froggatt M., "Distributed measurement of the complex modulation of a photoinduced Bragg grating in an optical fiber", *Appl. Opt.* Vol35, p 5162, 1996
- [5] Araujo, F. M., Ferreira L. A., Santos, J. L. and Farahi F., "Demodulation scheme for fiber Bragg grating sensors based on active control of the spectral response of a wavelength division multiplexer", *Applied Optics*, Vol. 37, Issue 34, pp. 7940-7946, 1998
- [6] U. Glombitza and E. Brinkmeyer, "Coherent Frequency-Domain Reflectometry for Characterization of Single-Mode Integrated Optical waveguides", *J. Lightwave Technol.*, vol. 11, no. 8, pp. 1377 - 1384, 1993
- [7] S. Kreger A. Sang, D. Gifford, M. Froggatt, "Distributed Strain and Temperature Sensing in Plastic Optical Fiber Using Rayleigh Scatter", *Proceedings SPIE Symposium on Defense, Security and Sensing*, April 2009
- [8] D. Gifford, S. Kreger, A. Sang, M. Froggatt, R. Duncan, M. Wolfe, B. Soller, "Swept-wavelength interferometric interrogation of fiber Rayleigh scatter for distributed sensing applications," *Proc. SPIE 6770*, (2007).

One Centimeter Spatial Resolution Temperature Measurements from 25 to 850 °C Using Rayleigh Scatter in Gold Coated Fiber

A. K. Sang, M. E. Froggatt, D. K. Gifford and B. D. Dickerson

Luna Technologies Inc, 3157 State St, Blacksburg, VA 24060

sanga@lumatechnologies.com

Abstract: We present the use of swept wavelength interferometry for distributed fiber-optic, temperature measurements of up to 850 °C over a 1m fiber segment in commercially available, single mode, gold coated fiber. The interrogation technique is based on measuring the spectral shift of the intrinsic Rayleigh backscatter signal along the optical fiber and converting the spectral shift to temperature.

©2007 Optical Society of America

OCIS codes: 120.6780, 060.2370

1. Introduction

Optical fiber, by nature of its material properties, is an ideal distributed temperature sensor. There are several methods available for extracting distributed temperature information from optical fiber. These include techniques based on Raman, Brillouin, and Rayleigh scattering as well as those involving multiplexed fiber Bragg gratings (FBGs) [1-3]. Techniques based on Raman and Brillouin scatter measurement typically employ optical time domain reflectometry (OTDR), thus are not well suited for applications that require high spatial resolution. However, Raman thermometry has been demonstrated in various environments to temperatures of up to 550 °C [4, 5]. Methods that employ FBGs can use either wavelength division multiplexing (WDM) or optical frequency domain reflectometry (OFDR) for signal demodulation and achieve higher resolution than Raman or Brillouin scatter measurements but are often limited by the number of gratings that can be multiplexed in a single fiber. FBGs have been used for thermal monitoring to temperatures as high as 1150°C using bare fiber within stainless steel capillaries [6]. The lack of a protective buffer makes the sensing platform impractical for commercial use due to the fragility of bare fiber.

In this paper, we present measurements of high temperature changes on a centimeter scale in a 1 meter fiber segment exposed to temperatures of up to 850 °C. We use coherent reflectometry, or swept wavelength interferometry (SWI), to measure the Rayleigh backscatter as a function of length along the fiber with high spatial resolution [7]. A sensor is formed by measuring the temperature-induced shift in the reflected spectrum of the Rayleigh backscatter in the location of the heating [8]. This technique can provide temperature measurements as precise as 0.6% full scale over spatial regions as small as 1 cm up to 850 °C.

2. Experiment

In this work, commercially available communications grade, gold-coated single mode fiber was used in thermal testing between 25 - 850°C. The maximum temperature was a limitation of the fiber coating. Higher temperatures may be achievable with metallic coatings such as tungsten. Fig 1a shows the basic layout used during testing. The optical fiber was passed through a 17" Mellen box furnace capable of continuous operation at 1200°C. The optical fiber within the furnace was sheathed in a Ø0.080" thin-walled stainless steel capillary tube, which was then inserted into Ø0.25" x 24" medium pressure stainless steel tube for structural support. The outer tube minimized thermal fluctuations in the heated zone. The optical fiber was then connected to a Luna Technologies' Optical Backscatter Reflectometer (OBR) which was controlled by a standard desktop PC. The fiber temperature was also monitored using a type K thermocouple inserted within the outer tube, adjacent to the stainless steel capillary at the furnace center.

In this work, polarization-diverse SWI was used to measure both the amplitude and phase of the Rayleigh backscatter signal. The Rayleigh scatter as a function of length was then obtained via the Fourier transform (see reference 7 for details). Figure 1b shows an example of the backscatter amplitude as a function of position of the fiber under test (FUT). The fiber segment within the heated zone was characterized by a reduction in the optical

backscatter due to an in-house annealing procedure performed on the fiber prior to testing. The scatter profile was measured over a 7 meter length with a $\sim 20 \mu\text{m}$ resolution. However, the OBR is capable of performing such measurements to 30 meters.

In this test, temperature is calculated by first measuring and storing the complex Rayleigh scatter signature of the FUT at a baseline state. The scatter profile is then measured in a perturbed state. The scatter profiles from the two data sets are then compared along the entire fiber length in increments of Δx ; each segment represents a discrete sensing element. A spatial resolution (Δx) of approximately 1 cm was utilized in the data presented in this paper. Fig. 2 shows the spectral shift distribution of the fiber at various furnace temperatures. Peak spectral change is noticed between 1.6 m and 1.9 m, consistent with the known effective heated zone of the box furnace.

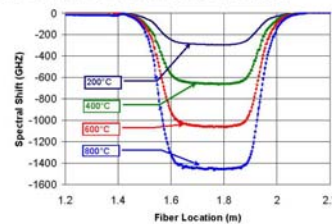
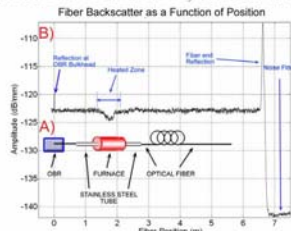


Fig. 1. a) Test layout schematic b) Backscatter as a function of position Fig. 2. Spectral shift as a function of position at various temperatures

Figure 3 shows the temperature and the spectral shift of a fixed location (1.65 m) during the test. Temperature targets were approached non-linearly to investigate transducer repeatability. Figure 4 shows temperature as a function of spectral shift. A correlation coefficient of 0.996 was calculated indicating a high level of agreement between the spectral shift and thermocouple data. A minimal level of hysteresis was noticed.

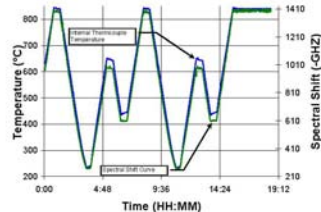


Fig 3. Temperature and Spectral shift as a function of time

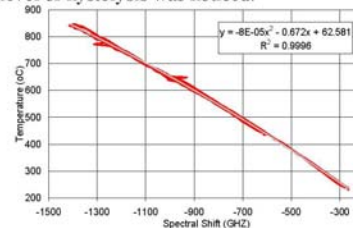


Fig 4. Thermocouple temperature vs spectral shift

3. Conclusions

Luna Technologies has successfully demonstrated the unique ability of making one centimeter resolution temperature measurements from 25 – 850 °C using Rayleigh scatter in commercially available single mode, gold coated fiber. This technique enables robust temperature measurements with high spatial resolution and good temperature accuracy. Temperature measurements can be performed on any telecommunications grade single mode fiber over a span of up to 30 m. with the primary thermal limitation being a function of the fiber coating. This method is a practical, economical approach for high temperature measurements.

References

- [1] J. P. Dakin, D. J. Pratt, G. W. Bibby, and J. N. Ross, *Electron. Lett.* **21**, 569 (1985).
- [2] D. Culverhouse, F. Farahi, C. N. Pannel, and D. A. Jackson, *Electron. Lett.* **25**, 913 (1989).
- [3] S.E. Kanellopoulos, V.A. Handerek and A.J. Rogers, *Opt.Lett.*, **20**, 333-335 (1995).
- [4] F. Jensen, E. Takada, and M. Nakazawa, *Proc. SPIE*, **2895**, 132-143 (1996)
- [5] R. Fececi, M. Farhadiroushan, V. A. Handerek, and A. J. Rogers *Rev. sci. instrum.* **68**, 3772-3776 (1997)
- [6] K. Stinson-Bagby and R. S. Fielder, *ICAPP Conference proceedings*, Pittsburg, Pa, June 2004 paper4299
- [7] B. J. Soller, D. K. Gifford M. S. Wolfe, and M. E. Froggatt, *OFC/NFOEC Technical Digest*, Los Angeles, March, 2005, paper NWD 3.
- [8] D. K. Gifford, B. J. Soller, M. S. Wolfe, and M. E. Froggatt, *ECOC Technical Digest*, Glasgow, Scotland, 2005, paper We4.P.5

One Centimeter Spatial Resolution Temperature Measurements in a Nuclear Reactor using Rayleigh Scatter in Optical Fiber

A. K. Sang, M.E. Froggatt, D. K. Gifford, S. T. Kreger, B. D. Dickerson

Luna Technologies, A Division of Luna Innovations Incorporated, 3157 State St., Blacksburg, VA 24060.

ABSTRACT

We present the use of swept wavelength interferometry for distributed fiber-optic temperature measurements in a Nuclear Reactor. The sensors consisted of 2 m segments of commercially available, single mode optical fibers. The interrogation technique is based on measuring the spectral shift of the intrinsic Rayleigh backscatter signal along the optical fiber and converting the spectral shift to temperature.

Keywords: optical fiber, OFDR, Rayleigh Scatter, temperature, distributed sensing, Radiation, Nuclear Reactor, Nuclear

1. INTRODUCTION

The nuclear industry has shown an emergent awareness of the possibilities offered by fiber optic technology for both data transfer and sensing applications to improve system cost and safety, while addressing the increasing technological obsolescence of instrumentation and control systems in current generation nuclear power plants [1, 2, 3]. Distributed strain measurements may be used for structural integrity monitoring of the reactor containment buildings or nuclear waste repository. With strategic location, strain measurements may provide feedback for automated optimization and control of reactor operation or indication of an impending failure before it becomes catastrophic [4, 5]. Distributed temperature measurements may be used around the outside of the pressure vessel for water cooled reactors for structural fatigue monitoring. The capability to make distributed temperature measurements of various components is also desirable in order to assure safe site operation [6]. In-core temperature measurements of gas cooled reactors are particularly challenging due to the combination of high temperatures and high neutron fluxes.

The presence of ionizing radiation fields in nuclear facilities is a major challenge in the application of both electronic and photonic equipment and sensors. In optical fiber sensors, ionizing radiation produces wavelength-dependent, radiation-induced attenuation which is exacerbated in measurement techniques whose working principle is based on intensity-related measurements [7, 8]. Even in the face of these challenges, however, the Nuclear Regulatory Commission (NRC) concluded in a study conducted in 1998 that fiber optic sensors have unique advantages in nuclear power plant instrumentation and control, making this technology worthy of further examination. The advantages cited include immunity to electromagnetic interference, the potential for higher sensitivity and accuracy, smaller size and reduced weight, higher bandwidth and multiplexing capabilities [9]. The same group later examined the survivability of fiber optic temperature sensors in a nuclear power plant environment [10].

There are several methods available for extracting distributed temperature information from optical fiber. These include techniques based on Raman, Brillouin, and Rayleigh scattering as well as those involving multiplexed fiber Bragg gratings (FBGs). Techniques based on Raman and Brillouin scatter measurement typically employ optical time domain reflectometry (OTDR), thus are not well suited for applications that require high spatial resolution. Methods that employ FBGs can use either wavelength division multiplexing (WDM) or optical frequency domain reflectometry (OFDR) for signal demodulation. These methods achieve higher resolution than Raman or Brillouin scatter measurements but are often limited by the number of gratings that can be multiplexed in a single fiber. Using OFDR to record the coherent Rayleigh scatter pattern results in spatial resolution as good as or better than FBGs, but like Raman or Brillouin scatter techniques, also obtains truly distributed measurements without modification to standard telecom-grade fiber.

In this paper, we present an initial feasibility test in which distributed temperature measurements are taken inside a nuclear reactor using selected, commonly available optical fibers. These measurements were made with centimeter scale spatial resolution over 2 m fiber segments. We use a commercially available instrument that implements swept wavelength interferometry (SWI) to measure the Rayleigh backscatter as a function of length along the fiber with high spatial resolution [11, 12]. A sensor is formed by measuring the temperature-induced shift in the reflected spectrum of the Rayleigh backscatter in the location of the heating [13]. This technique can provide temperature measurements as precise as 0.6% full scale over spatial regions as small as 1 cm up to 850 °C. The data presented herein demonstrates successful distributed temperature measurements in an environment that is known to be challenging for optical and electrical sensors.

2. EXPERIMENT

2.1 Measurement technique

OFDR provides both the high spatial resolution and sensitivity necessary to obtain the coherent Rayleigh scatter profile. The measurement network in the commercially available instrument used to acquire the amplitude and phase of the Rayleigh backscatter signature as a function of fiber length is shown in Figure 1. Light from an external-cavity tunable laser source (TLS) is split between the reference and measurement arms of an interferometer. In the measurement path, a 50/50 coupler further splits the light to interrogate a length of fiber under test (FUT) and returns the reflected light. Another 50/50 coupler then recombines the measurement and reference fields. A polarization beam splitter (PBS) and a polarization controller (PC) are used to split the reference light evenly between two orthogonal polarization states. As the laser is linearly tuned in frequency the interference between the measurement field and the reference field is recorded at detectors labeled S and P. This polarization diversity technique is used in OFDR to mitigate signal fading due to polarization misalignment of the interfering measurement and local-oscillator fields. Not shown in the figure is an auxiliary interferometer used to trigger data acquisition in equal optical frequency increments. Also not shown is a portion of the network wherein a HCN gas-cell is used to monitor the absolute wavelength of the scanning laser.

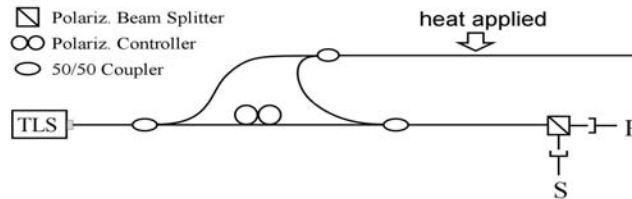


Figure 1. Optical network used for polarization-diverse measurement of Rayleigh backscatter.

Figure 2 is an example of Rayleigh scatter amplitude as a function of position in a 25 meter optical fiber spool. Notice the vector sum of the amplitudes of the S and P polarization states form the final polarization diverse measurement. The spatial resolution of the Rayleigh scatter measurement, Δz , is directly related to the resolution in the time domain and is determined by the spectral bandwidth of the scan range according to:

$$\Delta z = \frac{\lambda_s \lambda_f}{2n\Delta\lambda}, \quad (1)$$

where n is the group delay of material under test, λ_s and λ_f are the start and finish wavelengths, and $\Delta\lambda$ is the wavelength range of the measurement scan. In this instance, the laser was scanned from 1535 nm to 1575 nm, which corresponds to a bandwidth of 5 THz and a spatial resolution Δz , equal to 20 μm . This resolution can be corrupted by environmental noise, insufficiently linear laser tuning and excess of unbalanced dispersion in the measurement arm. Equation (1) is representative of the measured two-point resolution in our measurement system with no special steps taken for temperature or vibration isolation.

The maximum FUT length L_{max} is approximately determined by Nyquist sampling criteria by

$$L_{\text{max}} = \frac{cR_s}{4n\partial v/\partial t}, \quad (2)$$

where c is the speed of light, R_s is the average sample rate, n is the group index of the FUT, and $\partial v/\partial t$ is the laser spectral scan rate which is related to the wavelength scan rate by $\partial v/\partial t = -c/\lambda^2 \partial \lambda/\partial t$. The factor of four in the denominator is due to the Nyquist sampling limit and the double-pass nature of the measurement interferometer. Since the data acquisition is triggered by an internal interferometer the ratio of R_s to $\partial v/\partial t$ is constant (neglecting the effects of dispersion). Equation (2) is useful for indicating the trade offs between the scan range, the laser tuning rate, and the required sampling frequency. The constraint which links Equations 1 and 2 is the limit of the size of the data array which can be practically collected and processed, $N_{\text{max}} = R_s \Delta\lambda / (\partial \lambda/\partial t)$. The data in Figure 2 was taken with an average sample rate of 2 MS/s with a tuning rate of 20 nm/s, producing a maximum measurable FUT length of 40 m,

minus several meters of fiber interior to the instrument. This resulted in a sample size of 4 million points. The total measurement time including processing for this data set is approximately 3.5 seconds. No averaging was performed to achieve this data, however the data displayed in Figure 2 was spatially filtered with an effective bandwidth of approximately 10 mm. Further detail concerning the use of OFDR to measure the coherent Rayleigh scatter profile can be found in reference 14.

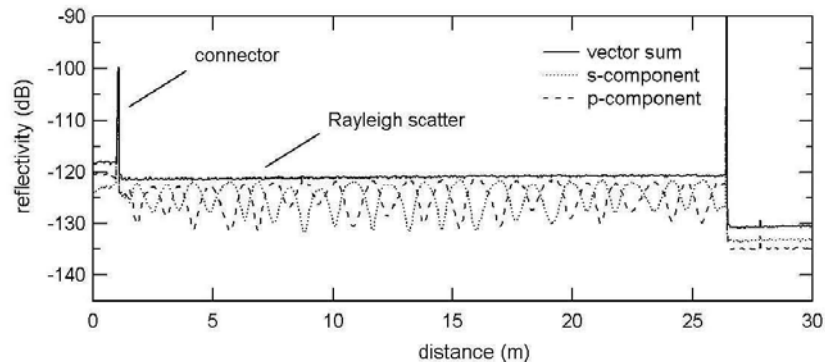


Figure 2 The reflectivity of a 25 meter spool (5 cm radius) of standard single-mode fiber. The top trace is the vector sum of the S and P components of the Fourier transform of the interference signals measured on the two detectors shown in Figure 1. The oscillations in the S and P curves are caused by birefringence (or PMD) induced in the fiber due to coiling.

Rayleigh backscatter in optical fiber is caused by random fluctuations in the index profile along the fiber length. For a given fiber, the scatter amplitude and phase pattern as a function of distance is a random but static property of that fiber and can be modelled as a long, weak FBG with a random period. Changes in the local period of the Rayleigh scatter caused by an external stimulus (like strain or temperature) in turn cause shifts in the locally reflected spectrum. These local spectral shifts can then be calibrated and assembled to form a distributed strain or temperature measurement.

A distributed sensor is formed by first measuring and storing the Rayleigh scatter signature of the FUT at an ambient temperature and null strain state. Then the scatter profile is measured at a later time with strain or a temperature perturbation applied to the fiber. The complex data sets from each detector, S and P, are broken into segment lengths Δs along the FUT and Fourier transformed into the optical frequency domain. A vector sum of the S and P spectra is then calculated to generate a polarization-independent spectrum associated with each interval. To determine the spectral shift between the reference and perturbed scans, a cross-correlation is performed for each FUT interval. Any change in strain or temperature manifests as a shift in the correlation peak. A distributed measurement is formed by compiling the spectral shifts for each interval along the FUT.

Figure 3a shows the fiber Rayleigh backscatter spectra along a 5mm segment for a reference scan at ambient temperature and scan of the same fiber interval after heating. Figure 3b then shows the cross-correlation with the reference spectrum for a measurement scan with and without temperature shift. The spectral difference between the shifted peak and the unshifted peak is directly proportional to the temperature shift in this fiber interval.

It is important to note that the segment length Δs affects the signal-to-noise ratio of the shift - a wider Δs incorporates more data points and gives better spectral resolution. However, if the local spectral shift varies significantly over Δs , the cross correlation peak may spread out and become difficult to detect, resulting in higher noise levels. Thus in fiber sections where there is a strong temperature or strain gradient reducing Δs often produces a more stable result.

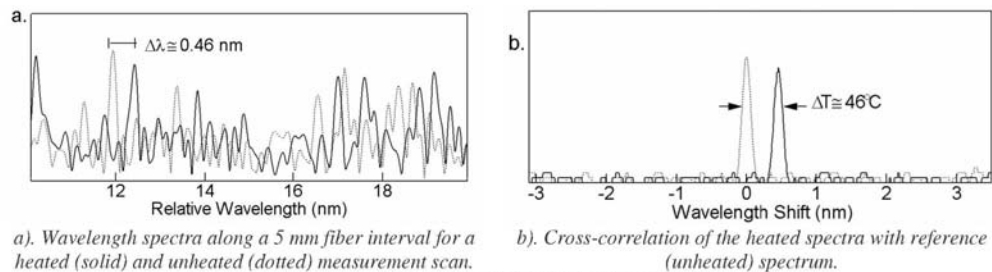


Figure 3. Demonstration of a Thermal shift of an optical fiber

2.2 Test Facility

The tests conducted herein were performed in the Ohio State University Research Reactor (OSURR). The facility is a pool-type reactor that can continuously vary the thermal power from 0.1 – 100 % of a maximum of 500 KW. At full power the neutron flux is 1.2×10^{13} n/cm²-s and gamma flux is 100×10^6 Rads / hour. The reactor has a 6.4 cm diameter tube that functions as a dry well which extends from the top of the reactor pool down into a position in the core grid along the south edge of the core [15].

2.3 Experimental setup

In this initial experiment, four commercially available optical fibers were prepared for nuclear radiation. These include 1) SMF28 – Polyamide coated, 2) 1550 nm Silica core – Acrylate coated, 3) 1550 nm 20 wt% GeO doped – Acrylate coated and 4) 1300 nm – Copper coated. The SMF-28 fiber and 1300nm copper coated fiber both have Germanium-doped cores, approximately 5 wt% GeO.

The fibers were bundled into a loose tube buffer which was then looped and bonded to a 1 meter aluminum “L” bracket to form a 2 meter measurement area. The “L” bracket was then inserted into a 5-Meter, 3.8 cm diameter tube to facilitate insertion into the existing drywell of the OSURR. Arrays of thermocouples were located at two vertical locations 0.4 m and 1.1 m from the reactor floor to enable both in-core and ex-core irradiation measurements as illustrated in Figure 4a. The commercially available instrument used to record the complex Rayleigh scatter is denoted in the figure by “OBR”, an acronym for Optical Backscatter Reflectometer. The test was conducted at 90% thermal power (450KW) for 13 effective full power hours as illustrated in Figure 4b.

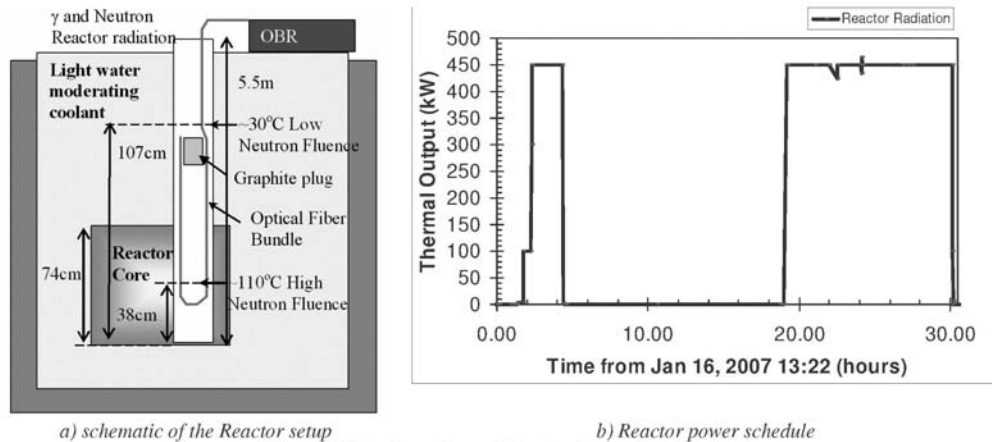


Figure 4. Reactor setup and thermal output during test.

3. DISCUSSION OF RESULTS

Figure 5 shows the typical spectral response profile as a function of position of the candidate fibers. The position datum selected was referenced to the low neutron fluence thermocouple location. As a reminder to the reader, the spectral response is a relative measurement from a reference baseline; hence, the initial value begins nominally at zero. As expected, a mirrored spectral response from the two attachment paths on the aluminum bracket is reflected in the data (see fiber path illustration in Figure 4a).

Figure 6 and Figure 7 show the spectral response of the various fiber types to the thermal environment induced by the irradiation over the test period in the high and low neutron fluence measurement areas. The spectral shift is negative with an increase in temperature, hence, for simplicity in comparison, we show the negative spectral response of the optical fibers (left 'y' axis in Gigahertz). As expected, in the region of high neutron fluence, we see an increased temperature as indicated by the co-located, shielded thermocouple. We note that all four fibers clearly track the measured temperature, capturing similar thermal fluctuations experienced during the test. The copper coated fiber experiences the largest spectral shift of the test candidates in both the low and high neutron fluence regions. This is theorized to be a result of the effects of the thermal expansion of the coating increasing the fiber elongation, thus causing a proportionately larger spectral shift.

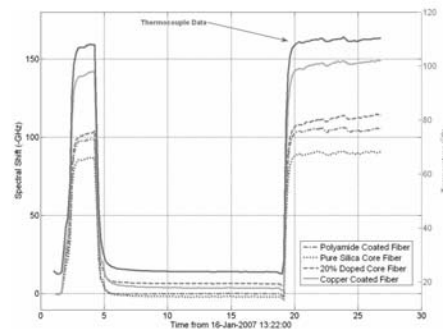
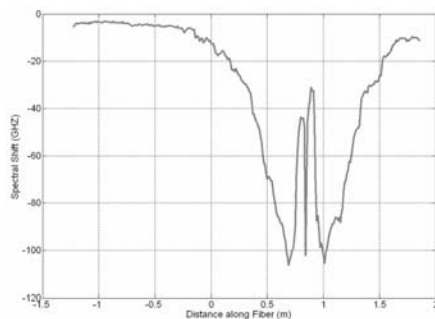


Figure 5 Spectral shift vs. position (SMF 28 Fiber 28 hrs)

Figure 6 Spectral shift at high neutron fluence area

The data further shows evidence of dopant influence on the fiber spectral response to the temperature changes. Neglecting the copper-coated fiber (due to coating influence), the 20 wt% GeO doped fiber shows the largest spectral shift followed by the polyamide coated (5 wt% GeO doped) then the pure silica core (un-doped) fiber; showing a correlation of dopant level to the spectral shift of the optical fiber. Figure 8 shows the spectral shift as a function of temperature for the various fiber types. In all four cases, we see evidence of a linear correlation to temperature. The nonlinearity noticed between 40-50°C is thought to be as a result of the rapid temperature increase during reactor startup, as evidenced by the increase in the periodicity of the graph markers for all four candidate fibers.

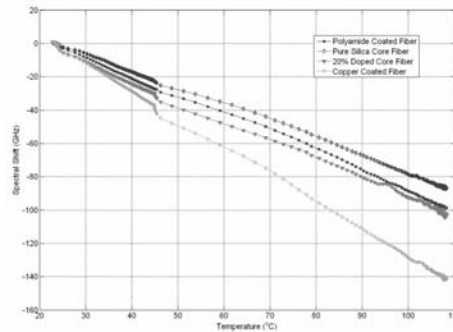
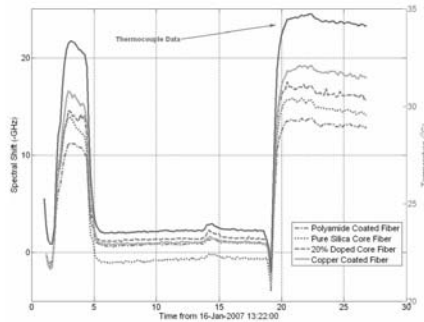


Figure 7 Spectral shift at low neutron fluence area

Figure 8 Spectral shift versus temperature

4. CONCLUSION

Luna Technologies has successfully demonstrated the unique ability of making one centimeter resolution temperature measurements in a radiation environment using Rayleigh scatter in commercially available single mode fibers over various coatings and dopant concentrations. This technique enables robust temperature measurements with high spatial resolution and good temperature accuracy. Temperature measurements can be performed on any telecommunications grade fiber over a span of 70 m or more with the primary thermal response being a function of the fiber coating and/or dopant level. This method represents a practical, economical approach for distributed thermal measurements in a radiation environment.

5. ACKNOWLEDGEMENTS

Joseph Talnagi coordinated radiation exposures of optical fiber in the Nuclear Reactor Laboratory at Ohio State University. This material is based upon work supported by the Department of Energy (National Nuclear Security Administration under Award Number DE-FG02-04ER83991).

Disclaimer. "This report was prepared as an account of work sponsored by an agency of the United States Government. Neither the United States Government nor any agency thereof, nor any of their employees, makes any warranty, express or implied, or assumes any legal liability or responsibility for the accuracy, completeness, or usefulness of any information, apparatus, product, or process disclosed, or represents that its use would not infringe privately owned rights. Reference herein to any specific commercial product, process, or service by trade name, trademark, manufacturer, or otherwise does not necessarily constitute or imply its endorsement, recommendation, or favoring by the United States Government or any agency thereof. The views and opinions of authors expressed herein do not necessarily state or reflect those of the United States Government or any agency thereof."

REFERENCES

1. E. Takada et. al., "New techniques to apply optical fiber images guides to harsh radiation environments in nuclear facilities," Proc. SPIE 3538, 40-47, 1998
2. Hangying Liu et. al., "Neutron radiation effects on Fabry-Perot fiber optic sensors" J. Nuc. Inst. & Meth in Phys. A 507 (2003) 691-702
3. J. W. Spencer et. al., "Fibre optic sensor system assessment in radiation environments", Proc. SPIE Vol. 2425, p. 96-104
4. P. Ferdinand et. al., "Optical fibre Bragg grating sensors for structure monitoring within the nuclear power plants," Proc. SPIE 2425, 11-20, 1994
5. A. Fernandez et. al., "Multi-component force sensors based on fibre Bragg grating strain sensors for highly radioactive environments," Proc. Phytotec '99 European Workshop, pp127-133 (1999)
6. F. Jensen, et. al., "Development of a distributed monitoring system for temperature and coolant leakage", Proc IAEA OECD/NEANSC Incore '96 Meeting, Mito, Japan (1996)
7. D. L. Griscom, "Gamma-ray induced optical attenuation in Ge-doped-silica optical-fiber waveguides," J. Appl. Phys. 78, 6696-6704 (1995)
8. F. Berghmans, et. al., "Radiation hardness of fiber-optic sensors for monitoring and remote handling applications in nuclear environments," Proc SPIE 3538, 28-39 (1998)
9. Liu, H. et. al., "Gamma Radiation Resistant Fabry-Perot Fiber Optic Sensors," *Rev. of Sci. Instrum.*, **73** (8), pp. 3112-3118 (2002)
10. Liu, H. et al., "Neutron Radiation Effects on Fabry-Perot Fiber Optic Sensors," *Nuclear Instrum. and Meth. in Phys. Res. A*, **507**, pp. 691-702 (2003)
11. M. Froggatt and J. Moore, "High resolution strain measurement in optical fiber with Rayleigh scatter," *Appl. Opt.*, **37**, 1735-1740 (1998).
12. B. J. Soller, D. K. Gifford, M. S. Wolfe, and M. E. Froggatt, *OFC/NFOEC Technical Digest*, Los Angeles, March, 2005, paper NWD 3.
13. D. K. Gifford, B. J. Soller, M. S. Wolfe, and M. E. Froggatt, *ECOC Technical Digest*, Glasgow, Scotland, 2005, paper We4.P.5
14. B. J. Soller, D. K. Gifford, M. S. Wolfe and M. E. Froggatt, "High resolution optical frequency domain reflectometry for characterization of components and Assemblies," 24 January 2005 / Vol. 13, No. 2 / OPTICS EXPRESS 674.
15. Ohio State University Nuclear Reactor Laboratory, <http://www-nrl.eng.ohio-state.edu/>

REFERENCES

- ¹<http://www.madehow.com/Volume-7/Scale.html>
- ²Sleeswyk, André Wegener Vitruvius' Odometer , Scientific American 245.4 (October, 1981), pp. 188-200
- ³Adam, Jean-Pierre, Roman Building: Materials and Techniques, (London: B.T. Batsford, 1994),
- ⁴http://transportationhistory.suite101.com/article.cfm/roman_roads
- ⁵Russell Brown, Lester. Eco-Economy, James & James / Earthscan. ISBN 1-85383-904-3
- ⁶Die galvanische Kette : mathematisch bearbeitet (The Galvanic Circuit Investigated Mathematically), Berlin : Riemann, 1827. - 245 S. : graph. Darst
- ⁷Duffin, W.J. (1980), Electricity and Magnetism, 3rd edition, McGraw-Hill, p. 179, ISBN 007084111X
- ⁸S. Hunter Christie, The Bakerian Lecture: Experimental Determination of the Laws of Magneto-electric Induction in different masses of the same metal, and its intensity in different metals. , Philosophical Transactions of the Royal Society of London, vol. 123, 1833, pp. 95-142
- ⁹Lynch J., Patridge A., et. al Design of Piezoresistive MEMS-Based Accelerometer for Integration with Wireless Sensing Unit for Structural Monitoring , J. Aerospace Engineering, Vol. 16 No. 3 pp. 108, 2003
- ¹⁰Farrar, C.R. Historical overview of structural health monitoring *lecture notes on structural health monitoring using statistical pattern recognition*, Los Alamos, N.M., 2001
- ¹¹Lynch, J. P. Decentralization of wireless monitoring and control technologies for smart civil structures. PhD thesis, Dept of Civil and Environmental Engineering, Stanford Univ., Stanford Ca. 2002
- ¹²Maiman T H 1960 Stimulated optical radiation in ruby masers Nature 187 493
- ¹³McIntyre, R. J, Theory of Microplasma Instability in Silicon , J. Appl. Phys. Vol 32, No 6, 983-995,1960
- ¹⁴Kao K C and Hockham G A, Dielectric fibre surface waveguides for optical frequencies , Proc. IEE 133 1151–1158,1966
- ¹⁵Jerzy Kalenik, Ryszard Pająk, A cantilever optical-fiber accelerometer, Sensors and Actuators , J. Sensors & Actuators, Volume 68, Issues 1-3, 15 June 1998, Pages 350-355
- ¹⁶C. Doyle, G. Fernando, An intensity-based fiber-optic vibration sensor , Proc. SPIE 2718 (1996) 94-101
- ¹⁷H.W. Fuller, Cantilevered-beam, fiber optic angular accelerometer , US Patent No. 4 419 895, 1983
- ¹⁸B.S. Chandrasekar, T.S. Radha, B.S. Ramprasad, A simple fiber optic vibration sensor , Pacific Northwest Fiber Optic Sensor Workshop, Troutdale, OR, USA, 1995, Proc. SPIE 2574 (199.5) 159-164.
- ¹⁹Rogers A J, Optical measurement of current and voltage on power systems , IEEE J. Electr. Power App. 2 120–124, 1979
- ²⁰Ulrich, R. Fiber-Optic Rotation Sensing with Low Drift , Optics Letters 2E, vol 5, pp. 173-175, 1980.
- ²¹Lieberman R A, Blyler L L and Cohen L G, A distributed fibre-optic sensor based on cladding fluorescence , IEEE J. Lightwave Technol. 7 741–746, 1989
- ²²Personick S D, Photon probe—an optical time-domain reflectometer , Bell System Technical Journal 56 355–366, 1977
- ²³Tongue, Benson, *Principles of Vibration*, Oxford University Press, 2001
- ²⁴<http://www.army-technology.com/contractors/noise/bruelkjaer2/bruelkjaer24.html>
- ²⁵K. Thyagarajan, Ajoy K. Ghatak, Fiber Optic Essentials, John Wiley & Sons, pp34, 2007
- ²⁷K. Thyagarajan, Ajoy K. Ghatak, Introduction to Fiber Optics, Cambridge Uni. Press, pp 18, 1998
- ²⁹Force, Inc. (2005-04-14). Types of Optical Fiber
- ³⁰<http://www.fiberoptics4sale.com/Merchant2/multimode-fiber.php>
- ³¹Personick S D, Photon probe—an optical time-domain reflectometer , Bell System Technical Journal 56 355–366, 1977
- ³²M. K. Barnoski and S.M . Jensen, Fiber waveguides: A novel technique for investigating attenuation characteristics, *Appl. Opt.*, vol. 15, 2112 (1976).
- ³³J. P. Dakin, Distributed optical fiber sensors, in Distributed and Multiplexed Fiber Optic Sensors, II, p. 76, Proc. SPIE, vol. 1797, 1992.
- ³⁴Rogers A J Polarization-optical time domain reflectometry: a new technique for the measurement of field distributions , Appl. Opt. 20 1060–1074, 1981

- ³⁵Rogers A.J, Polarization-optical time-domain reflectometry , *Electron. Lett.* Vol 16, 489–490, 1980
- ³⁶Leblanc, Michel, Polarization-OTDR for measuring characteristics of optical fibers , US Patent 6,724,469, Apr 20 2004
- ³⁷<http://en.wikipedia.org/wiki/Polarization>
- ³⁸Dakin, J.P., Pratt, D.J., Bibby, G.W. and Ross, J.N., Distributed Optical Fibre Raman temperature sensor using a semiconductor light source and detector , *Electron. Lett.*, 21, 1985, pp.569-570.
- ³⁹Harris and Bertolucci, *Symmetry and Spectroscopy* , Dover Publications, 1989
- ⁴⁰Ferraro, J. & Nakamoto, K., *Introductory Raman Spectroscopy* , San Diego, Ca, Academic Press, 1994
- ⁴¹Thevenaz, L, *Review and Progress in Distributed Fiber Sensing* , OSA, 2006
- ⁴²Dakin J P, Pratt D J, Ross J N and Bibby G W, Distributed anti-Stokes Raman thermometry Proc. Conf.on Optical-Fibre Sensors 3 (San Diego) postdeadline paper,1985
- ⁴³D.Culverhouse, F.Ferahi, C.N.Pannell, D.A.Jackson, Exploitation of stimulated Brillouin scattering as a sensing mechanism for distributed temperature sensors and as a mean of realizing a tunable microwave generator , *Optical Fibre Sensors conference OFS'89*, Springer Proceedings in Physics 44, p.552, Springer-Verlag, Berlin, 1989.
- ⁴⁴Horiguchi T. & Tateda M., Optical- fiber-attenuation investigation using stimulated Brillouin scattering between a pulse and a continuous wave , *Optics Letters*, 14, p.408, 1989.
- ⁴⁵Rogers A J, *Essentials of Opto-electronics* , Chapman and Hall, London, Eng, pp 329–35, 1997
- ⁴⁶Kersey A D A Review of Recent Developments in Fiber Optic Sensor Technology , (Invited Paper) OFT, Vol 2, pp 291-317, Article No. 0036, 1996
- ⁴⁷Horiguchi T. et al., Measurement of temperature and strain distribution by Brillouin frequency shift in silica optical fibers, in *Distributed and Multiplexed Fiber Optic Sensors, II*, p. 2, Proc. SPIE, vol. 1797, 1992
- ⁴⁸Horiguchi T. et al., Development of a distributed sensing technique using Brillouin scattering, *IEEE J. Lightwave Technol.*, vol. 13, p.1296,1995
- ⁴⁹X. Bao et al., Combined distributed temperature and strain sensor based on Brillouin loss in an optical fiber, *Opt. Lett.*, vol. 19, p. 141, 1994
- ⁵⁰Youngquist R. C. , Carr S and Davies D. E. N. Optical coherence domain reflectometry: a new optical evaluation technique , *Opt. lett.* , vol 12 No. 3, pp158, 1987
- ⁵¹Wentworth, R. H. Theoretical noise performance of coherence-multiplexed interferometric sensors , *J of Lightwave Tech*, Vol 7 Is 6 pp 941-956, 1989
- ⁵²ANDO, High-Resolution Reflectometer AQ7410B , product manufactured by NTT Electronics Co and Ando Electric Co. using the technology of Nippon Telegraph and Telephone Corporation
- ⁵³Baney, D. M., Sorin, W. V., Extended-Range optical Low-Coherence Reflectometry Using a Recirculating Delay Technique , *Instruments and Photonics Laboratory*, HPL-93-33, 1993
- ⁵⁴U. Glombitza and E. Brinkmeyer, Coherent Frequency-Domain Reflectometry for Characterization of Single-Mode Integrated Optical waveguides , *J. Lightwave Technol.*, vol. 11, no. 8, pp. 1377 - 1384, 1993
- ⁵⁵Hill, K. O. and Meltz G., Fiber Bragg Grating Technology Fundamentals and Overview , *J of Lightwave Technol.* vol. 15, no. 8, 1997
- ⁵⁶K. O. Hill, Y. Fujii, D. C. Johnson, and B. S. Kawasaki, Photosensitivity in optical fiber waveguides: Application to reflection filter fabrication, *Appl. Phys. Lett.*, vol. 32, pp. 647–649, 1978.
- ⁵⁷B. S. Kawasaki, K. O. Hill, D. C. Johnson, and Y. Fujii, Narrow-band Bragg reflectors in optical fibers, *Opt. Lett.*, vol. 3, pp. 66–68, 1978.
- ⁵⁸Meltz G., et al., Formation of Bragg Gratings in Optical Fibers by a Transverse Holographic Method , *Optics Lett.*, 14, p. 823, 1989.
- ⁵⁹Hill K. O., et al, Bragg Gratings Fabricated in Monomode Photosensitive Optical Fiber by UV Exposure through a Phase Mask , *Appl. Phys. Lett.*, vol 62, p. 1035, 1993
- ⁶⁰Askins C. G. et al., Fiber Bragg grating reflectors prepared by a single excimer laser pulse, *Opt. Lett.*, p.833, 1992
- ⁶¹Askins C. G. et al., Considerations for producing single-pulse fiber Bragg gratings, in *Distributed and Multiplexed Fiber Optic Sensors, III*, p 12, Proc. SPIE, vol. 2071, 1993.
- ⁶²Askins C. G. et al., Stepped-wavelength optical fiber Bragg grating arrays fabricated in line on a draw tower, *Opt. Lett.*, vol. 19, p 147, 1994
- ⁶³Hill, O. K. and Meltz, G, Fiber Bragg Grating Technology Fundamentals and Overview , *Journal of lightwave Tech*, Vol 15 No 8, 1997
- ⁶⁴Morey W. W. *et al*, Recent Advances in Fiber Grating Sensors for Utility Industry Applications , *Proc. SPIE Vol 2594*, 1995

-
- ⁶⁵ Dankin J., Culshaw B., *Optical Fiber Sensors Volume Four: Applications, Analysis, and Future Trends*, Ed., Artech House, Boston, 1997
- ⁶⁶ Kersey A. D. *et. al*, *Fiber Grating Sensors*, *J. of Lightwave Tech.* vol. 15, p 8, 1997
- ⁶⁷ Araujo, F. M. Ferreira L. A., Santos, J. L. and Farahi F., *Demodulation scheme for fiber Bragg grating sensors based on active control of the spectral response of a wavelength division multiplexer*, *Applied Optics*, Vol. 37, Issue 34, pp. 7940-7946, 1998
- ⁶⁸W. Eickoff, R. Ulrich., *Optical frequency domain reflectometry in single-mode fiber*, *Appl. Phys. Lett.* 39, 693, 1981.
- ⁶⁹Froggatt M., *Distributed measurement of the complex modulation of a photoinduced Bragg grating in an optical fiber*, *Appl. Opt.* Vol35, p 5162, 1996
- ⁷⁰Froggatt M., Moore J., *Distributed Measurement of Static Strain in an Optical Fiber with Multiple Bragg Gratings at Nominally Equal Wavelengths*, *Appl. Opt.* 37, p 1741, 1998
- ⁷¹ L. Melvin *et. al.*, *Integrated Vehicle Health Monitoring (IVHM) for Aerospace Vehicles*, *Structural Health Monitoring: Current Status and Perspectives*, F. K. Change, Ed., p 705, 1997
- ⁷² Davis, M.A. Kersey, A.D. *Application of a fiber Fourier transform spectrometer to the detection of wavelength encoded signals from Bragg grating sensors*, *Journal of Lightwave Technology*, vol 13 Issue 7, p. 1289-1295, 1995.
- ⁷³ Kersey, A.D. *et al.* (1992), *High-Resolution Fibre-Grating Based Strain Sensor With Interferometric Wavelength-Shift Detection* *Electron. Lett.* 28(3) p. 236-238, 1992
- ⁷⁴ Marcuse D., *Coupled mode theory of round optical fibers*, *Bell Sys. Tech. J.* vol 52, p 817–842, 1973
- ⁷⁵ C. Askins *et. al.*, *Stepped-wavelength optical-fiber Bragg grating arrays fabricated in line on a draw tower*, *Opt. Lett.* Vol 19, Is 2, pp 147, 1994
- ⁷⁶A. K. Sang, M. E. Froggatt *et. al.*, *Millimeter resolution distributed dynamic strain measurements using optical frequency domain reflectometry*, OFS, Ontario, Canada, 2011
- ⁷⁷ H. A. Haus and W P. Huang, *Coupled-mode theory*, *Proceedings, IEEE* Vol 79, pp 1505-1518, 1991
- ⁷⁸ Huang, W. P, *Coupled-mode theory for optical waveguides: an overview* *Opt. Soc. Am.* Vol 11 No. 3 p 963, March 1994
- ⁸⁰ Sang A., Froggatt M., Gifford D., Dickerson B., *One Centimeter Spatial Resolution Temperature Measurements from 25 to 850°C Using Rayleigh Scatter in Gold Coated Fiber*, CLEO 2007